Combined Tangential-Normal Injection Into A Supersonic Flow

by

Peter Samuel King

Thesis submitted to the Faculty of the

Virginia Polytechnic Institute and State University

in partial fulfillment of the requirements for the degree of

Master of Science

in

Aerospace Engineering

APPROVED:

Dr. J. A. Schetz, Chairman

Dr. D. A. Walker

Dr. W. F. Ng

February, 1989

Blacksburg, Virginia

Combined Tangential-Normal Injection Into A Supersonic Flow

by

Peter Samuel King

Dr. J. A. Schetz, Chairman

Aerospace Engineering

(ABSTRACT)

A combination of tangential and normal air injection into a Mach 3 airflow was experimentally studied. A rearward facing slot producing tangential injection at a nominal Mach number 1.7 was operated at several different total pressures. An array of transverse tubes of height equal to the slot height and placed just downstream of the slot was operated at two dynamic pressure ratios as well as at Mach 1 and 2.2. Mean flow measurements of static and total pressures were taken up to 20 slot heights downstream from which Mach number, density, velocity and entrainment rates were calculated. Various dimensions and spreading angles of the mixing regions were measured directly from Nanoshadowgraphs and Schlieren photographs. Large eddy structures were produced in several cases, leading to increased entrainment of the free stream. For some cases, heated air was injected through the normal tubes, and the jet total temperature decay was measured downstream. It can be seen from the data as a whole that the mixing rate can be significantly increased by the combined tangential-normal injection design over tangential slot injection alone, with up to as much as 92% more entrained mass.

Acknowledgements

I would like to deeply thank for his guidance, advice, and friendship. His support was critical in my decision to start graduate studies.

Next I would like to thank , whose hours of work, advice, and motivation enabled this research to come to a successful completion.

and lent valuable experience and advice.

at APL also gave a lot of support and advice to this project.

Many of my fellow students also assisted me in this work. In particular, I would like to thank , ,

and for their help and support. , ,

and from the Aerospace Dept. shop helped make sure that everything fit together and worked.

Finally, I would like to my parents, And for their love and support throughout my life.

Table of Contents

List of Tables

List of Illustrations

Nomenclature

Δ	Thickness of total mixing layer
Θ	Nondimensional temperature
ρ	Density
ρu	Mass flux
AS	Angle of spread of total mixing layer
$ASML$	Angle of spread of splitter plate mixing layer
d_N	Normal injection tube outside diameter
d_N^*	Normal injection tube throat diameter
H	Slot injector height (nominally ½-inch)
L	Left side (behind injection tubes)
LBM	Length before merging of splitter plate mixing layer and floor boundary layer
$\dot{m}$	Mass flow rate
M	Mach number
p	Pressure
$p_{N_{eb}}$	Normal jet effective back pressure, $0.8p_2$
$\bar{q}$	Dynamic pressure ratio, $(\rho u^2)_N/(\rho u^2)_\infty$
R	Right side (between injection tubes)
s	Normal injection tube spacing
T	Temperature
u	Velocity

W	Width of test section (9 inches)
x	Distance downstream from slot
$\tilde{x}$	Distance downstream from tubes
y	Height above floor

Subscripts

0	Stagnation quantities
1,4	Station numbers
2	Conditions behind normal shock in flow
∞	Free-stream
c	Cone static probe
e	Entrained
ex	Exit pressure
i	Initial condition (Station 1R)
N	Normal injection
T	Tangential injection

Chapter 1

Introduction

Throughout the continuing development of the Scramjet concept, the mixing of fuel and air in the combustor has been one of many important and persistent problems. In the high Mach number range of flight, combustor velocities are of the order of 10^4 ft/sec. The length of the combustor must be limited to a few feet due to the impact that the size of the combustor can have on the overall performance of a highly integrated hypersonic flight vehicle. Therefore, sufficient entrainment and subsequent micromixing followed by significant heat release must all occur in roughly 10^{-4} sec.[1] Also, both the initial entrainment and micromixing are significant problems at high Mach number due to the inherently low rate of free shear layer mixing at these conditions. Clearly, these constraints dictate increased efforts aimed at improving the understanding of high Mach number mixing and mixing augmentation.

The difficulties of achieving adequate mixing at high Mach numbers are far from being well understood. Responsible mechanisms include the effect of eddy shocklets and the effect of compressibility on turbulent mixing[1-4]. Efforts to augment high speed mixing usually revolve around three-dimensional effects aimed at increasing the total area available for mixing, the introduction of longitudinal vorticity[5], and shock interactions or oscillating shocks[2]. The understanding of efficient mixing processes also has many other applications, including thermal protection of surfaces, reduction of skin friction, and fuel-air mixing.

Many mixing augmentation schemes that are employed in subsonic flow fail to work at high Mach numbers, including the addition of swirl and acoustic noise. There are, however, several injecton schemes for supersonic flow that do show promise, including injection from a strut and injection from wall surfaces. Struts can cause blockage and large total pressure losses in the flow and are not considered in this experiment. Two common types of fluid injection from the wall of a supersonic combustor include normal injection[6,7] from circular jets, for example, and tangential injection from a rearward facing slot[8-10]. In general, the advantages of tangential injection include a film cooling effect on the wall of the combustor and relatively low free stream total pressure loss, since there is little flow disturbance. Also, since the injection is in the flow direction, significant thrust can be produced from the momentum of the injected fluid. However, without three-dimensional effects, the mixing rate is considered too slow. In comparison, normal injection is considered to have a much faster mixing rate and

the benefit of penetration into the free stream. The larger free-stream disturbance that normal injection creates can result in significant total pressure losses. Recirculation zones upstream and downstream of the injector create hot spots on the combustor wall. Also, with a normal injection scheme no thrust is derived from the momentum of the injected fuel. Injection at a downstream angle between 0 and 90° has various combinations of these advantages and disadvantages.

In this research, experimental results are presented for a design that combines both tangential and normal injection schemes in a manner that seeks to include the advantages and minimize the disadvantages of each. A fraction of the added mass flow was injected transversely to get increased penetration of a portion of the injectant into the free stream. The normal injection was from an array of tubes equal in height to and located just downstream of a slot in order to get maximum penetration while being sheltered from the hot free stream and to remove the hot recirculation zones from the surface of the slot lip. In addition, it is reasonable to expect that the combination of the disturbance of the tubes themselves, the bow shock from the normal jets, and the jets can create a favorable interaction with the free stream and slot flow to augment the mixing process above that of a slot alone.

Although a complete study of a fuel injection model should include injection of a foreign substance into the main flow, much can be learned from a "basic" study using only the injection of air. This simplifies the data reduction and the necessary equipment considerably. That plan was followed here.

Parameters varied in this experimental program included the slot and normal jet total pressures and the normal jet Mach number. The air injected normally was also heated for several cases in order to trace the path of the jet flow and measure its temperature decay in order to assess its mixing rate. Mean flow measurements of cone-static, total temperature and Pitot pressure were taken at a series of downstream stations. From this data, profiles of Mach number, density, and velocity were obtained. From the density and velocity, mass flux profiles and entrainment rates were calculated. Schlieren pictures and Nanoshadowgraphs were also taken to visualize the flowfields.

Chapter 2

Experimental Apparatus and Methods

Test Facilities

All tests were performed in the Virginia Tech Supersonic Wind Tunnel. This blowdown facility provided run times of about 13 seconds at a free-stream Mach number of 3, a total pressure of 95 psia and at a total temperature of 520°R, giving a free-stream Reynolds number of 1.57×10^7 per foot. Air is compressed by four Ingersoll Rand reciprocating compressors and held in tanks totaling 2800 ft^3. The high pressure air passed through a prefilter and dryer before entering the test section. Screens in the settling chamber were used to help flow uniformity and reduce turbulence in the free stream. The air then passes through the converging-diverging Mach 3 nozzle into the special test section, shown in Figure 1. This test section was 4.5 inches high by 9 inches wide and over one foot

long in the streamwise direction. The dimensions of the test section resemble the size of an actual scramjet combustor.

All data acquisition and tunnel control operations were handled by an IBM Personal Computer. The tunnel hydraulic control valve was computer operated and utilized feedback circuitry to accurately control the settling chamber total pressure. The computer controls make it possible to achieve very repeatable runs; typically, p_{0_∞} was kept to ± 2 psi from run to run.

Model

The combined tangential-normal injection model used is pictured in Figure 2 and Figure 3. The tangential injection consisted of a 0.475 inch high opening, rearward-facing slot injector separated from the free stream by a splitter plate 0.021 inches thick. A nominal slot height of $H = 0.5$ inches was used to nondimensionalize many of the lengths in the experiment. The contoured, converging-diverging slot injector was designed to operate nominally at a Mach number of 1.7 and total pressure of 10.7 psia. The slot total pressure was controlled by a manually operated gate valve and kept within $\pm 2\%$ of the desired pressure. The air for this injector was taken from the tunnel supply line just upstream of the settling chamber.

The normal injection came from of a row of eleven evenly spaced ($s/d_N^* = 17.4$) circular tubes located at $x/H = 0.5$ downstream of the slot. This spacing was chosen to give a three-dimensionality to the flow to increase the available mixing area over that of a 2-D planar jet. These tubes are equal in height to the slot, and inject air normal to the free-stream flow. Both sonic ($M_N = 1.0$) and supersonic ($M_N = 2.2$) jets were tested, each with a throat diameter $d_N^* = 0.043$ inches. The sonic tubes had a outside diameter of $d_N = 0.0625$ inches, while the supersonic tubes were twice as large at $d_N = 0.125$ inches. The air was supplied by a manifold of compressed air tanks and regulated by a dome regulator to within $\pm 5\%$ of the required injector total pressure. A heating unit was developed to allow normal jet total temperatures of up to 660°R to be achieved, allowing the penetration and decay of the jet to be measured. It consisted of about 80 feet of stainless steel tubing, ¼-inch in diameter, coiled to conserve space. A current of 30 amps was then passed through the coil to produce Joule resistance heating on the tube and then the air passing through the tube.

Test Matrix

The combined injector model was operated at several different operating points in order to study the effects that various parameters had on the flow. Many of the cases that showed typical trends and features are tabulated in Table 1 and

are discussed in this paper. Both the tangential and normal injection systems allowed for variable total pressures (and hence mass flows). Case (B), $M_N = 1.0$, $p_{0_N} = 350$ psia, and $p_{0_T} = 10.7$ psia, is considered to be the "baseline" case, and most other combinations of parameters are compared to this.

The tangential slot injector was run at a total temperature of 520°R and total pressures from 9.7 psia to 13.7 psia in 0.5 psi increments, resulting in exit pressures from slightly below to slightly above the free-stream static pressure of about 2.6 psia. Thus, the slot injection ranged from slightly over- to underexpanded, turning the free stream either towards or away from the wall after the step. The mean flow ρu profiles at the first station were integrated to give a baseline slot mass flow rate of 0.019 slugs/sec. Measurements were also taken for cases with the tangential slot closed, so that the mixing of the transverse jets alone could be measured.

The normal injection was run at nominal total pressures of 350 and 500 psia, referred to hereafter as the "low pressure" and "high pressure" cases. The normal mass flow was calculated after measuring the pressure change in the fixed-volume air tanks during trial runs. The baseline mass flow from these injectors was measured to be 0.0031 slugs/sec, giving a mass flow ratio $\dot{m}_N/\dot{m}_T = 0.16$. The high pressure case had a higher mass flow at $\dot{m}_N = 0.0049$ slugs/sec, or $\dot{m}_N/\dot{m}_T = 0.26$. Again, cases were run with no normal injection, so that the influence of the tubes themselves could be studied.

Optics

As mentioned previously, spark Schlieren and short duration ("nano") Shadowgraph pictures were taken of every test case. They are capable of giving both qualitative as well as quantitative information about the flow field. The Schlieren setup used is shown in Figure 4. The light source used for the Schlieren photographs was a General Radio Company Type 1531-AB Strobotac, having a flash duration of 10^{-6} seconds. For the Nanoshadowgraphs, the light source used was a Xenon Corporation Novatron-789B Nanopulse Lamp with a 20 nanosecond flash. The light beam was aimed through the test section by a collimating mirror. For the Nanoshadowgraphs, the camera was placed and focused just on the other side of the test section. For the Schlieren photos, the light beam was reflected from another collimating mirror which focused the beam on a horizontal knife edge. The light then passed to a third mirror and into the camera. All of the photographs were taken using Polaroid Type 57 film.

Mean Flow Measurement Stations

Measurements of Pitot pressure, cone static pressure, and total temperature were made at a series of nine stations in the flow. Five axial stations at

$x/H = 0.25$, 1, 4, 10, and 20, referred to hereafter as Stations 1, 1b, 2, 3, and 4, allowed the flow quantities to be measured as the mixing progressed downstream, see Figure 3. Station 1, being just downstream of the slot, was a logical choice for initial profiles to be used in subsequent calculations. Station 1b was placed just behind the normal jet tube array, and is useful for measuring initial jet properties. Station 2 is useful as it is far enough downstream to be past most of the waves and complicated flow near the slot. By Station 3, significant mixing has begun to occur and the layers are merging. By the time that the flow has reached Station 4, these layers have merged, providing profiles of mixed, well developed flow. Two transverse measuring locations were used, one directly downstream of a jet (the left side) and the other midway between two jets (the right side). Therefore, the stations are referred to, for example, as Station 1bL or Station 3R. No data could be taken at Station 1L.

Pressure Measurements

Measurement of the tunnel settling chamber total pressure was accomplished by a Pitot probe connected to a 0-100 psia Setra Systems pressure transducer. This signal was then filtered, buffered, and amplified before being sampled by the computer. The tangential slot injector total pressure was sensed by a Pitot probe in the injector manifold. It was sampled by a Pressure Systems, Inc. (PSI) Digital

Pressure Measurement System with an input pressure range of ± 15 psig. The normal injection total pressure was set by hand and read from the air tank manifold pressure gauge.

The flow cone static pressure and Pitot pressure were measured by probes (see Figure 5) mounted to a vertical traverse unit. The cone static pressure probe consisted of a 10° semivertex angle cone soldered to 0.0625 inch diameter tubing. The vertex of the cone was precision ground and maintained to within 2 arc minutes of 10°, see Figure 6. Four 0.01 inch holes separated by 90° were drilled into a common chamber, helping to reduce errors due to probe misalignment. The probe had a capture area of around 0.002 in^2 and a response time of less than 0.1 seconds. The Pitot probe was made by flattening the tip of a circular tube to a rectangular cross section with an opening of 0.0165 by 0.125 inches, giving a capture area of about 0.002 in^2. The thickness of the probe lip was approximately 0.005 inches. The cone static probe was connected to a 0-10 psia pressure transducer, while the Pitot probe used a 0-100 psia pressure transducer. The signal from each of these transducers was amplified by a Gould Model 13-4312-00 amplifier and low-pass filtered before being sampled by the computer.

Temperature Measurements

The wind tunnel total temperature was measured by use of a type K thermocouple in the settling chamber. There was no provision for measuring the slot total temperature separately. The normal injection plenum chamber was equipped with a 0.01 inch diameter type K thermocouple.

A vented thermocouple probe[11] was used to measure the total temperature in the flow. The recovery factor of this probe was measured to be 0.99.[12] The thermocouple used was a butt-welded, 0.005 inch diameter Chromel-Alumel (type K) wire having a thermal time constant of about 0.1 second. The ceramic insulating tip had an inlet opening diameter of 0.075 inches, see Figure 7.

Each of these temperature signals were passed through an Omega Engineering Thermocouple D.C. Millivolt Amplifier Model Omni-IIB. Besides amplifying the signal, these devices provided an electronic ice-point reference junction for the thermocouples. The signal was then low-pass filtered and recorded by the computer.

Probe Traverse

The three probes were traversed across the flow in the vertical direction by means of a stepper motor-driven assembly that allowed profiles to be taken at each station up to heights of $y/H = 4.0$, well into the free stream. The stepper motor used was a Lynn Products Model 3701 and its associated control circuitry. It was computer controlled and operated at a maximum vertical speed of approximately 0.2 in/sec., limited by the response times of the pressure probes.

The position of the probe and traverse was measured by the use of a linear variable differential transformer (LVDT) attached to the traverse rod. The signal from the LVDT was filtered by a 4-pole low-pass Bessel filter, amplified, and then recorded by the computer.

Data Acquisition System

The data from this experiment was collected and stored by an IBM PC equipped with a Metrabyte Model Dash-16F High Speed A/D and I/O board. The A/D section was capable of sampling 16 channels at 100 kHz with 12 bit resolution over its 10 volt input range. The data from all of the transducers used was sampled at 100 Hz. The I/O capabilities of the Metrabyte board were used

to operate the tunnel control valve, set and monitor the settling chamber total pressure, and to operate the probe traverse. Figure 8 shows a block diagram of the computer data acquisition system.

Data Reduction

The raw data was in the form of Pitot pressure p_{0_2}, cone static pressure p_c, and total temperature T_{0_2}. This data was reduced to profiles of Mach number, velocity, and density in the following manner. For $p_c/p_{0_2} < 0.4782$, the Mach number was given by a curve fit to cone static pressure tables.[13]

$$M = -1.9239X^9 + 10.117X^8 - 16.4515X^7 + 10.3343X^6 + 0.8189X^5$$
$$- 4.0485X^4 + 2.4034X^3 - 0.13574X^2 + 0.6891X + 1.19997$$

where $X = -2.86369\left(\frac{p_c}{p_{0_2}}\right) + 1.36942$. The static pressure was then found using the Rayleigh Pitot formula,

$$\frac{p}{p_{0_2}} = \left(\frac{2}{(\gamma+1)M^2}\right)^{\frac{\gamma}{(\gamma-1)}}\left(\frac{2\gamma M^2 - (\gamma-1)}{\gamma-1}\right)^{\frac{1}{\gamma-1}}$$

For regions where the free-stream Mach number was less than 1.2 (i.e., $p_c / p_{0_2} > 0.4782$), the shock wave on the cone static probe became detached, and a locally constant value of static pressure p across the shear layer in these regions

was assumed. The width of the layer for which this assumption was made was typically on the order of $0.1H$. If $p/p_{0_2} > 0.5283$, then M is subsonic, $p_{0_2} = p_{0_1}$, and the Mach number can be determined from the isentropic relation

$$M = \sqrt{\frac{2}{\gamma - 1}\left[\left(\frac{p}{p_{0_2}}\right)^{-\frac{\gamma-1}{\gamma}} - 1\right]}.$$

If $p/p_{0_2} < .5283$, then $1.0 < M < 1.2$, and p can be found by iterating the Rayleigh Pitot formula. Once the Mach number profile has been found, T_{0_2} can be used to calculate density and velocity as

$$a = \sqrt{\gamma RT} = \sqrt{\frac{\gamma RT_{0_2}}{1 + \frac{\gamma - 1}{2} M^2}},$$

$$u = a \cdot M,$$

$$\rho = \frac{p}{RT} = \frac{p_{0_2}}{RT_{0_2}}\left(\frac{2}{(\gamma + 1)M^2}\right)^{\frac{\gamma}{\gamma-1}}\left(\frac{2\gamma M^2 - (\gamma - 1)}{\gamma + 1}\right)^{\frac{1}{\gamma-1}}\left(1 + \frac{\gamma - 1}{2} M^2\right).$$

These mean density and velocity profiles could then be integrated to yield mass flux at a given station. Using the value of the total mixing layer height, Δ, measured from the Schlieren photographs, the mass flux in the total mixing layer at any station can be found from

$$\dot{m} = H \int_0^{\Delta/H} \rho u \, d\left(\frac{y}{H}\right)$$

By multiplying by the width of the test section (0.75 ft), the mass entrained into the total mixing layer can be calculated. Although this is a two-dimensional calculation done on both the left and right sides (behind and between the tubes), the average of the two sides gives a reasonable estimate of the mass entrained into the three-dimensional flow field.

Chapter 3

Results and Discussion

Photographs

Schlieren photographs and Nanoshadowgraphs were made of the injection scheme under the different operating conditions tabulated in Table 1. Many of the important flow features can be seen in these pictures in Figure 9 through Figure 14, which are half-tone reductions of the originals photographs. Since the Schlieren photos have longer exposure times than the Nanoshadowgraph, they show the mean flow features more clearly. The Nanoshadowgraphs provide a much better job of "freezing" the flow, making it easier to see the fine structure and turbulence. Also, Shadowgraphs of any time exposure show shocks more clearly, while Schlieren photographs show regions of smooth density variation more clearly. However, dimensions taken from Nanoshadowgraphs can be

misleading, since they capture transient flow features at only one instant of time. Therefore, Table 2 includes only measurements taken from the Schlieren photographs.

Figure 9 is a Schlieren photograph of the flow at baseline conditions, case (B). The flow is from left to right. The rearward facing slot can be seen at the lower left in this and later photos. The windows visible in the photographs were used to compute a scale factor so that the dimensions of flow features could be measured. Also seen is the array of normal injection tubes downstream of the slot. An adjustment shock and lip shock can be seen emanating from the splitter plate. The adjustment shock hits the floor near the injection tubes and reflects up into the free-stream. The bow shock from the normal jets is also clearly visible. The flow in the region near the injection tubes is very complex and three-dimensional and therefore shows up dark in the Schlieren photo due to the large density gradients there. Also, the Schlieren system acts to integrate these gradients across the test section, further blurring this region. However, three distinct turbulent layers can be seen growing and eventually merging downstream of the slot. The first of these is the lower wall boundary layer downstream of the slot. This layer is responsible for the wall cooling effect of the slot flow, which in a real combustor would be much cooler than the incoming supersonic air. Next going upward, is the splitter plate mixing layer coming off of the slot lip where the free stream and the slot flow begin mixing. This layer includes the incoming upstream wall boundary layer and the splitter plate wake. Above these two layers, is the jet "layer" produced by the injection through the normal tubes. Although the array

of jets is very three-dimensional, Figure 9 clearly shows the penetration and spreading of the jets as they are turned and travel downstream.

The rate at which these layers grow and merge is a prime indicator of the overall effectiveness of this injection scheme. Improved mixing schemes would be indicated by increases in in the spreading angles and thicknesses of the various layers. These dimensions, shown in Figure 2, were measured from the Schlieren photographs and are tabulated in Table 2. The distance from the floor to the top visible edge of the jet layer is referred to as the total mixing layer height, Δ. The angle of spread of this total mixing layer measured between Stations 3 and 4 is $AS_{3\text{-}4}$, while $ASML_{2\text{-}4}$ is the angle of spread of the splitter plate mixing layer, measured between Stations 2 and 4. The length before the splitter plate mixing layer and the floor boundary layer merge, nondimensionalized by H, is denoted LBM. The apparent length LBM depended somewhat on the exposure setting of the camera system, and the actual point of merging was sometimes hard to measure precisely from the photos. Hence, the values listed in the table are somewhat uncertain. General trends of this quantity, however, were consistent.

Figure 10 is a typical Nanoshadowgraph of the flow for case (A). It can be seen that the bow shock produced by the normal injection tubes is at a lower angle, since there is no normal mass flow. Also, the total mixing layer thickness, Δ, is everywhere less than the cases with normal injection, and it remains nearly constant as evidenced by the low value of $AS_{3\text{-}4}$. Note, that the flow field does not look as complicated in this Nanoshadowgraph as it did in the previous Schlieren

photograph. This is because the Shadowgraph is sensitive to the rate of change of the density gradient, while the Schlieren responds to the density gradient itself. Schlieren photographs are generally considered to be an order of magnitude more sensitive than the Nanoshadowgraph.[13] Also, the downward deflection of the free stream into the overexpanded slot flow can be seen.

Figure 11 is a Schlieren photo that shows the flow for case (D) with no normal injection, but with the array of supersonic injection tubes in place of the sonic injectors. The larger outside diameter of these tubes is clearly visible. Cases with no normal injection only have two mixing layers. Figure 12 is a Schlieren photograph of high pressure, supersonic normal injection, case (F). The jet layer is visible penetrating higher above the splitter plate mixing layer than for the sonic jets. Also visible is the spread and breakup of the jet as it becomes more turbulent. By Station 4, the jet and the splitter plate mixing layer have started to mix together. Again, it is seen in Table 2 that normal injection increases Δ and $AS_{3\text{-}4}$. Increases in Δ are to be expected due to penetration of the normal jet into the free-stream, but the increases in $ASML$, and possibly AS as well, could be due to the augmentation of mixing that the combined injection design has over tangential slot injection alone.

Figure 13 and Figure 14 show a Schlieren photograph and Nanoshadowgraph of case (G). This case is similar to case (A), but with a slightly lower value of the slot total pressure. These photos are included to show a most interesting flow feature. As can be seen in these two pictures, relatively large,

periodic eddy structures are generated in the jet plume, and to a lesser degree in the splitter plate mixing layer. These eddies were found to vary in strength with differing values of the slot total pressure. They were barely noticeable at $p_{0_T} = 10.7$ psia, and appeared most strongly around $p_{0_T} = 9.7$ psia and $p_{0_T} = 12.7$ psia. The strength of the eddies decreased on either side of these values. Measurements from Figure 13 indicate a structure angle of about 40° in the region from $x/H = 7$ downstream until the jet and splitter plate mixing layer are better mixed. In Figure 14, the fine scale turbulence of the mixing region is more evident. The angle of the eddy structures in this photo were found to be 60° near Station 3 and decreasing downstream. The diameter of these structures was on the same order as H. The Schlieren and Nanoshadowgraph photos for this case indicate an average structure diameter of around 0.6 H and average wavelength of 0.4 H. Structures found in case (I) had an average diameter of 0.5 H and an average wavelength of 0.6 H. These structures were also seen in some supersonic normal injection cases. In Table 2, it can be seen that case (G) has the largest spreading angle $AS_{3\text{-}4}$, and among the largest value of Δ_4/Δ_i. The value of LBM for this case does not decrease as might be expected, but was lower for some other cases where these structures were seen. By comparison, the spreading angles of the slot alone are very small as would be expected, since the exit pressure of the slot is almost matched to the free-stream pressure.[10,12] The disturbance that the tubes create, even without any normal mass flow, has a significant effect on the growth of the splitter plate mixing layer. This could be because the supersonic normal injection tubes have a larger outside diameter than the sonic injectors, causing the

shedding of vortices of a different size and frequency, and hopefully, more mixing of the slot flow. Case (H) has mixing layer dimensions similar to case (G), except for the value of AS_{3-4}, which is only half of the case (G) value. The eddy structures were not seen in this case. Case (I) photos also showed these large eddy structures, although it has spreading angles and mixing layer thicknesses more typical of the no injection cases (A) and (D). Case (J) did not have these structures and has spreading parameters similar to case (I).

The cases with the larger thicknesses and spreading angles shown in Table 2 indicate some important trends. First of all, it can be seen that the value of Δ_4/Δ_t and AS_{3-4} are related, since an increase in AS_{3-4} generally leads to a larger value of Δ_4 (see Figure 2). Likewise, an increase in $ASML_{2-4}$ leads to a decrease in LBM. The value of $ASML$ and LBM are influenced by the interaction of the jet and splitter plate mixing layers. For the sonic, $p_{0_T} = 10.7$ cases, (A)-(C), the value of $ASML_{2-4}$ increases with the addition of normal injection. The low pressure case had an increase of 109% over the no normal injection case, while the high pressure case was just 82% larger. This may be due to the fact that the high pressure jet penetrates the incoming boundary layer farther, and hence mixes with it slightly less than the low pressure jets. By Station 1, the baseline sonic jet had a penetration of only 1.4 H, while the baseline supersonic jet penetrated over 1.6 slot heights. The incoming boundary layer was on the order of 0.6 H, so that its outer edge is at 1.6 H. Farther downstream, the sonic jet still had not penetrated much beyond this, while the supersonic jet had reached a height of almost 2 H. For the supersonic jet cases, (D)-(F), as well as the sonic

cases (G) and (H), there is little change in the value of $ASML_{2-4}$. The values of $ASML_{2-4}$ for cases (I) and (J) are about the same as for the no normal injection cases. The values of LBM for these cases follow similar trends.

The trends of AS_{3-4} and Δ_4/Δ_t may give a better indication of mixing, since they represent the growth of the entire mixing layer. These values are strongly influenced by the penetration of the jet and its interaction with the incoming boundary layer. Again, the values in Table 2 indicate an increase in the spreading angle AS_{3-4} and thickness Δ_4/Δ_t with the addition of normal injection. Low and high pressure sonic injection increased AS_{3-4} by 20% and 40%, respectively, over the no normal injection case, while Δ_4/Δ_t increased by 64% and 55%. For cases (D)-(F), the supersonic normal injection decreased AS_{3-4} by 20% for the low pressure case, and increased it by 50% in the high pressure case compared to the no normal injection case. Δ_4/Δ_t was increased only 17% and 25%, respectively, for these cases. However, for case (G) in the presence of the large eddy structures, AS_{3-4} increased 54%, while Δ_4/Δ_t increased 18% over the corresponding no normal injection case. For case (I), the value of AS_{3-4} is around the same as for the other sonic low pressure cases. Δ_4/Δ_t for this case is also not increased above the other cases. Case (J) had very similar dimensions. Notice that the slot alone flow dimensions show less mixing than practically every other case, even the ones without normal injection. From these photographic results, it can be concluded that the sonic, low pressure injection produced the best combination of spreading angles and mixing layer growth. The presence of the large eddy

structures seemed to produce an increase only in AS_{3-4}, not in the total mixing layer thickness.

Mean Flow Profiles

The raw pressure and temperature data were reduced as discussed earlier, and are plotted versus the height above the lower wall. The velocity and density profiles were nondimensionalized by their local free stream values. Dimensional profiles of these quantities can be found in Appendix A. This section will concentrate mainly on descriptions of the Mach number profiles, since the velocity and density profiles usually show similar features.

Profiles for case (A) are shown in Figure 15 through Figure 20. Figure 15 is a plot of Mach number versus the height above the floor at Stations 1bL through 4L for case (A). Recall that the left side stations are located behind the tubes and the right side stations are between the tubes. The incoming freestream and slot flows are visible at Station 1b, although somewhat disturbed, since this station is close behind the the normal injection tubes. As the flow proceeds to Stations 3 and 4, the profiles smooth somewhat and approach a fully developed shape. Figure 18 shows a much cleaner free stream and slot flow at Station 1 on the right side between the tubes. From this profile, it is seen that the slot Mach

number is less than the nominal value of 1.7. The initial free stream boundary layer is about 0.6 H thick. The lower wall boundary layer as well as the splitter plate mixing layer and wake are easily recognized. Also, the slot flow does not merge with the free stream as well as on the right side, the profile being less fully developed by Station 4; compare Station 4 results in Figure 15 and Figure 18. The data from this station (1R) was used as an initial condition in later entrainment calculations. Δ_i was typically around 1.6 H. At Station 2 in Figure 18, the presence of the bow and lip shocks are seen at $y/H \simeq 2.7$ and 2.0, respectively. These two features were are seen on many Station 2 profiles, and they match up well with dimensions taken from the Schlieren photographs.

Figure 21 through Figure 26 are profiles of case (B). In Figure 21, it can be seen that there is a region near $y/H \simeq 1.3$ where the Mach number is indicated to be zero at Station 1b. This occurs only on the left side profiles in the cases with normal injection. In this region, the calculated total pressure was found to be less than the assumed locally constant value of static pressure, a situation that is clearly impossible. This leads to the conclusion that perhaps flow angularity at this point directly behind the normal jet makes the measurement and data reduction techniques discussed earlier invalid. We believe these problems are mainly with the cone static probe. Of course, this problem shows up in the velocity and density profiles for these cases also (e.g., see Figure 22 and Figure 23). Notice that the higher normal jet density is clearly visible at Station 1b in Figure 23. These large density peaks were found to quickly dissipate by Station 2, indicating that the jets have already spread substantially by that

station. Again, on the right side (Figure 24), the incoming freestream and slot flows are clearly visible. In Figure 21, the jet and splitter plate mixing layers are visible at Station 2 as a peak in the Mach number profile. The location of this peak agrees with the Schlieren photograph of this case, Figure 9. By Station 4, the flow is more fully developed than in case (A). By comparing the right and left side profiles at Station 3 and 4, one effect of the normal jets can be seen. The slot region is fuller for the flow between the jets. On the left side behind the tubes, the jet has pushed the region between the free stream and slot flow upwards. This will be discussed again in the entrainment section below.

The profiles for case (C), Figure 27 through Figure 32, are very similar to the profiles presented for case (B). The main difference seems only to be a slight increase in the penetration of the jet layer.

For the rest of the cases, (D) through (J), data is presented for Stations 4L and 4R only. In Figure 33, case (D), the left and right profiles at Station 4 are similar. There is no normal injecton in this case, although the larger diameter supersonic tubes are in place. The total mixing layer thickness is slightly higher on the right side between the tubes. In case (E), Figure 36, the total mixing layer thickness is increased on the left side by the addition of low pressure normal injection. Again, the right side profile looks more fully developed than the left side, but with a smaller total mixing layer thickness, Δ. Case (F) profiles, shown in Figure 39, are very similar to case (E) profiles, except for the slightly increased penetration behind the tubes due to the higher jet total pressure.

In Figure 42, profiles are shown for case (G) which showed strong eddy structures in Figure 13. One result of these large structures was to increase the total mixing layer thickness, Δ , visible in Figure 42 on the left side. The right side profile is also more fully developed for this case than for other cases with normal injection, but without the strong eddies. In Figure 45, case (H), Mach number profiles are similar to case (G) in shape, but they do not have the increased mixing layer thickness found in case (G).

Figure 48, case (I), shows the Mach number profiles for another case where the large eddy structures were seen in Schlieren and Nanoshadowgraph photos. They are very similar to cases (G) and (H), but with smaller increases in the spreading angles and total mixing layer thickness, shown in Table 2. The Mach number profiles for case (J) are similar to case (H). This case has a total mixing layer thickness close to that of the other cases with supersonic normal injection.

Most of the mean flow profiles (except for ρu) computed for different slot and jet total pressures were similar in their basic shape at a given station, and seemed to be relatively insensitive to these parameters as they were varied.

Entrainment

A measure of the mixing that occurs in this, or any, design is the amount of free-stream air that is entrained into the total mixing layer. Typical mass flux profiles at Station 4 have been plotted in Figure 54 through Figure 63. The different layers in the flow have merged and penetrated into the free stream somewhat by this station.

Mass flows were computed at the slot face (Station 1R) and at Station 4 by integrating the mean flow ρu profiles across the total mixing layer. For the cases without normal injection, (A) and (D), Figure 54 and Figure 57, there are only small differences between the left and right sides in the ρu profiles at Station 4. There are significant differences, however, for both the low and high pressure injection cases ((B),(C),(E)-(J)). At first glance, it seems that the ρu profiles for the right side are more fully developed, having a larger integrated mass flux. But, the values of the total mixing layer thickness, Δ , for the left side are always larger than on the right side, giving a larger height of integration and making up for the apparent mass flux deficit seen in the profiles. Values of Δ for use in these calculations were taken as 99% of the local free stream velocity. These values taken from the left side agreed very closely to values measured from the Schlieren photographs. However, total mixing layer thicknesses from the right side profiles were lower than in the photographs. This is because the flow is not two-dimensional even at Station 4 due to the large lateral jet spacing

($s/d_N^* = 17.4$), and the photographs indicate only the thickest part of the total mixing layer. It is expected, then, that Δ will be larger and that more mixing will occur directly behind the tubes, since the losses associated with the tube drag and wake usually enhance mixing. By taking the difference between the mass flow at Station 4, $\dot{m}_4$, and the sum of the mass flows at $x/H = 0$ and the normal injected mass flow, $\dot{m}_l + \dot{m}_N$, the mass flow entrained into the total mixing layer across the width of the test section, $\dot{m}_e$, could be obtained, see Figure 64. The results of these calculations are shown in Table 3.

In this section, the performance of each case will be compared to the slot alone configuration. First, it is interesting to note that the entrained mass flow $\dot{m}_e$ for the slot alone is greater than for the case with tubes but no normal injection. This suggests that there are some losses associated with flow over the array of tubes. Some estimates of these losses can be made. First, the thrust due to the slot flow was calculated in a similar fashion to the mass flow calculations discussed above. For the baseline case (B), the slot thrust was calculated to be 22.9 lb. For the drag on the array of tubes, a drag coefficient of 1.45 for an infinite cylinder was used.[14] This gave a drag of only 0.17 lb per sonic tube, and 0.34 lb for the larger supersonic tubes. For the entire array of eleven tubes, then, a maximum drag of 3.7 lb was obtained. Thus, the tube array drag is seen to be only 16.3% of the slot thrust. Although this loss is not negligible, it is less than the gains achieved by increased mixing. This will be shown below. Another "loss" might be in the interaction of the turbulence produced by the tube array and that in the mixing layers. The scale of the tubes is a tenth of the scale of the incoming boundary

layer and the largest eddy structures. Thus, the tubes themselves will not help in the production of these eddies. More likely, the tubes contribute to the break up of these large structures, enhancing the micromixing but decreasing the large-scale entrainment and mixing. Another measure of the losses associated with the normal injection arrangement the total pressure drop across the tube/jet bow shocks. For the no normal injection cases, the free stream total pressure at Station 2 was calculated to be 86.7 psia, for a total pressure drop of 9.2%. For the baseline low pressure injection cases, the Station 2 total pressure was 90.9 psia, a drop of only 4.8%. Clearly, then, the gains from this injection scheme can outweigh the losses.

It can be seen that for the cases with no normal injection, (A) and (D), there is little difference between $\dot{m}_e$ for the left and right sides. The supersonic jet case (D) has a slightly higher value, possibly due to a greater disturbance caused by the larger injection tube diameter. However, when sonic normal injection is introduced, cases (B) and (C), the entrained mass increases 194% compared to the slot alone for the low pressure case, and 206% for the high pressure case. The supersonic jets, cases (E) and (F), increased $\dot{m}_e$ only 62% and 95% compared to the slot alone for the low and high pressure cases. What is perhaps more surprising is that the normal injection also increased the entrainment on the right side, between the jets. In most cases, the right side showed a larger amount of mass entrained than the left side behind the jets. If the right and left side values are averaged, it is seen that the sonic injection increased $\dot{m}_e$ by 206% and 244%

for cases (B) and (C) compared to the slot alone, while the Mach 2.2 supersonic jets increased it by 141% and 175% over the slot alone for cases (E) and (F).

The entrained mass flow for case (G), when the large eddy structures were present, shows a very large increase on the left side downstream of the tubes. The mass entrained in this case is about 2.3 times as large as the slot alone case[12] in the last row of Table 3. However, case (I) also had large eddy structures present in the jet layer, but did not show as large an increase in entrainment as case (G). Case (J), like case (H), did not show evidence of the structures and had average values of entrained mass. Even the combined injection cases without evidence of large eddy structures show an increase in entrained mass over the slot alone.

This data shows that entrainment of the free stream is greatly improved by use of the combined tangential-normal injection over the slot alone, especially at conditions where the turbulent eddy structures are present. The effectiveness of the tubes with normal injection compared to that without injection can be rationalized with the observation that the scale of the underexpanded jet plumes is much larger than that of the tubes and is of the same order of the large scale structures in the mixing layers.

Crocco and Lees[15] have estimated that the mass entrained into a 2-D boundary layer-like flow is given by

$$\frac{d\dot{m}_e}{dx} \simeq c(\rho u)_\infty,$$

where $0.01 < c < 0.03$. For $c = 0.02$, this gives a value of $d\dot{m}_e/dx = 0.047$ slugs/sec/ft^2. Across the 9-inch (0.75 ft) width of the test section, there would be $(0.047)(0.75) = 0.035$ slugs/sec/ft entrained into the mixing layer. Between Stations 1 and 4 (0.82 ft), the entrained mass would be 0.029 slugs/sec. This is slightly less than that found in the slot alone data in Table 3.

Except for varying the strength of the eddy structures and the subsequent mass that they help entrain, the slot total pressure seemed to have little effect on the rest of the flowfield. The effect of p_{0_T} is essentially that it adjusts the deflection of the free stream into the slot flow, changing the interaction of the slot flow with the tube/jet array. Again, some structure was observed for certain supersonic jet cases, resulting in a higher entrained mass flow. The supersonic jet cases without structures showed no significant increase over the sonic cases. All of this suggests that the scale of the added flow features with the tube/jet array and their location with respect to the other mixing layers are very important if one wishes to obtain mixing augmentation.

Jet Penetration and Decay

Total temperature profiles of heated normal injection taken downstream allowed the determination of the jet trajectory and temperature decay along the

jet centerline. The decay of the peak jet temperature along the centerline gives a measure of entrained into the jet plume. When looking at the jet flow and its decay, the downstream stations are better described by their distance from the jet tubes, not from the slot. The left side stations 1bL through 4L are located at $\tilde{x}/d_N^* = 6$, 41, 111, and 227 respectively. The temperature profiles have been nondimensionalized as

$$\Theta \equiv \frac{T_{0_2} - T_{0_\infty}}{T_{0_N} - T_{0_\infty}},$$

which is a measure of the local total temperature increase due to the heated normal jet. These profiles are given in Figure 65 through Figure 72. They show the jet widening and its centerline temperature decreasing as the flow progresses downstream and cooler air is mixed into the jet. In the cases with normal injection, a second temperature peak can be seen below that of the jet plume, indicating that some of the heated jet mass flow is entrained in the splitter plate mixing layer immediately downstream of the tubes.

The jet trajectory and penetration into the free-stream could be determined from the height of the peak jet temperature. Close agreement was found between these measurements and data computed from the JETPEN (JET PENetration) computer program[16] developed at the Johns Hopkins University Applied Physics Laboratory, especially as the jet progressed downstream. Figure 73 is a typical plot of these trajectories. They also agreed well with measurements taken from the Schlieren photographs.

Figure 74 is a plot of the maximum jet temperature decay for cases (B), (E), (G), (H), (I) and (J), as well as for two cases with no tangential slot injection. It can be seen that there are two distinct regions of differing slopes, indicating two regions of exponential decay. The upstream region extends from the injection tubes to about 40 d_N^* downstream and is characterized by a slower rate of mixing than in the downstream region. Better initial mixing is seen to be produced by the higher jet expansion ratio $p_{N_{ex}}/p_{N_{eb}}$ found in the sonic cases (see Table 1), where $p_{N_{eb}}$ is an "effective back pressure". This is true for the jet alone cases as well as the combined tangential-normal cases. This parameter indicates how well the jet is matched to the exit conditions behind the bow shock. Since the supersonic jets have a value of $p_{N_{ex}}/p_{N_{eb}}$ closer to unity, they cause less disturbance to the flow, and hence, reduced interaction. The effect is less for the combined cases, because, for equal expansion ratios, the slot flow would also increase initial mixing. The effect of the jet to free stream dynamic pressure ratio, $\bar{q}$, is similar; when $\bar{q}$ is higher (i.e. the supersonic cases), the jet penetrates beyond the incoming boundary layer and interacts with it less. The normal jet momentum flux ratio seems to have little effect on the jet decay. The higher mass flux ratios of the sonic cases may account for some of the increased initial mixing. Similar trends exist for the splitter plate mixing layer decay, shown in Figure 75.

The apparent switch from an upstream mixing region to a downstream mixing region occurs at the point where the jet has lost most of its normal momentum. This increase in mixing rate could be due to the fact that the flow is then locally more like a coaxial mixing process. The rate of decay in the downstream region

may be due to the difference in axial momentum in this region. The point at which the sonic cases seem to flatten out ($\tilde{x}/d_N^* \simeq 100$) is where the jet axial momentum has approached that of the free stream.

Overall, the combined tangential-normal cases have faster initial mixing and somewhat faster downstream decay rates than do the slot or normal jets alone, resulting in significantly shorter lengths to reach desired mixing levels. Sonic jet cases seem to produce faster initial mixing than do supersonic jet cases. However, sonic injection mixing rates tend to flatten out after $\tilde{x}/d_N^* \simeq 225$, where the supersonic jet cases begin to produce faster mixing rates. There were no clear differences between the various slot total pressures tested, and the baseline value of $p_{0_T} = 10.7$ psia is probably satisfactory from a design standpoint.

The decay rates in the splitter plate mixing layer are also shown in Figure 74. The trends are similar to those discussed above, although there seems to be less difference between the sonic and supersonic jets until the downstream region is reached. In the downstream region, however, the sonic jets produced far superior mixing in contrast to the situation in the jet plume flow above.

Chapter 4

Conclusions and Recommendations

Conclusions

This experimental program was aimed at determining whether combined tangential-normal injection would have faster mixing rates than a tangential slot injector alone. The data presented here shows that, indeed, the combined injection scheme is to be preferred over the slot alone.

From the photographic evidence, it was shown that the low and high pressure, sonic normal injection cases gave the largest improvement in total mixing layer thickness (an average of 60% improvement over the slot alone case) and in total mixing layer spreading angle AS_{3-4} (an average of 30% improvement over the slot alone). Apparently, most of the gain in mixing is achieved by going from no

normal injection to the low or high pressure case. The slight additional initial penetration of the jet into the free-stream in the supersonic normal injection cases does not seem to increase the spreading angles or total mixing layer thickness substantially.

The analysis of the mean flow profiles by themselves does not give much in the way of quantitative data, but important flow features were identified from them and corroborated with photographic results.

The entrainment calculations indicate that the high pressure sonic injection cases gave the largest increase in the amount of free stream air entrained into the mixing layers. Up to 92% more mass was entrained compared to the slot alone case. The large eddy structures observed have been shown to be very desirable aids to mixing and entrainment. When they were present in the jet flow, the entrained mass in that region increased substantially.

Results of the jet decay analysis again show that sonic normal injection is to be preferred over supersonic injection, with no real bias towards the low or high pressure cases.

Each of the different parts of this experimental analysis gives a different piece of the larger puzzle. Put together, it seems clear that this combined tangential-normal injection model shows considerable improvement over the slot injector alone, and has great promise for further development and use.

Recommendations

Although it is clear from the results of this study that the combined tangential-normal injection is an improvement over the slot injection alone, the question still remains as to whether the improvement is merely the effect of adding normal injection to the slot injection, or if the combined case is "greater than the sum of its parts." In other words, does some sort of synergistic process take place between the tangential and normal flows? This is not an easy question to answer from the current data. The analysis presented here was designed to be a basic study in order to determine if this was a feasible injector scheme compared to a slot alone injector. Further experiments are called for in which more detailed measurements should be taken. In order to better understand the 3-D effects of the jets and jet spacing on the increase in available mixing area, data profiles should be taken at more than two transverse positions. In this way, a better picture of the jet and slot decay and spreading can be obtained. Further study also seems to be indicated in order to discover more precisely what combination of parameters produces the large, turbulent eddy structures sometimes found in the jet. Also, the use of heated air in the slot should be investigated to better understand the spread of the slot mass flow in the presence of normal jets. (A slot flow heating unit was under construction at the time of these experiments, but was not completed in time to be included.) Lastly, in order to produce a more realistic scheme, helium should be tested as the injected

fluid. This would give a more realistic density ratio, and would allow concentration measurements to be taken.

References

1. Ferri, A., "Supersonic Combustion Progress," *Astronautics and Aeronautics*, August 1964.

2. Kumar, A., Bushnell, D.M., and Hussami, M.Y., "A Mixing Augmentation Technique for Hypervelocity Scramjets," AIAA Paper 87-1882.

3. Papamoschov, D. and Roshko, A., "Observations of Supersonic Free-Shear Layers," AIAA Paper 86-0162.

4. Bogdanoff, D.W., "Compressibility Effects in Turbulent Shear Layers," *AIAA Journal*, Vol. 21, No. 6, pp.926-27.

5. Hersch, M. and Povinelli, L.A., "Injection into a Supersonic Stream from the Windward Side of Sweptback Injectors at Angle of Attack," *Journal of Spacecraft and Rockets*, Vol. 8, No. 10, 1971, pp.1101-3.

6. Rogers, R.C., "Mixing of Hydrogen Injected From Multiple Injectors Normal to a Supersonic Airstream," NASA TND-6476, Sept. 1971.

7. Schetz, J.A. and Billig, F.S., "Penetration of Gaseous Jets Injected into a Supersonic Stream," *Journal of Spacecraft and Rockets*, Vol. 3, No. 11, Nov. 1966, pp.1658-65.

8. Kenworthy, M. and Schetz, J.A., "An Experimental Study of Slot Injection into a Supersonic Stream," *AIAA Journal*, Vol. 11, May 1973, pp.585-86.

9. Schetz, J.A. and Gilreath, H.E., "Tangential Slot Injection in Supersonic Flow," *AIAA Journal*, Vol. 5, No. 12, 1967, pp.2149-54.

10. Walker, D.A., Campbell, R.L., and Schetz, J.A., "Turbulence Measurements for Slot Injection in Supersonic Flow," AIAA Paper 88-0123, presented at the 26th Aerospace Sciences Meeting, Jan. 11-14, 1988, Reno, Nevada.

11. Winkler, E.M., "Design and Calibration of Stagnation Temperature Probes for Use at High Supersonic Speeds and Elevated Temperatures," *Journal of Applied Physics,* Vol. 25, No. 2, Feb. 1954.

12. Smith, B.R., "Mean Flow Measurements of Heated Supersonic Slot Injection into a High Reynolds Number Supersonic Flow," M.S. Thesis, Virginia Polytechnic Institute and State University, 1989.

13. Volluz, R.J., "Handbook of Supersonic Aerodynamics," Section 20, "Wind Tunnel Instrumentation and Operation," NAVORD Report 1488, Vol. 6, Jan. 1961.

14. Hoerner, S.F., *Fluid Dynamic Drag,* published by the author, 1965.

15. Crocco, L., and Lees, L., "A Mixing Theory for the Interaction Between Dissipative Flows and Nearly Isentropic Streams," *Journal of the Aeronautical Sciences,* Vol. 19, October 1952, pp.649-76.

16. JETPEN: Jet Penetration Analysis computer program, Johns Hopkins University, Applied Physics Laboratory, 1987, based on Billig, F.S., Orth, R.C., and Lasley, M., "A Unified Analysis of Gaseous Jet Penetration," *AIAA Journal,* Vol. 9, No. 6, 1971.

Tables

	M_N	p_{0N}	p_{0T}	$\frac{u_T}{u_\infty}$	$\frac{(\rho u)_T}{(\rho u)_\infty}$	$\bar{q}$		$\frac{p_{Nex}}{p_{Neb}}$	$\frac{u_N}{u_\infty}$		$\frac{(\rho u)_N}{(\rho u)_\infty}$	
jet temp.	both	both	both	both	both	cold	hot	both	cold	hot	cold	hot
Case (A)	1.0*	—	10.7	0.75	0.36	—	—	—	—	—	—	—
(B)	1.0	350	10.7	0.75	0.36	7.0	7.9	8.6	0.51	0.54	13.7	14.6
(C)	1.0	500	10.7	0.75	0.36	11.4	12.8	12.3	0.51	0.54	22.3	23.7
(D)	2.2*	—	10.7	0.75	0.36	—	—	—	—	—	—	—
(E)	2.2	350	10.7	0.75	0.36	6.1	6.8	1.5	0.87	0.93	6.9	7.3
(F)	2.2	500	10.7	0.75	0.36	9.8	11.0	2.2	0.87	0.93	11.1	11.8
(G)	1.0	350	9.7	0.75	0.32	7.0	7.9	8.6	0.51	0.54	13.7	14.6
(H)	2.2	350	9.7	0.75	0.32	6.1	6.8	1.5	0.87	0.93	6.9	7.3
(I)	1.0	350	12.7	0.75	0.42	7.0	7.9	8.6	0.51	0.54	13.7	14.6
(J)	2.2	350	12.7	0.75	0.42	6.1	6.8	1.5	0.87	0.93	6.9	7.3

Table 1. Matrix of test conditions.: * denotes presence of jet tubes but no normal mass flow.

Case	Δ_i/H	Δ_4/Δ_i	$ASML_{2-4}$	AS_{3-4}	LBM
(A)	1.6	1.1	1.1°	1.5°	16
(B)	1.3	1.8	2.3°	1.8°	13
(C)	1.5	1.7	2.0°	2.1°	14
(D)	1.7	1.2	1.1°	1.0°	22
(E)	1.7	1.4	0.9°	0.8°	20
(F)	1.7	1.5	1.1°	1.5°	19
(G)	1.6	1.5	1.3°	2.0°	18
(H)	1.5	1.6	1.2°	1.0°	19
(I)	1.6	1.5	1.1°	1.7°	20
(J)	1.6	1.5	1.2°	1.4°	18
slot alone	1.7	1.1	0.5°	1.4°	23

Table 2. Parameters measured from photographs: slot alone data is from Smith.[12]

Case	Side	$\dot{m}_4 \cdot W$	$\dot{m}_i \cdot W$	$\dot{m}_N$	$\dot{m}_e \cdot W$	$\frac{\Delta \dot{m}_e \cdot W}{\Delta x}$
(A)	L	0.050	0.035	—	0.016	0.019
(A)	R	0.049	0.035	—	0.014	0.017
(B)	L	0.088	0.038	0.003	0.047	0.057
(B)	R	0.080	0.038	—	0.043	0.052
(C)	L	0.089	0.036	0.005	0.049	0.056
(C)	R	0.091	0.036	—	0.056	0.068
(D)	L	0.056	0.035	—	0.021	0.026
(D)	R	0.046	0.035	—	0.011	0.013
(E)	L	0.074	0.038	0.003	0.034	0.041
(E)	R	0.082	0.038	—	0.044	0.053
(F)	L	0.082	0.036	0.005	0.041	0.050
(F)	R	0.085	0.036	—	0.049	0.060
(G)	L	0.101	0.036	0.003	0.063	0.077
(G)	R	0.083	0.036	—	0.047	0.057
(H)	L	0.077	0.036	0.005	0.038	0.046
(H)	R	0.079	0.036	—	0.044	0.053
(I)	L	0.085	0.041	0.003	0.041	0.050
(I)	R	0.084	0.041	—	0.043	0.052
(J)	L	0.084	0.041	0.005	0.038	0.046
(J)	R	0.091	0.041	—	0.050	0.061
slot alone		0.074	0.041	—	0.033	0.040

Table 3. Results of mass entrainment calculations: slot alone data is from Smith.[12]

Figures

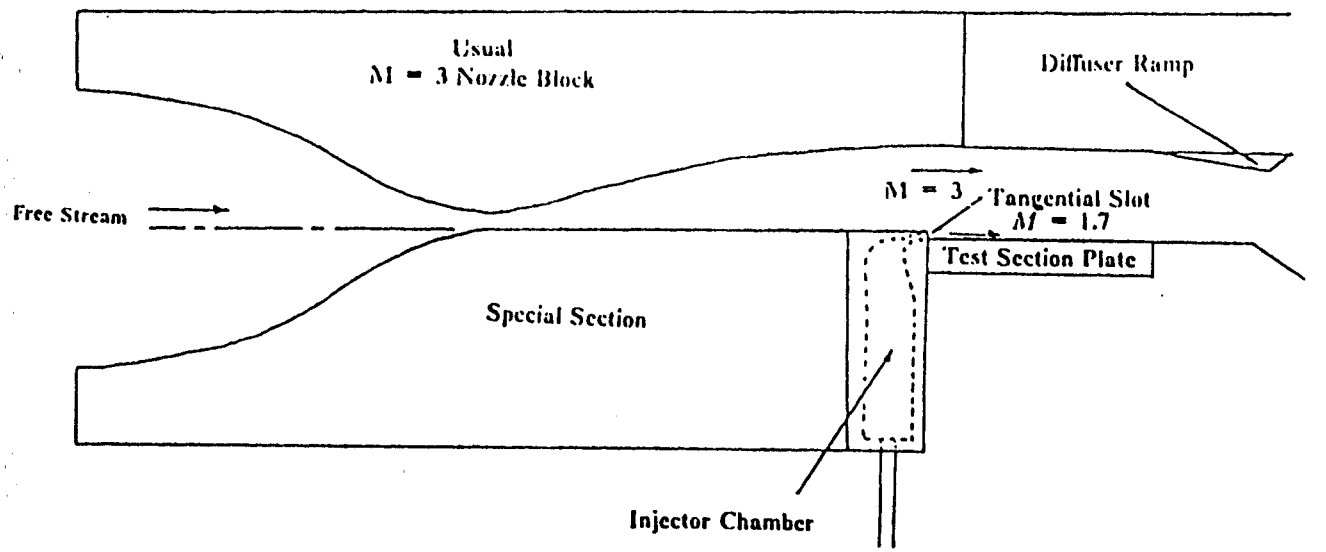

Figure 1. Virginia Tech Supersonic Wind Tunnel test section

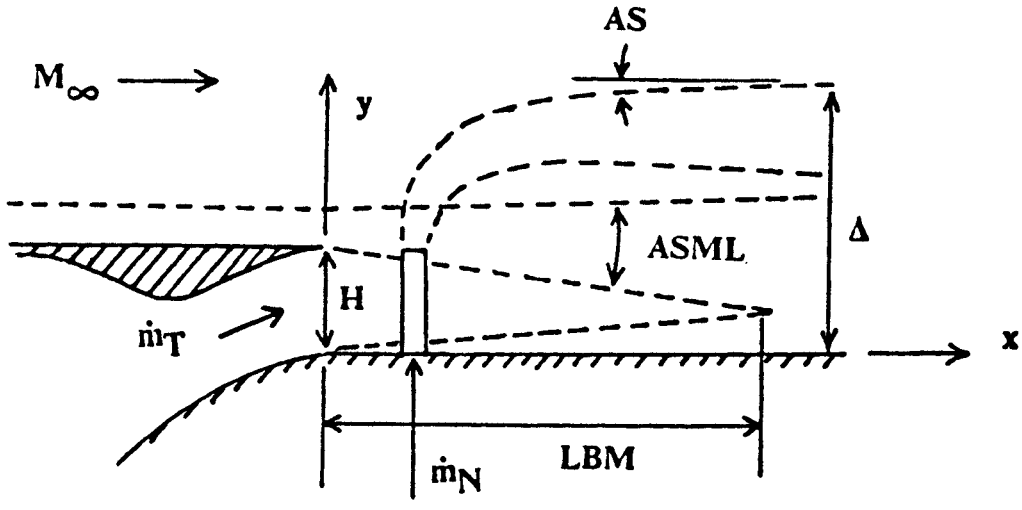

Figure 2. Combined injection model, side view: not to scale

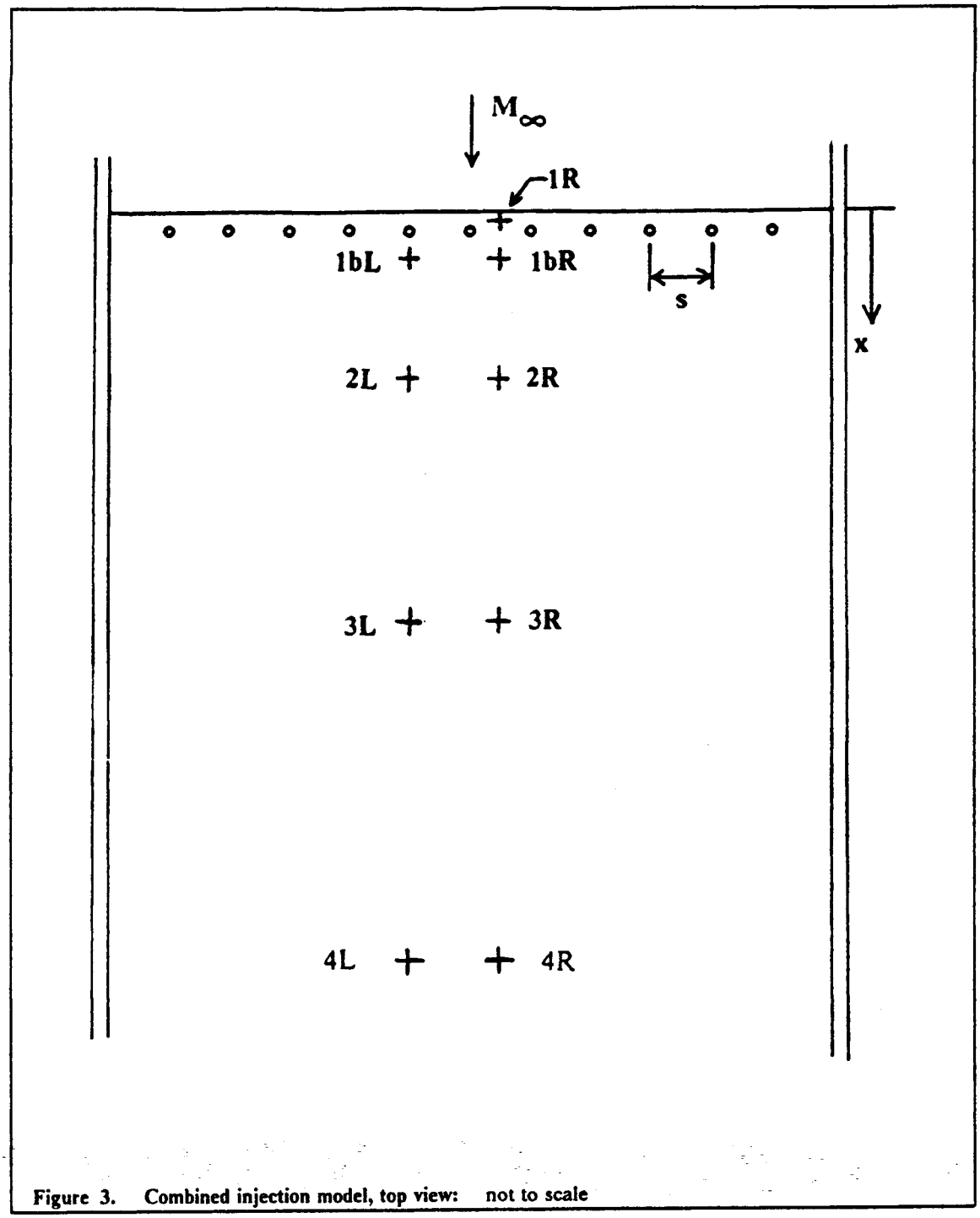

Figure 3. Combined injection model, top view: not to scale

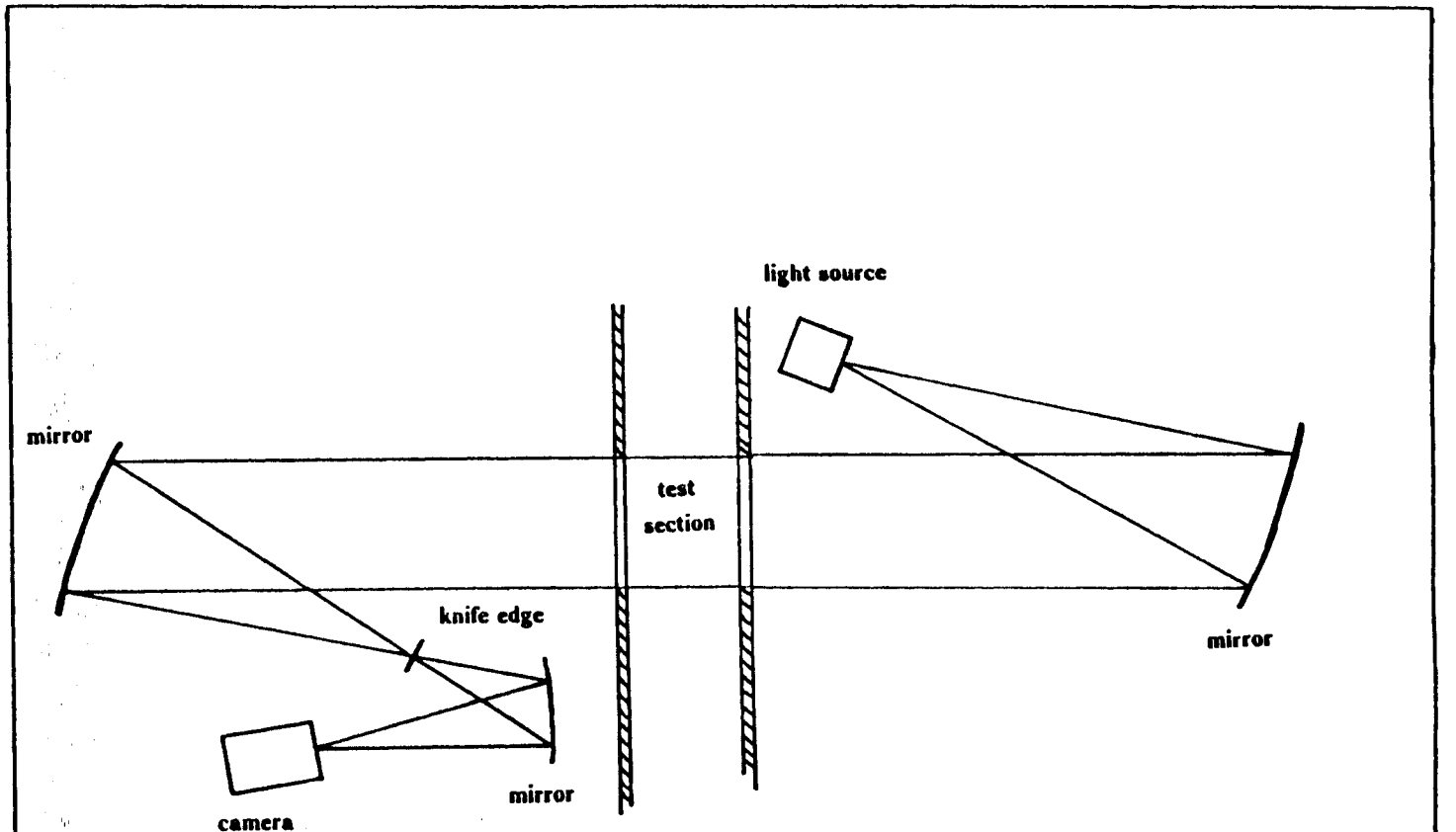

Figure 4. Schlieren photography equipment arrangement

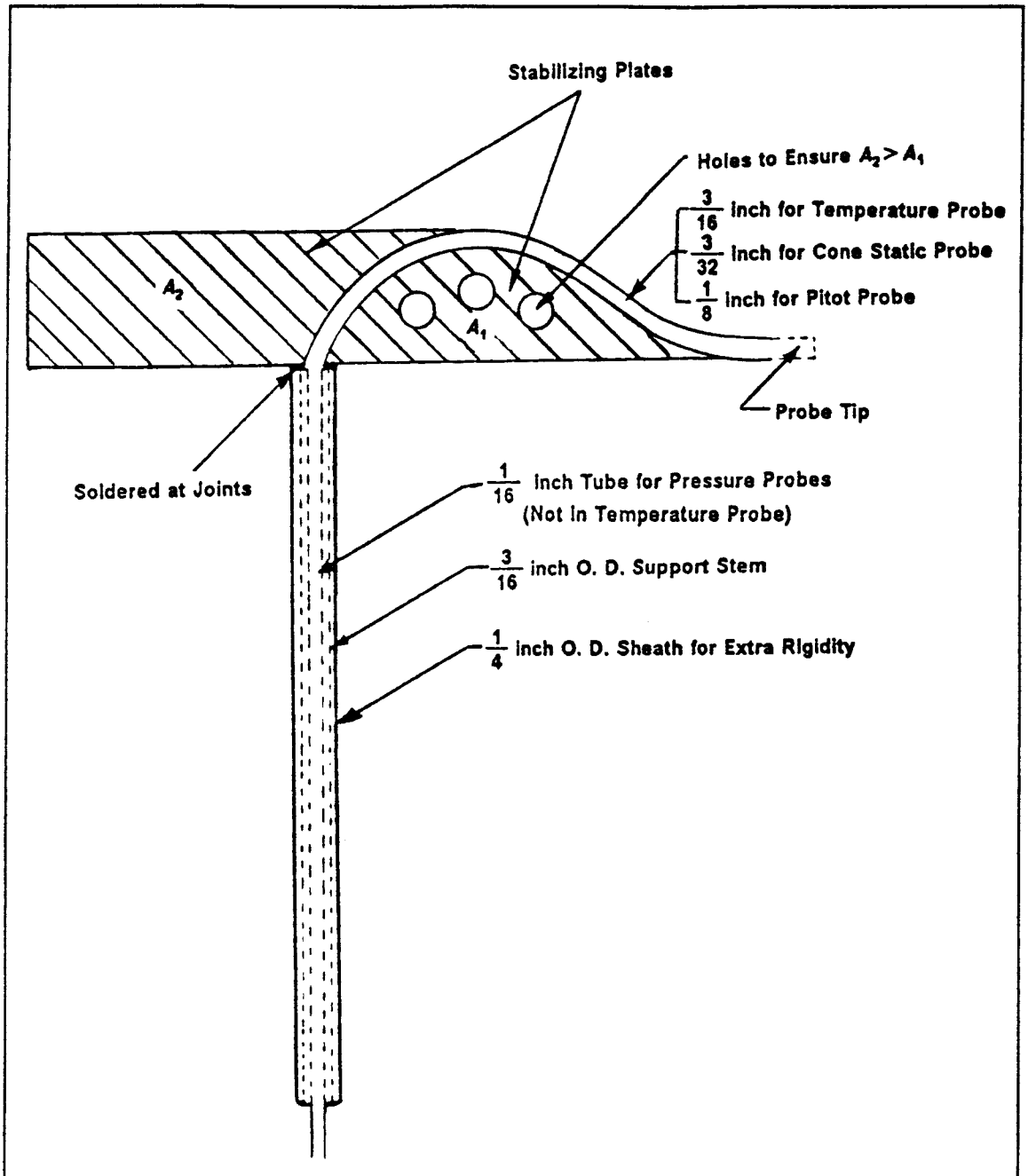

Figure 5. Details of the probe assembly: this design is common to all three probes

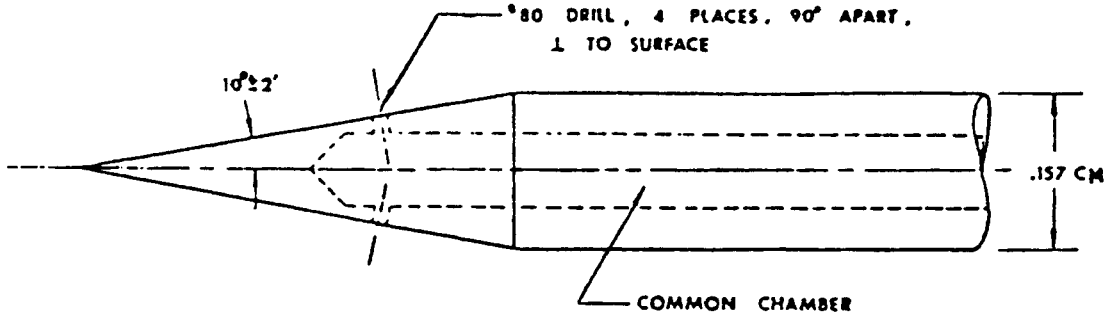

Figure 6. Details of cone static pressure probe tip

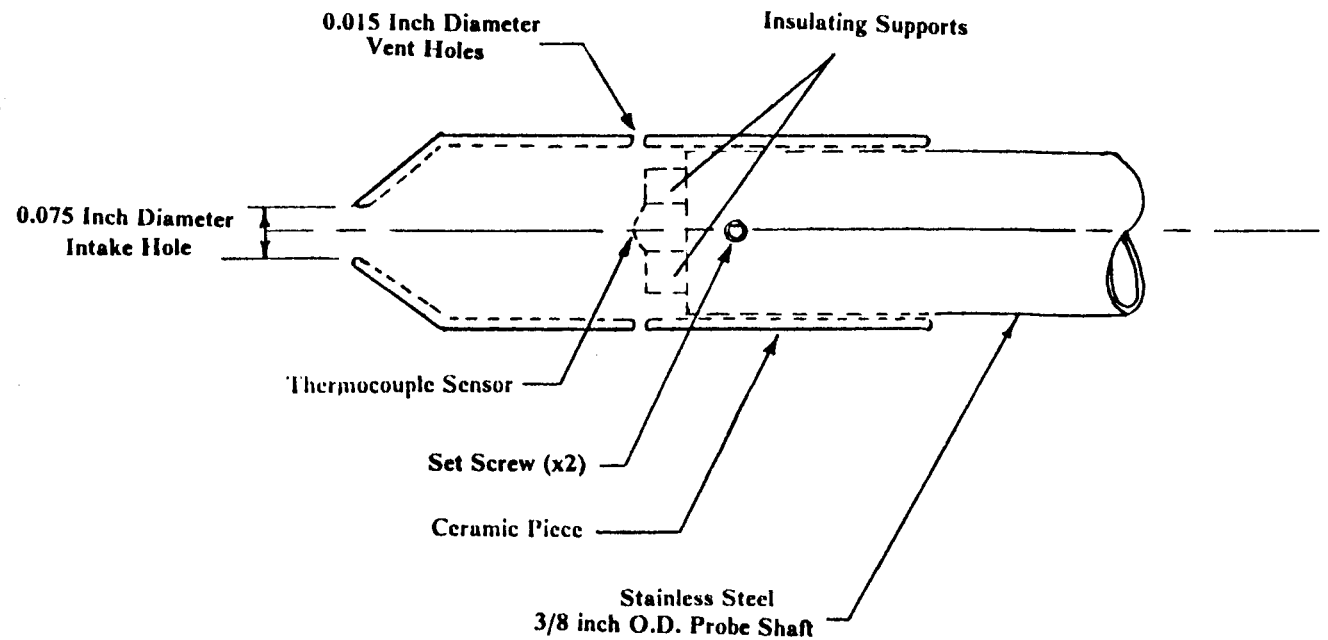

Figure 7. Details of thermocouple total temperature probe tip

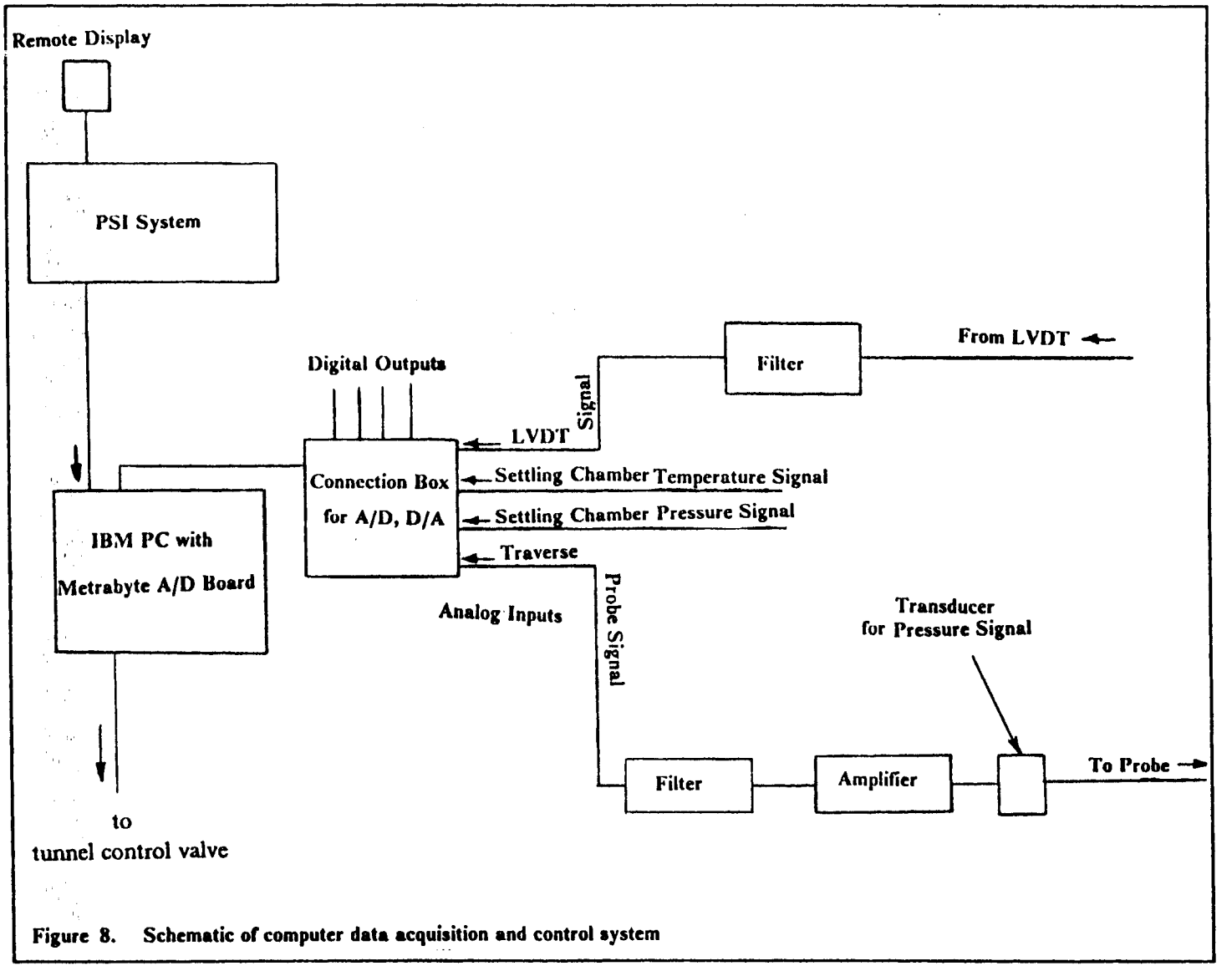

Figure 8. Schematic of computer data acquisition and control system

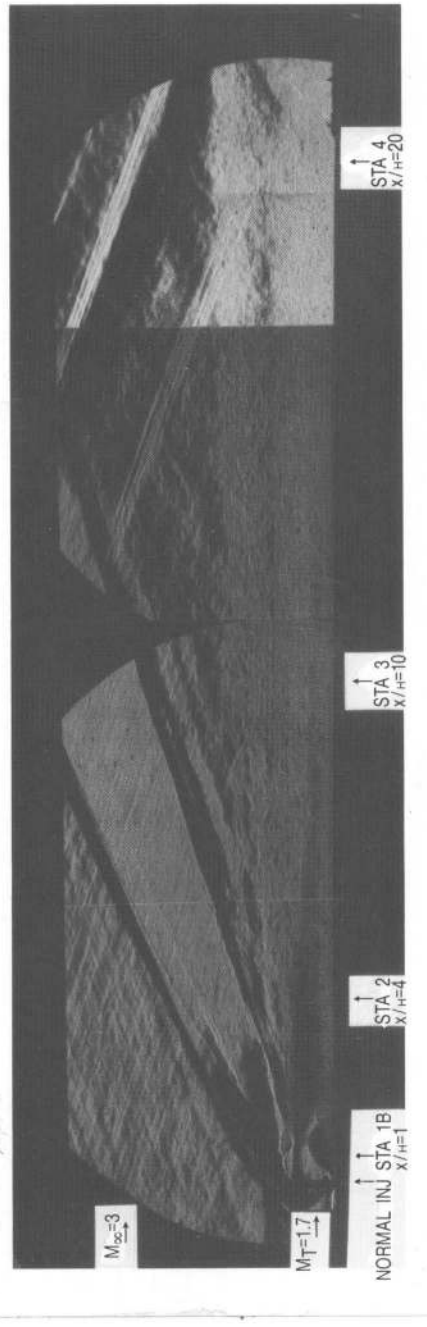

Figure 9. Schlieren photgraph of Case (B): $M_N = 1.0$, $p_{0_N} = 350$, $p_{0_T} = 10.7$

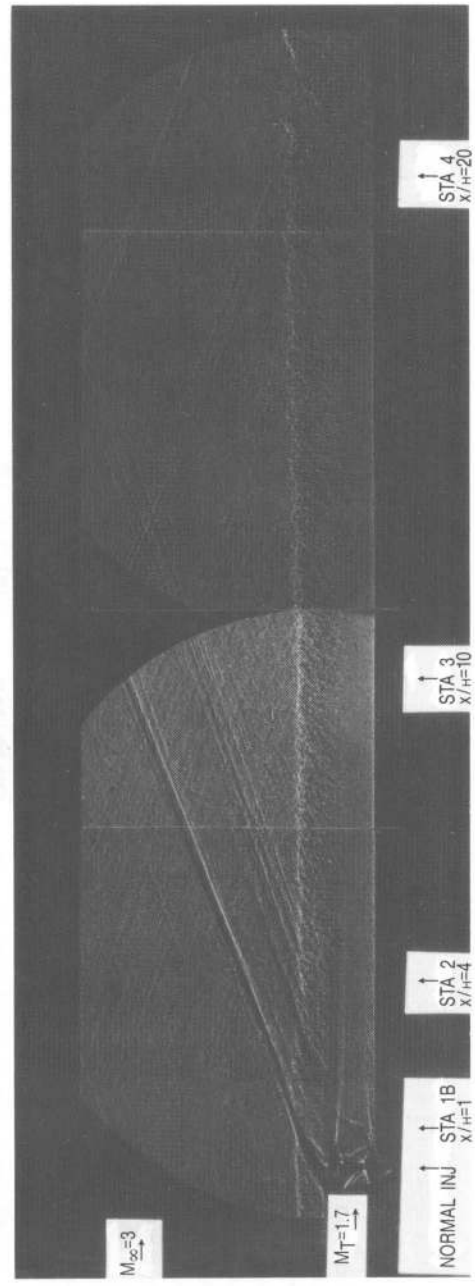

Figure 10. Nanoshadowgraph of Case (A): $M_N = 1.0$, no normal injection, $p_{0_T} = 10.7$

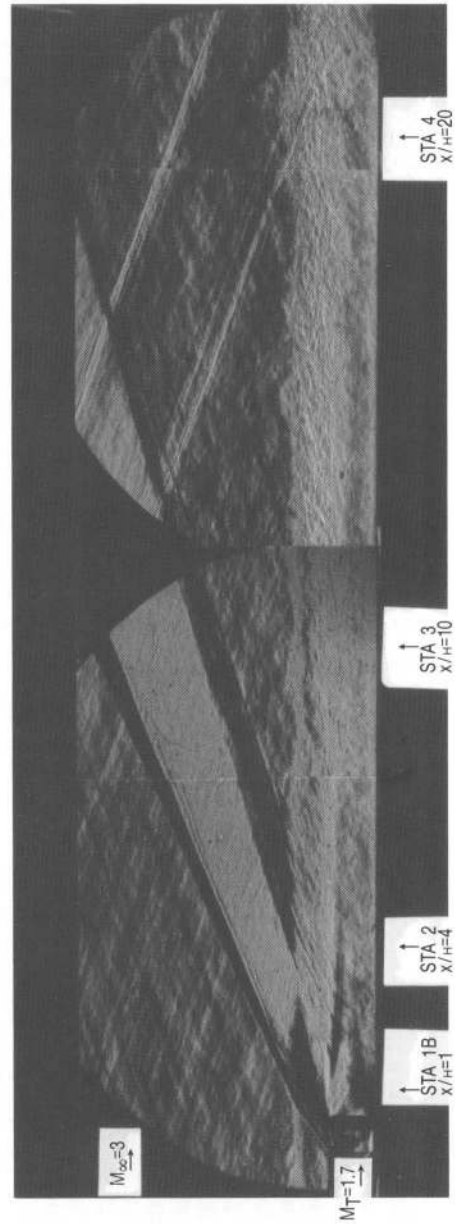

Figure 11. Sclieren photograph of Case (D): $M_N = 2.2$, no normal injection, $p_{0_T} = 10.7$

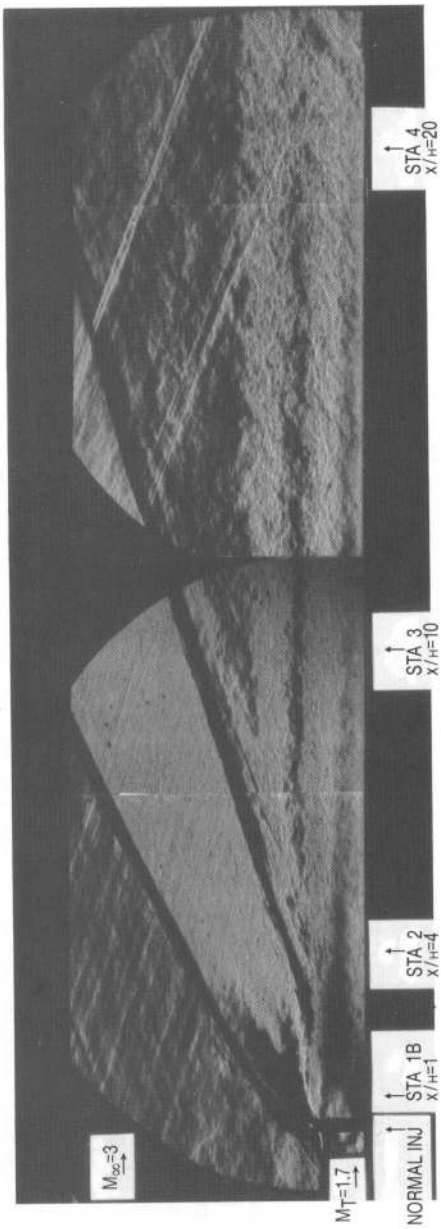

Figure 12. Schlieren photograph of Case (F): $M_N = 2.2$, $p_{0_N} = 500$, $p_{0_T} = 10.7$

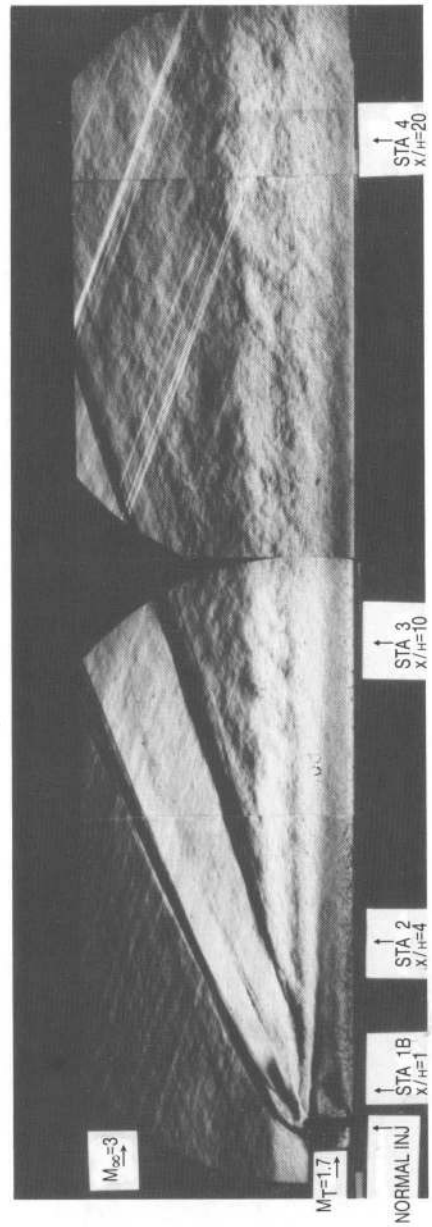

Figure 13. Schlieren photograph of Case (G): $M_N = 1.0$, $p_{0_N} = 350$, $p_{0_T} = 9.7$

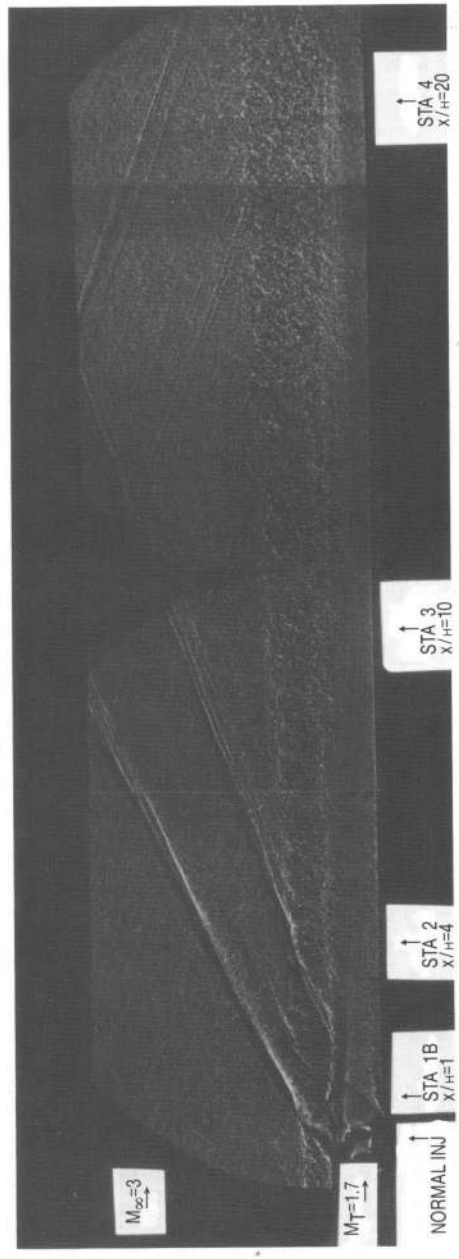

Figure 14. Nanoshadowgraph of Case (G): $M_N = 1.0$, $p_{0_N} = 350$, $p_{0_T} = 9.7$

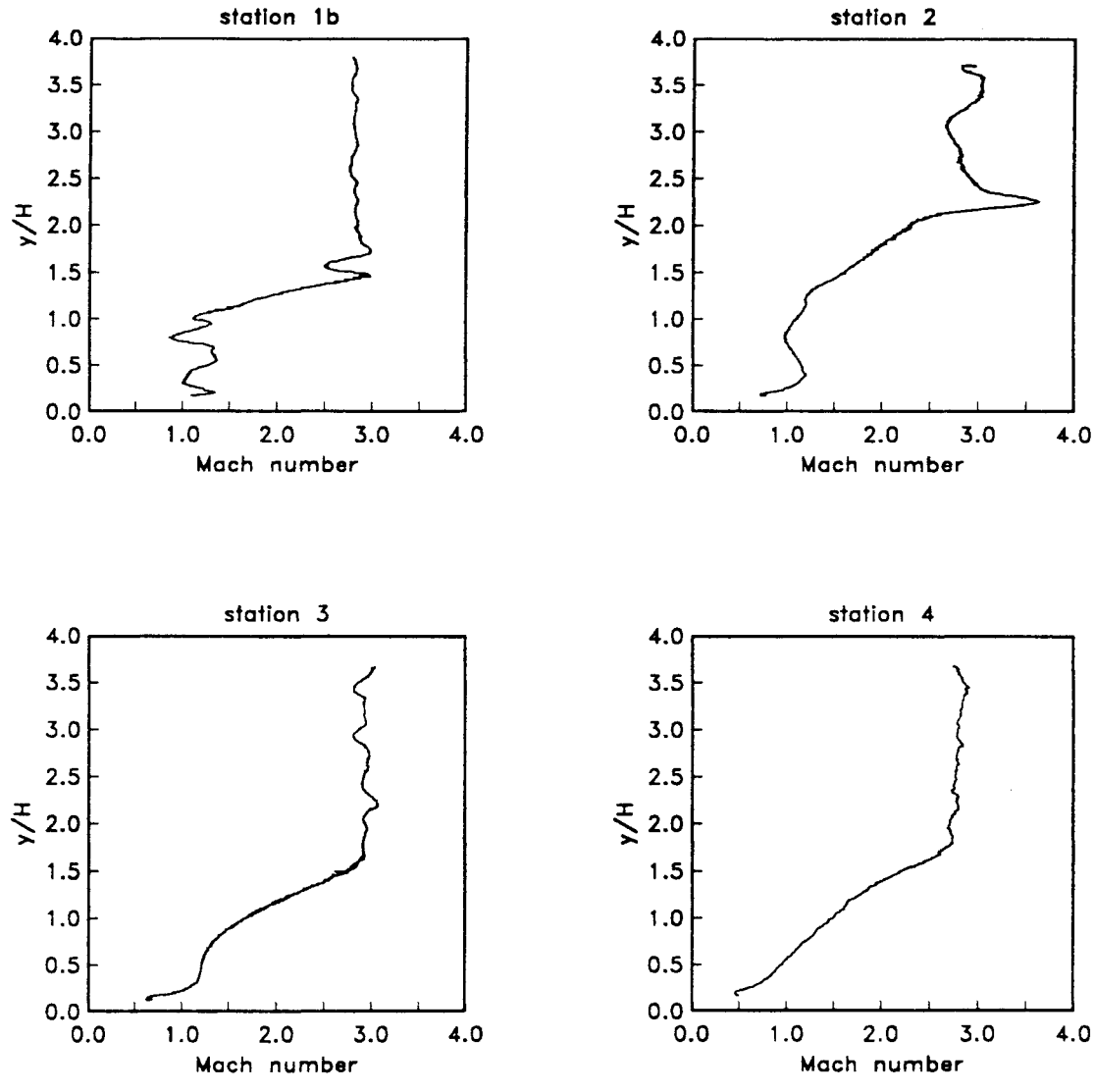

Figure 15. Mach number profiles, left side, Case (A)

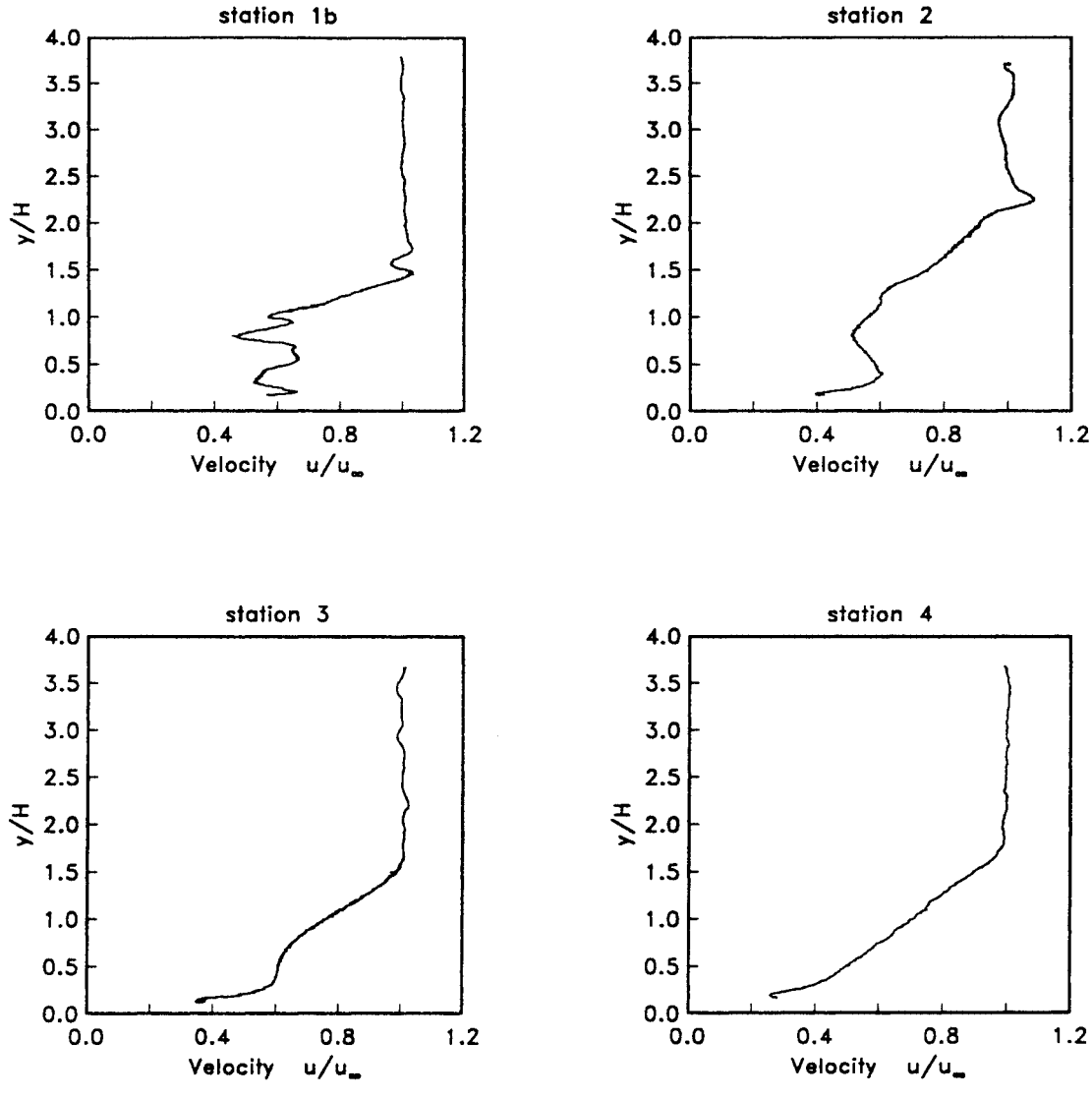

Figure 16. Velocity profiles, left side, Case (A)

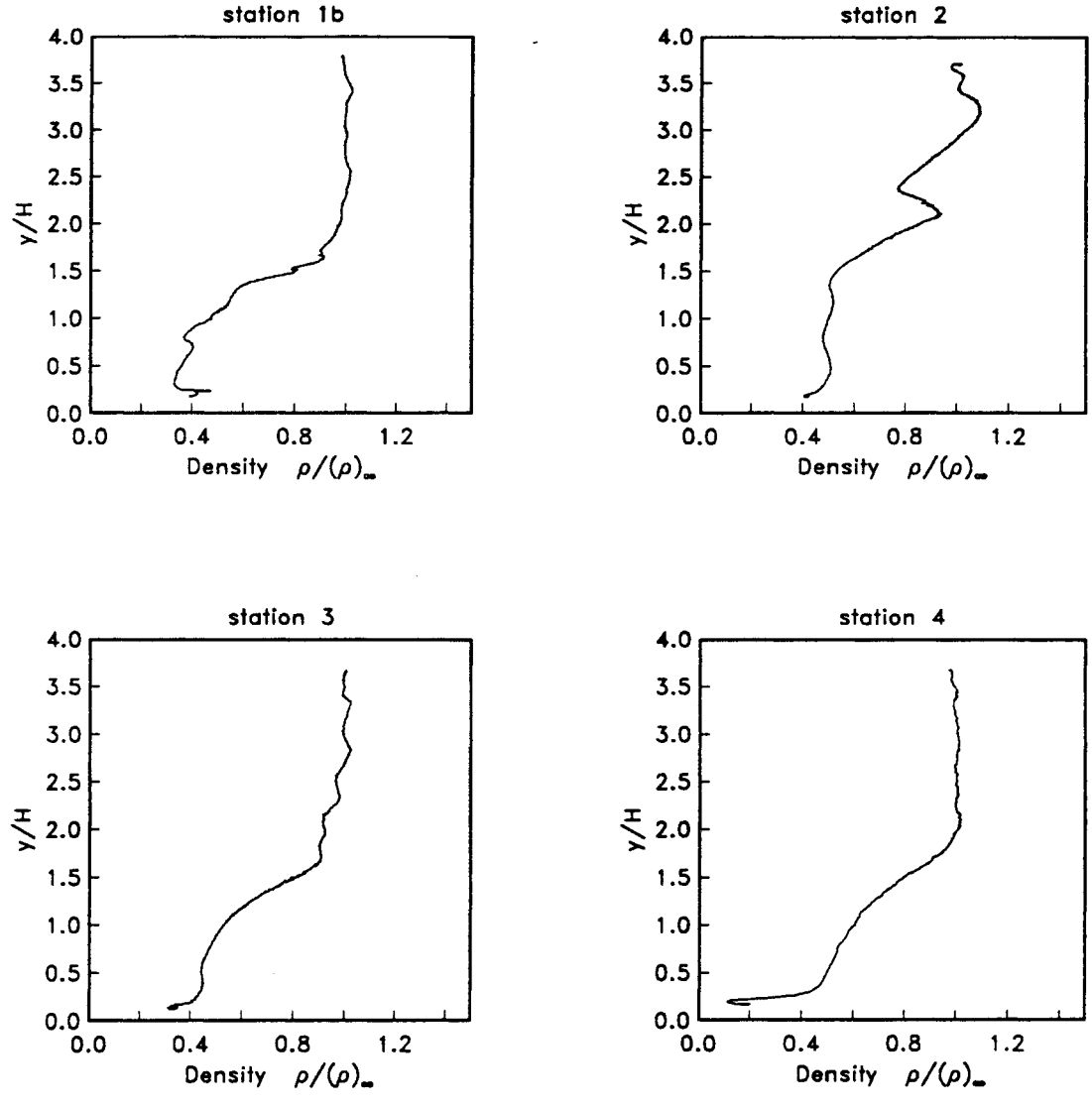

Figure 17. Density profiles, left side, Case (A)

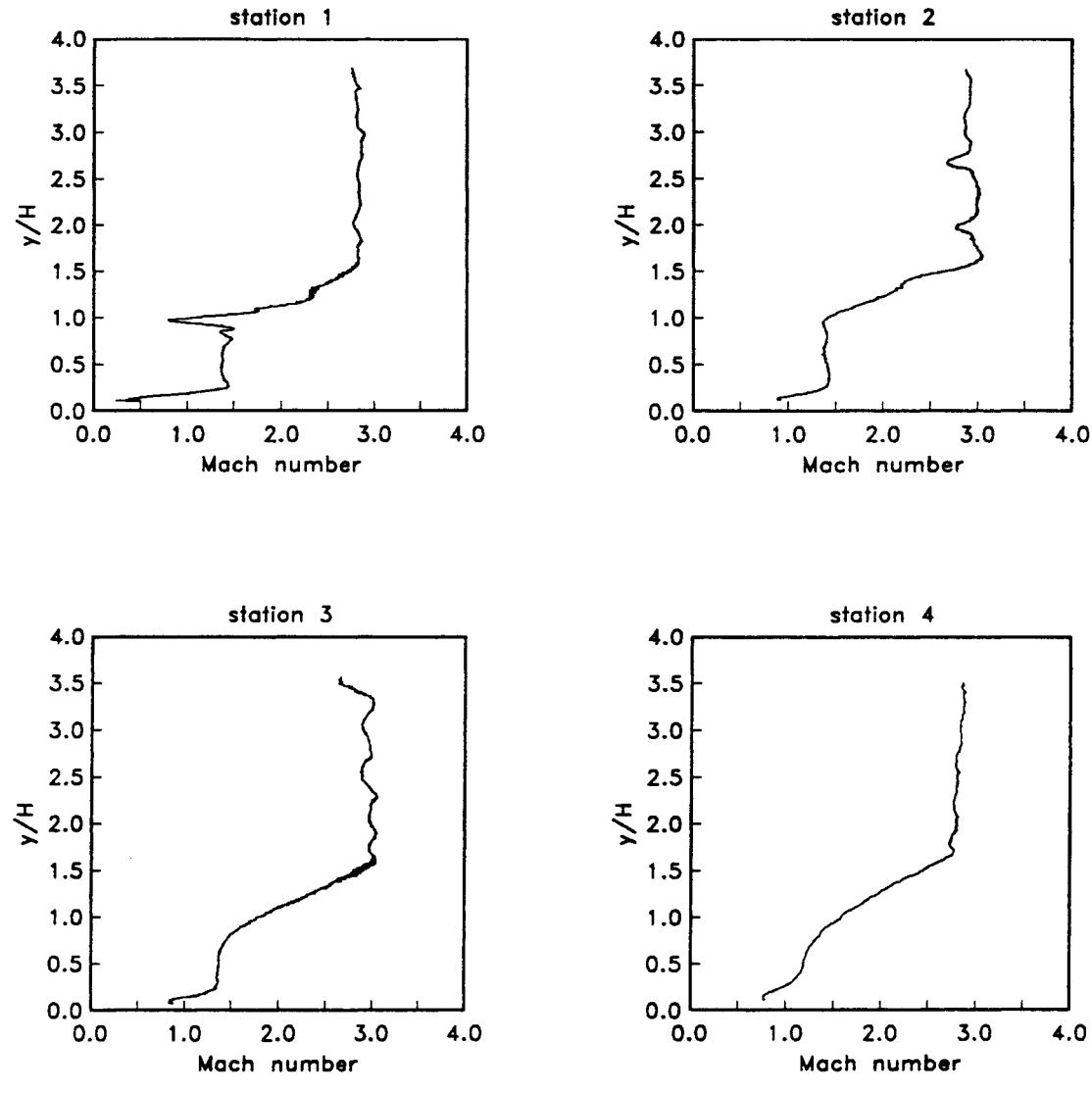

Figure 18. Mach number profiles, right side, Case (A)

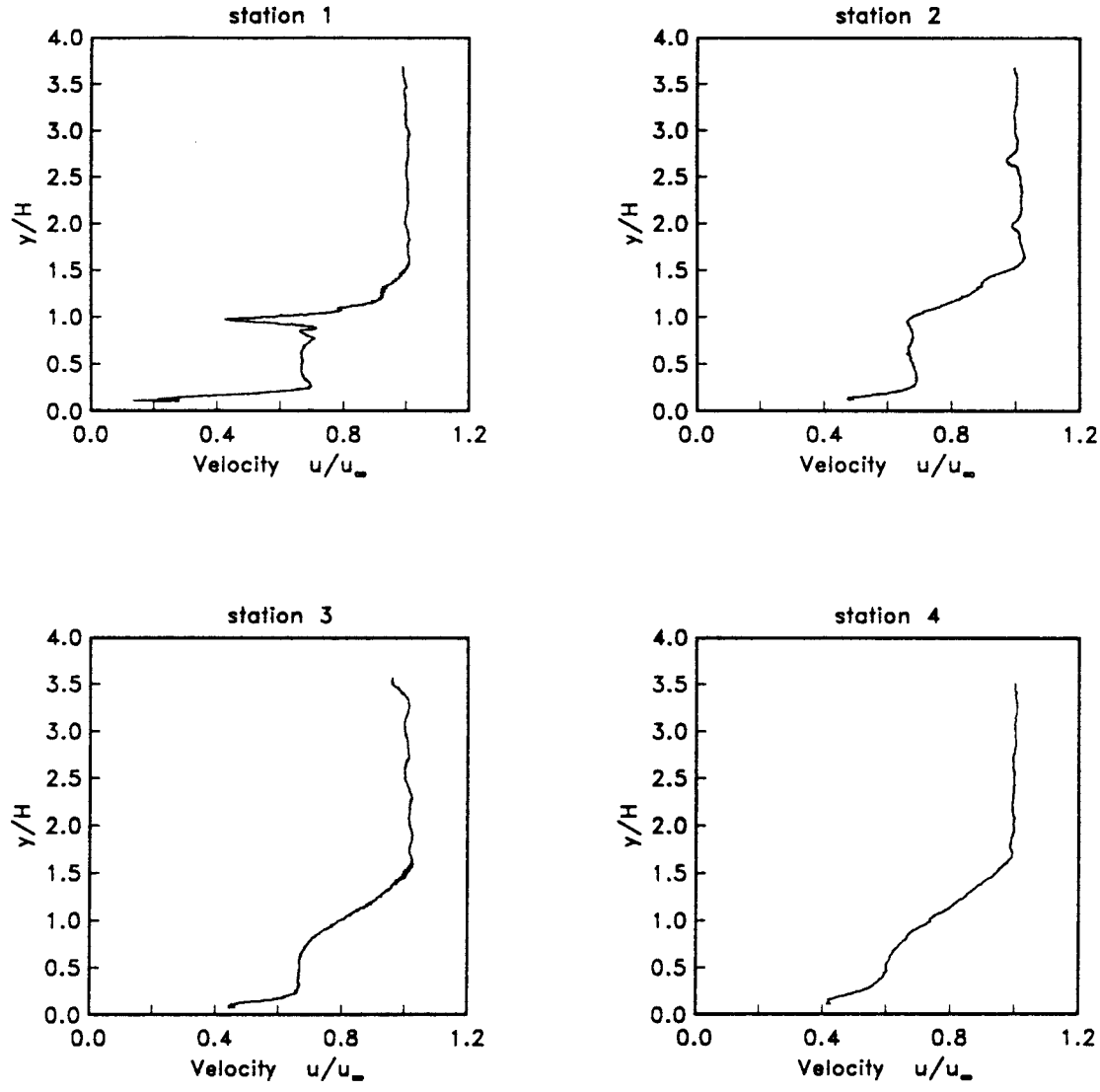

Figure 19. Velocity profiles, right side, Case (A)

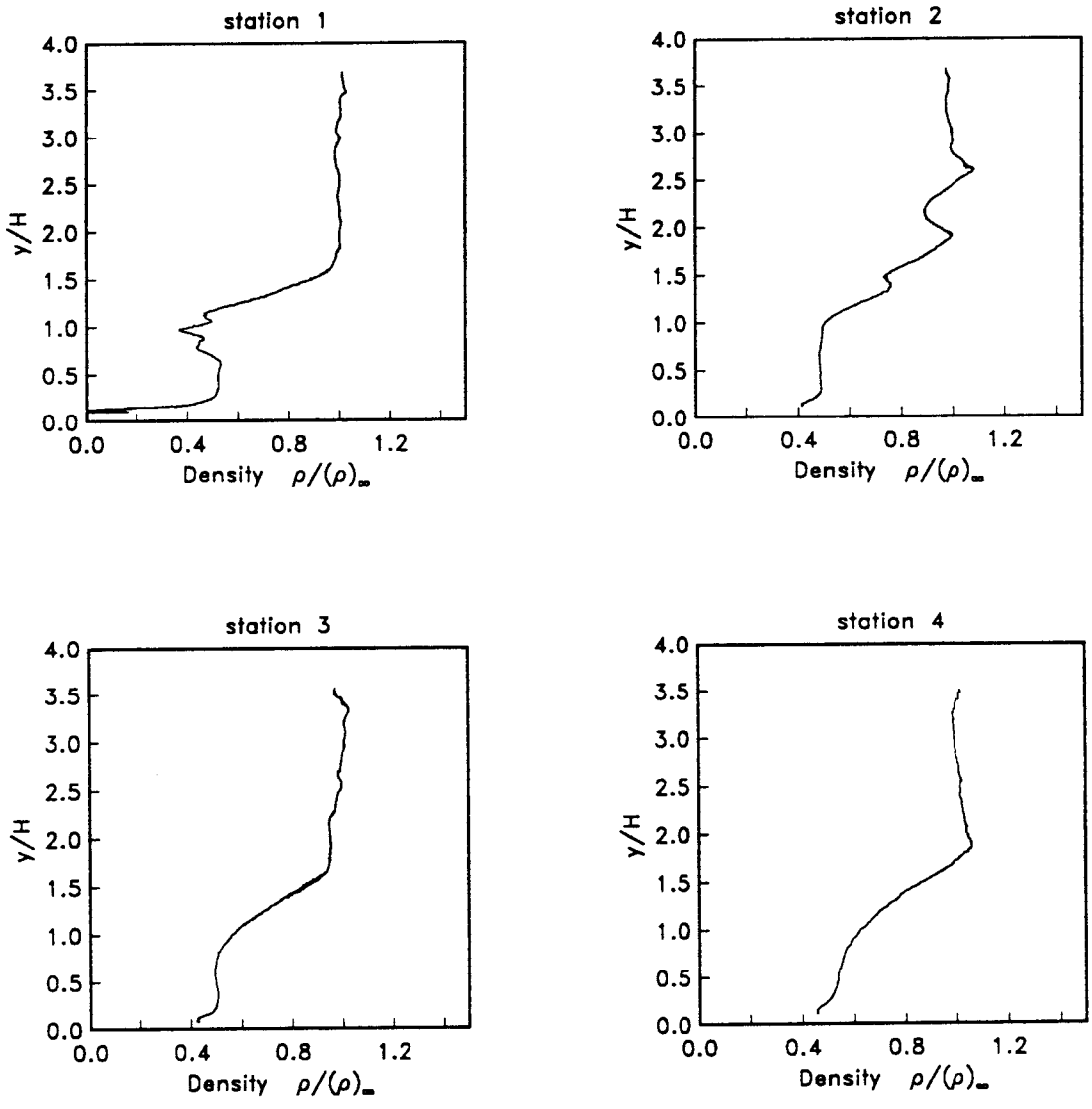

Figure 20. Density profiles, right side, Case (A)

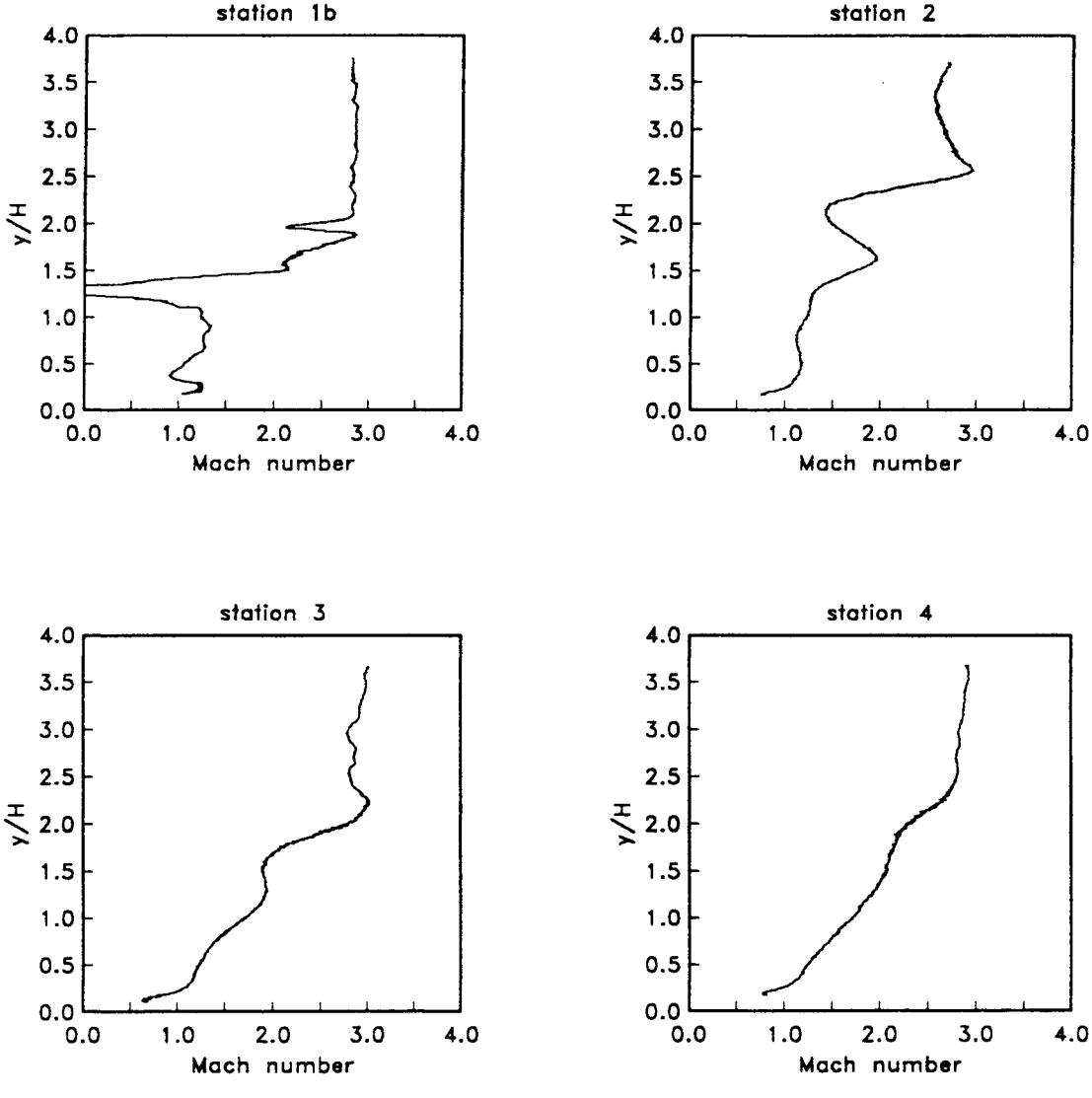

Figure 21. Mach number profiles, left side, Case (B)

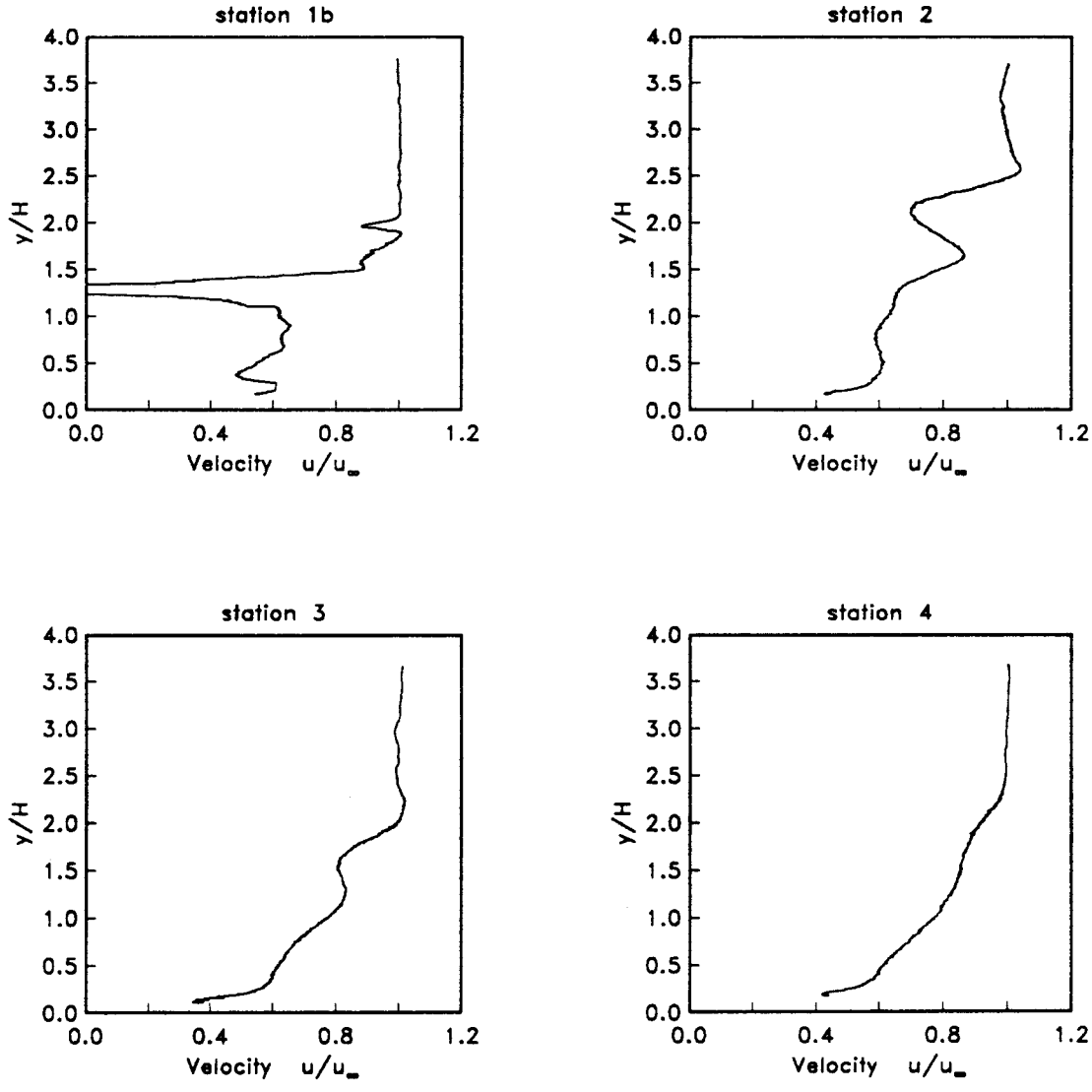

Figure 22. Velocity profiles, left side, Case (B)

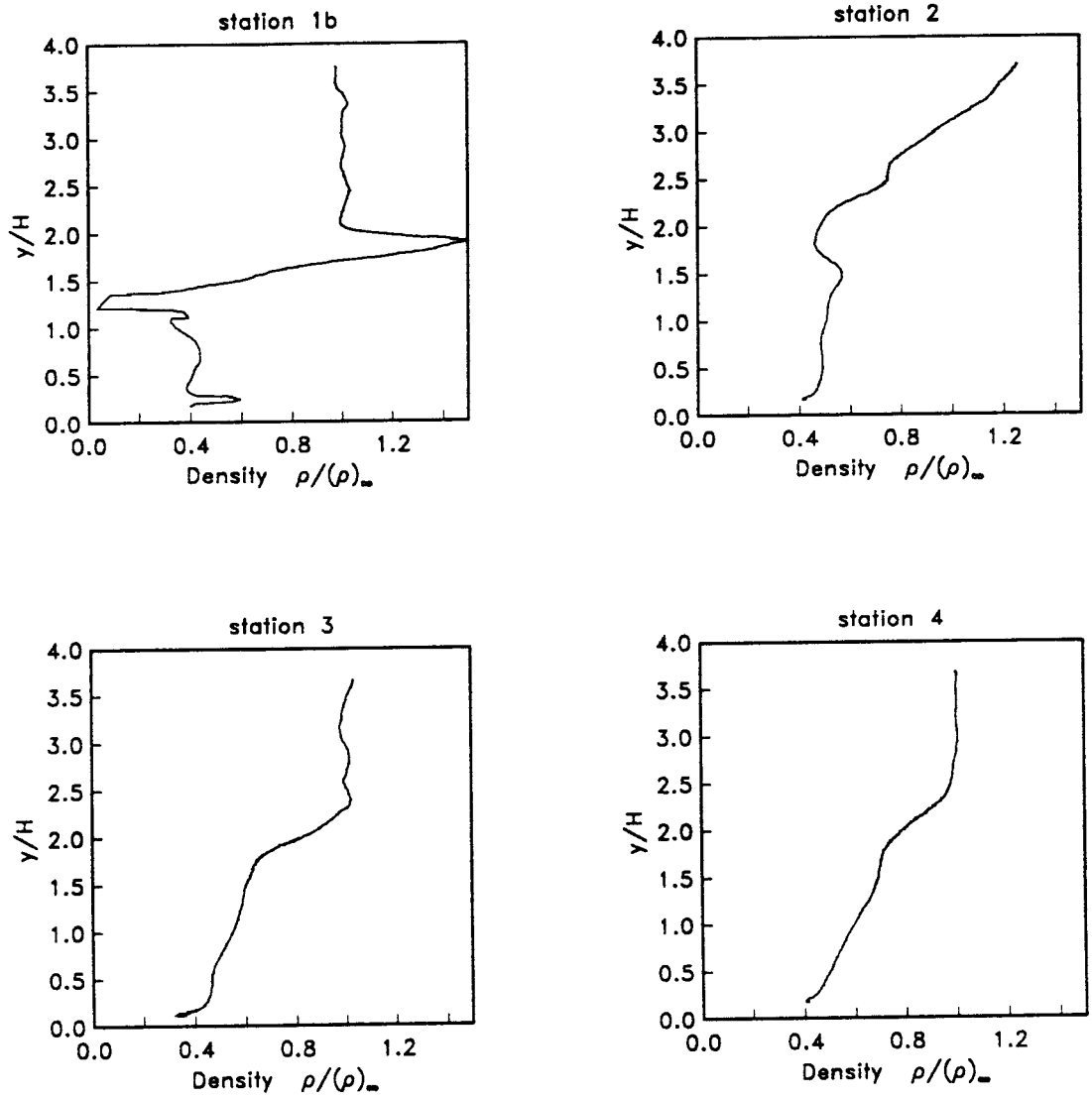

Figure 23. Density profiles, left side, Case (B)

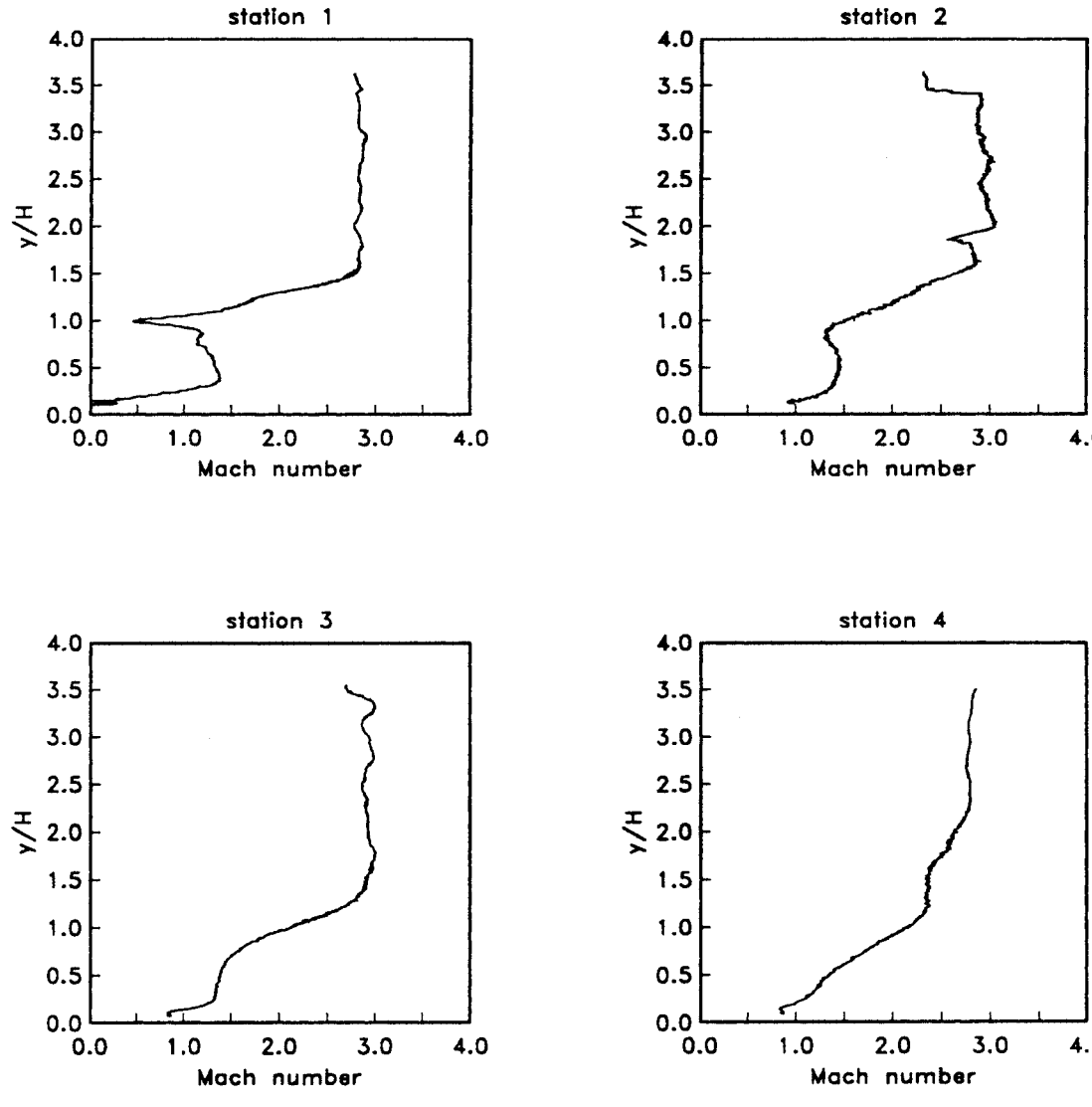

Figure 24. Mach number profiles, right side, Case (B)

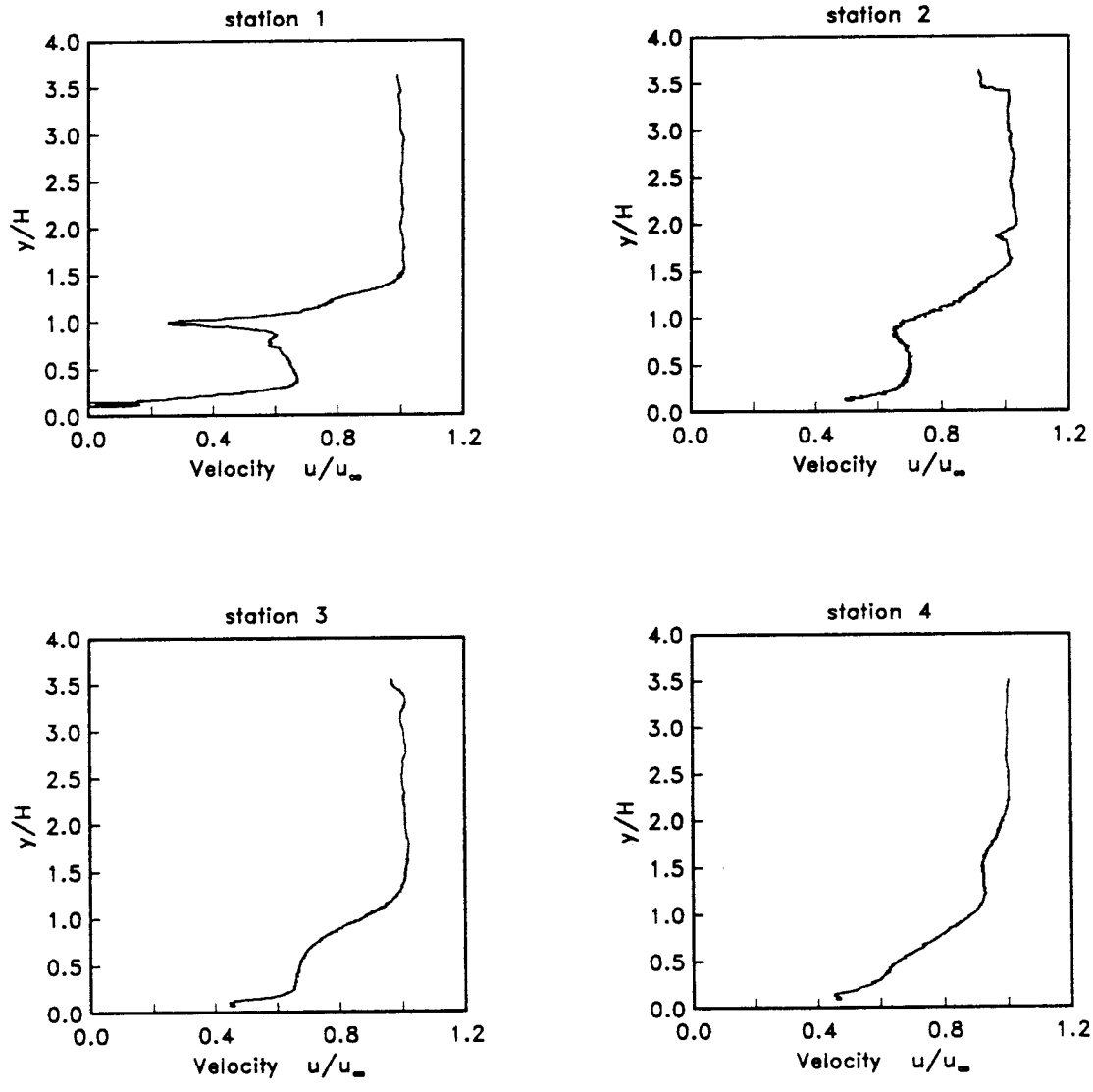

Figure 25. Velocity profiles, right side, Case (B)

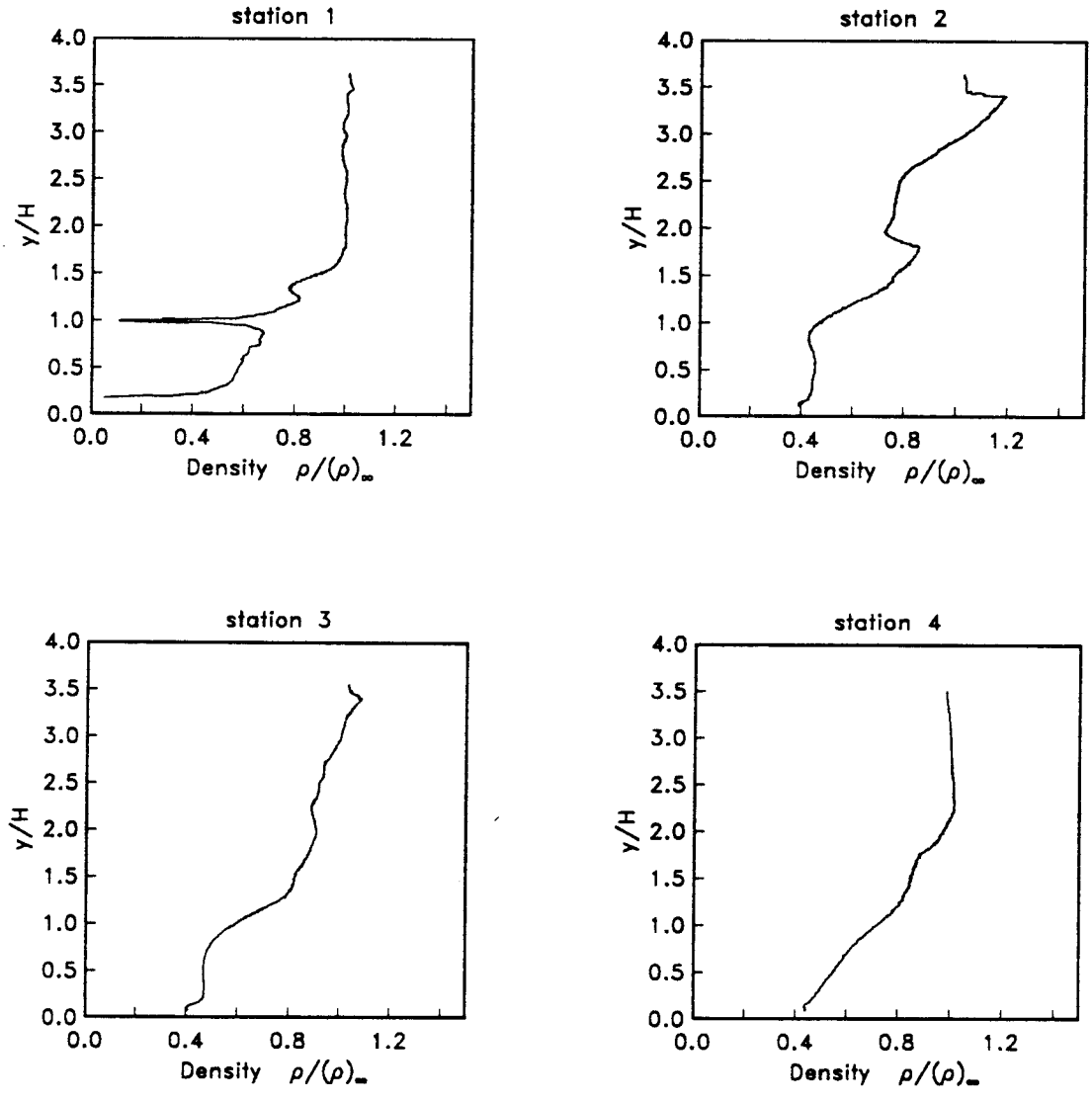

Figure 26. Density profiles, right side, Case (B)

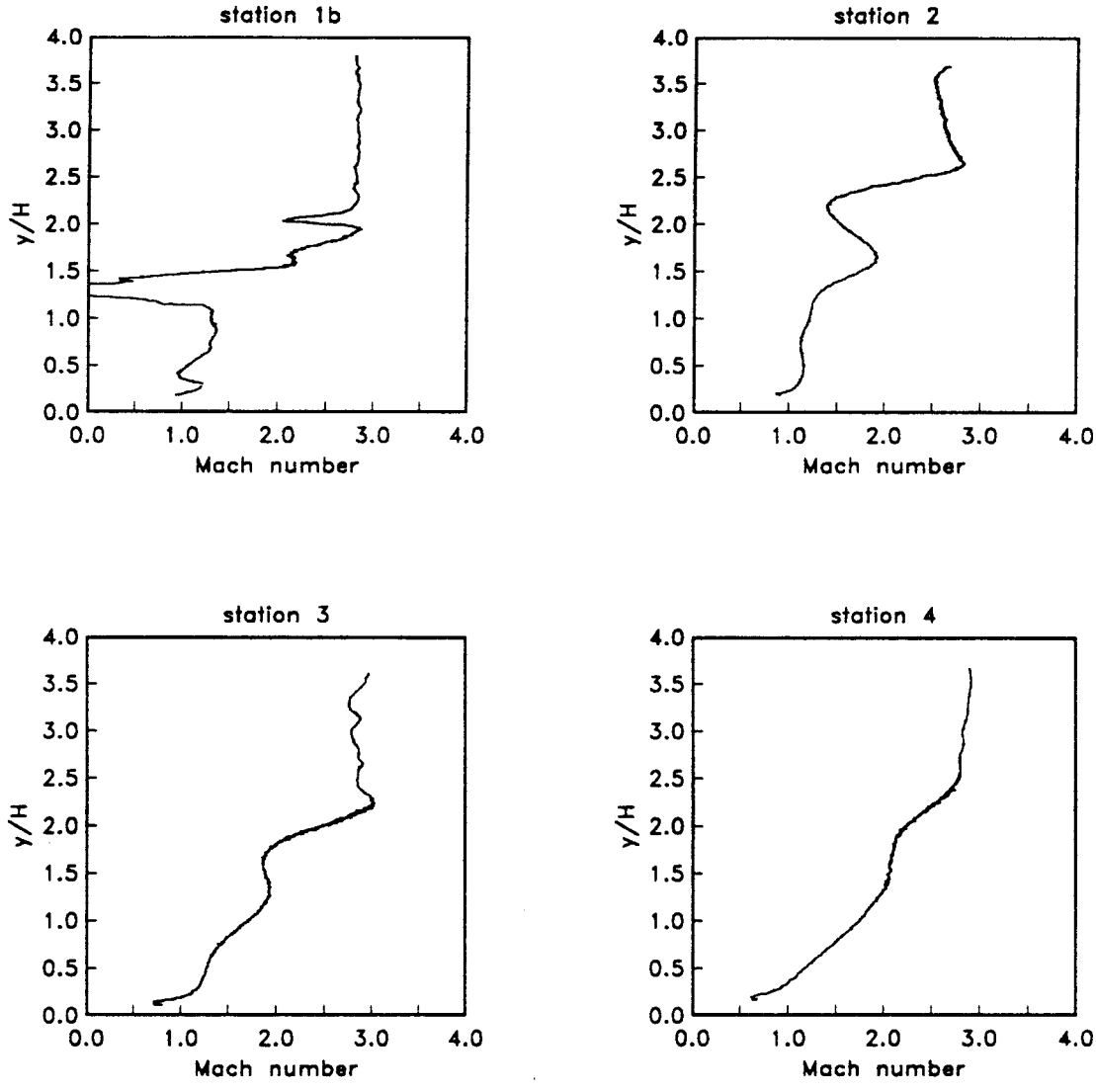

Figure 27. Mach number profiles, left side, Case (C)

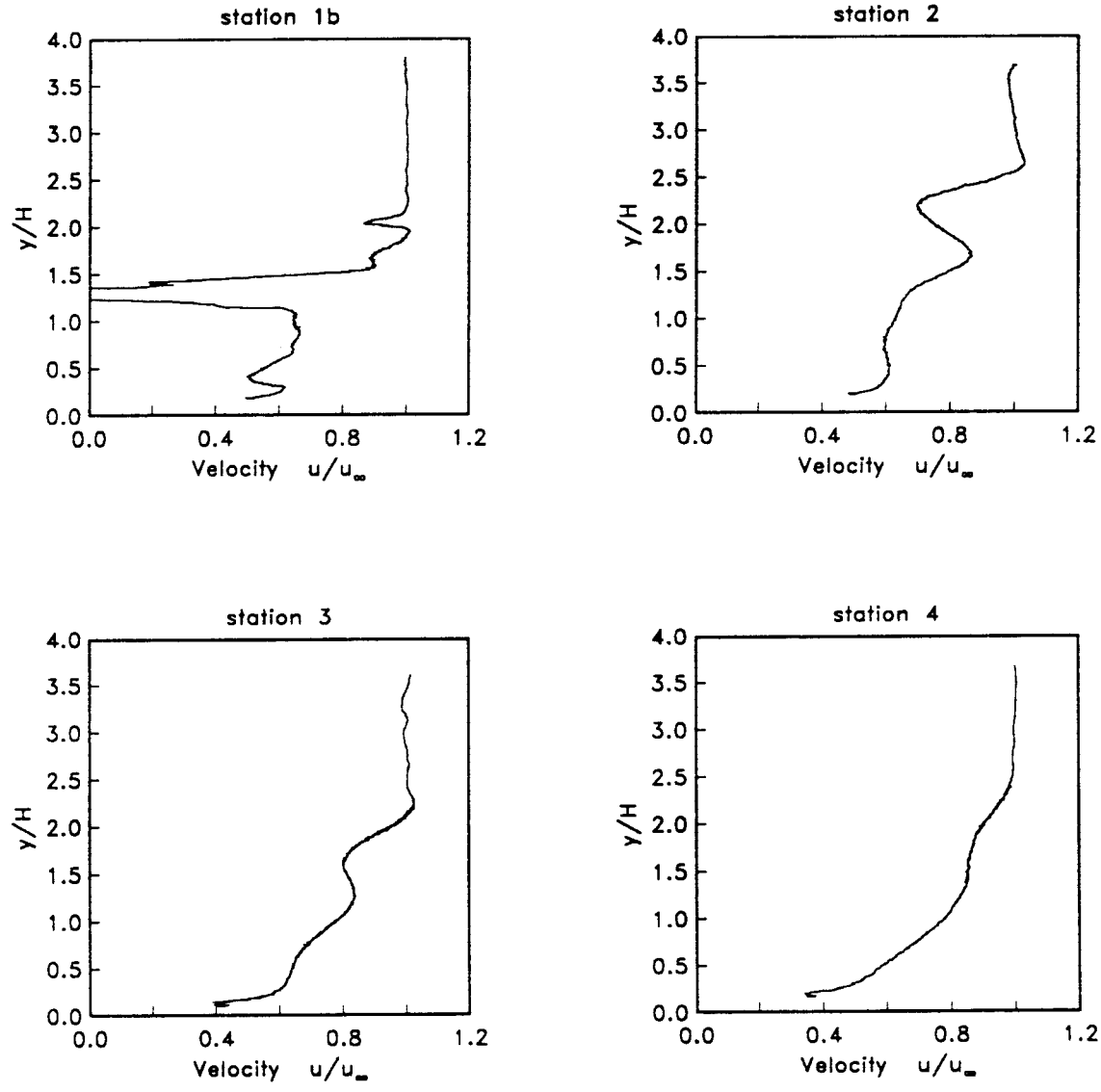

Figure 28. Velocity profiles, left side, Case (C)

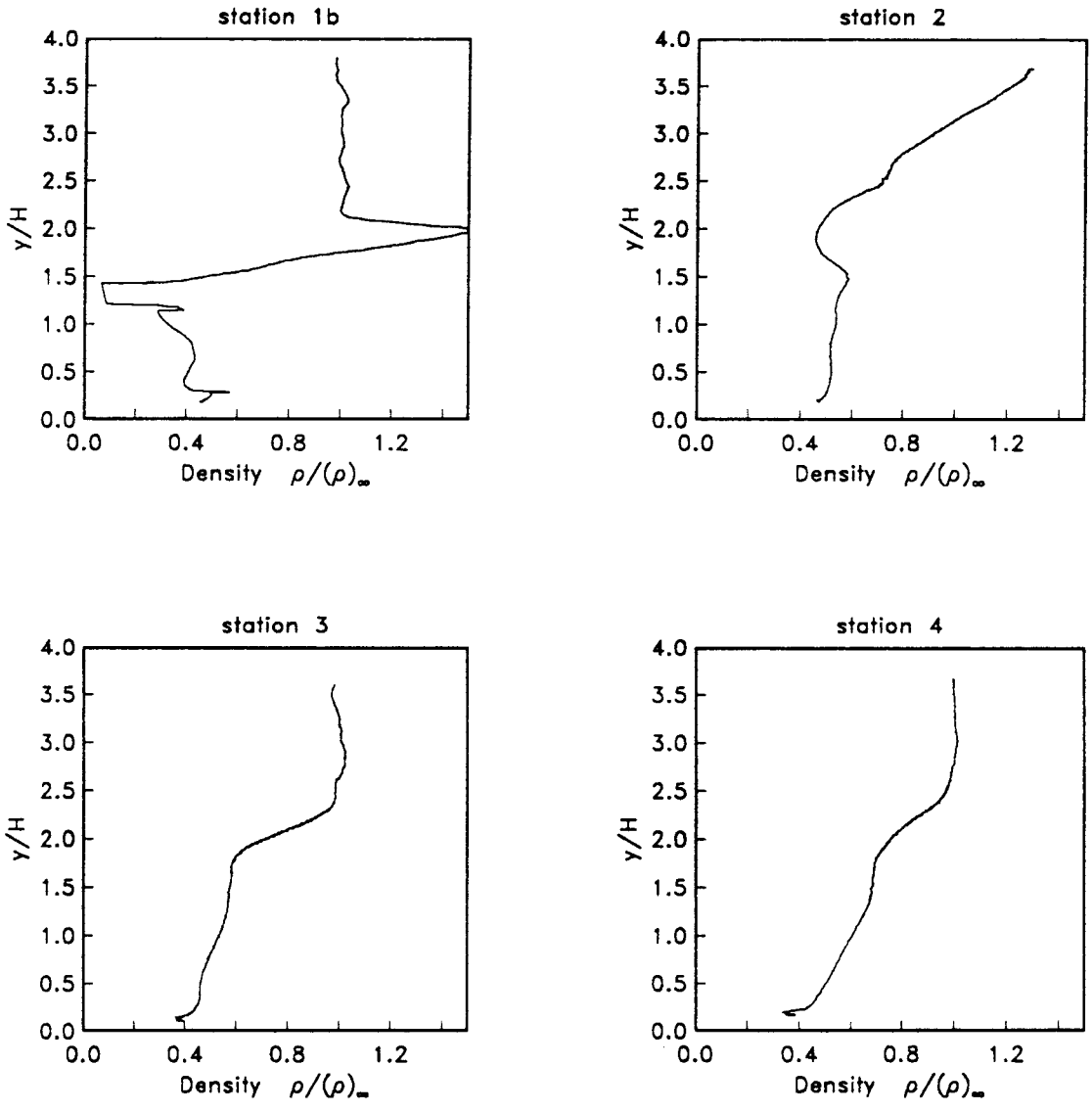

Figure 29. Density profiles, left side, Case (C)

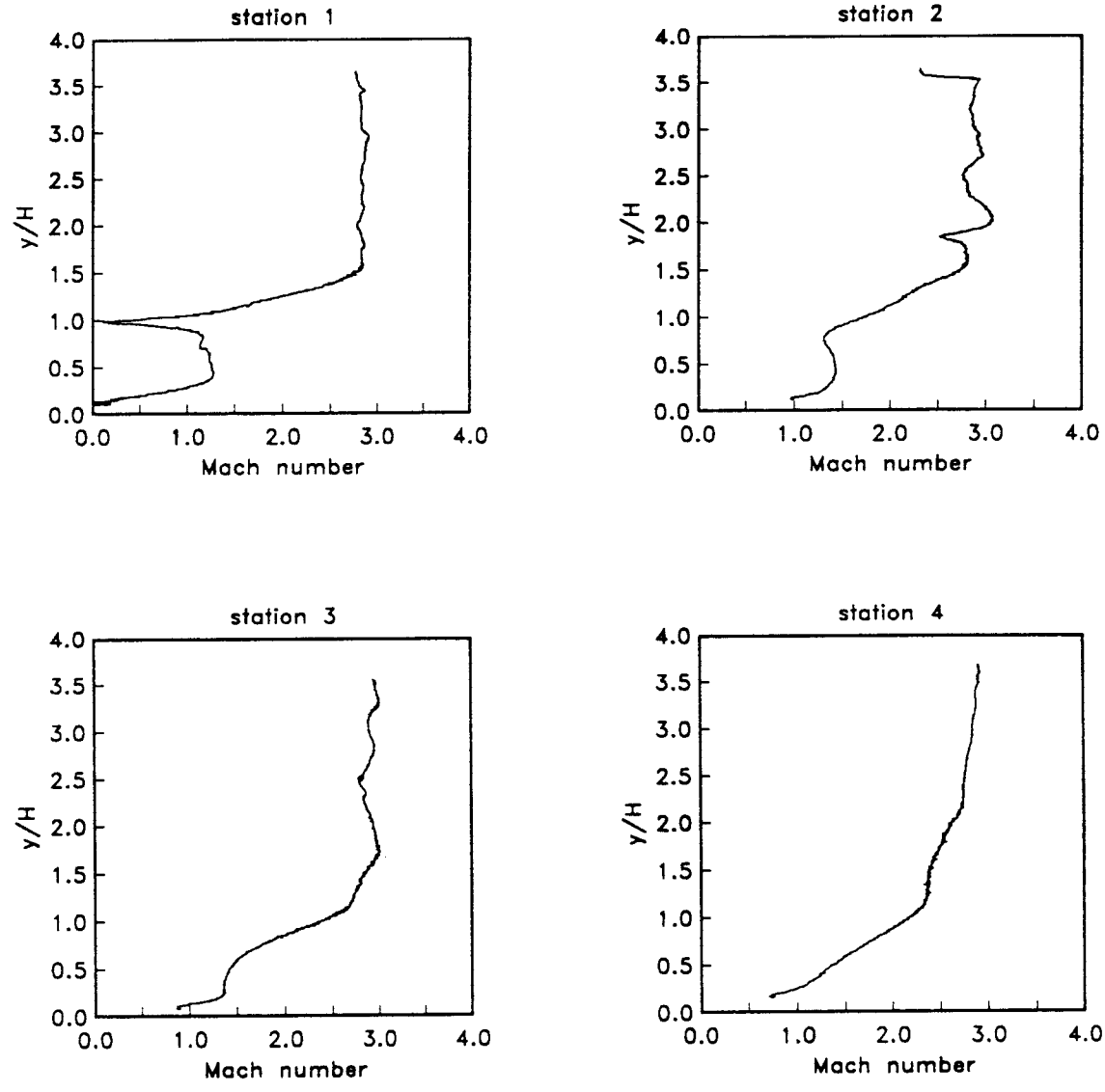

Figure 30. Mach number profiles, right side, Case (C)

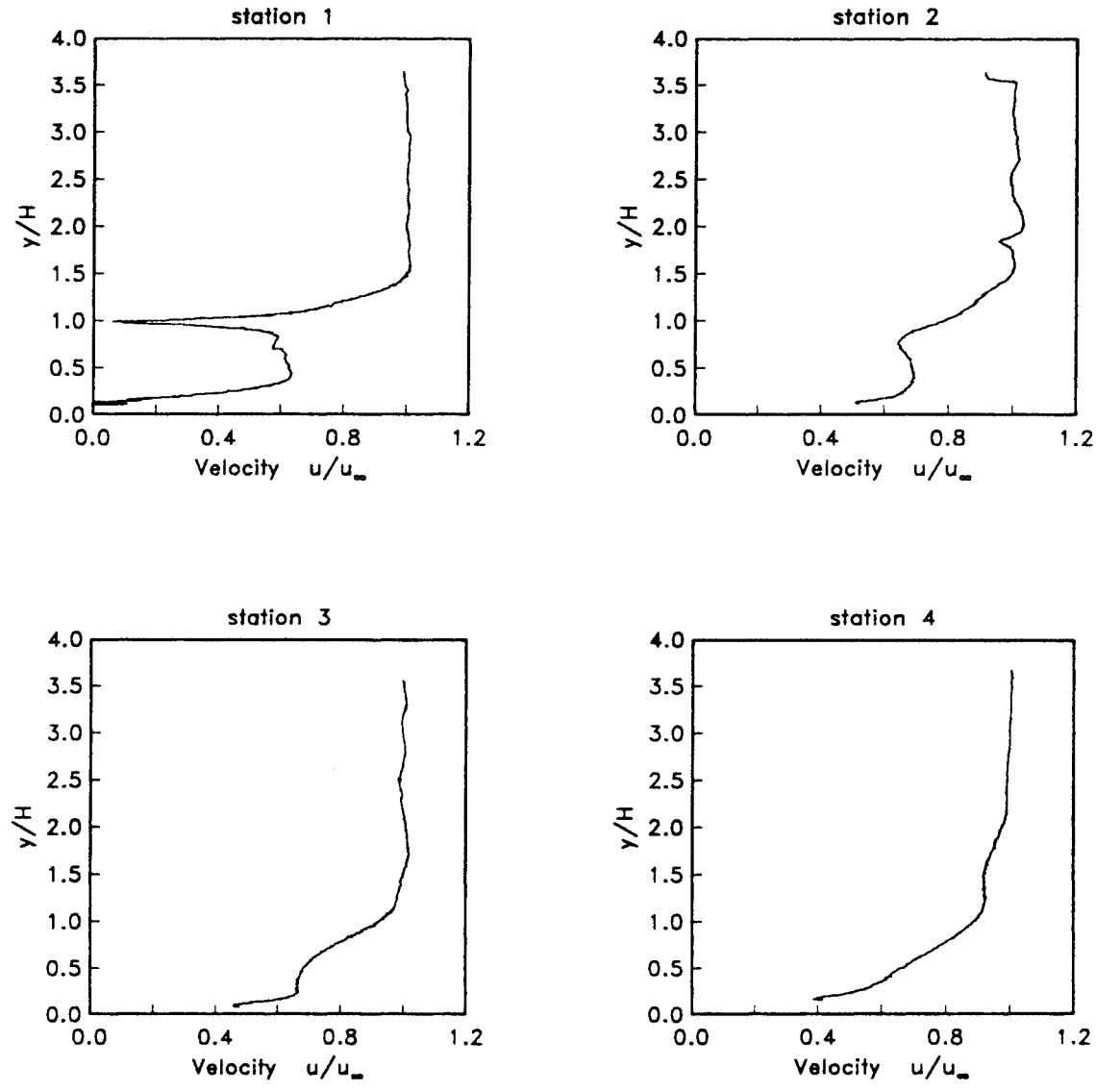

Figure 31. Velocity profiles, right side, Case (C)

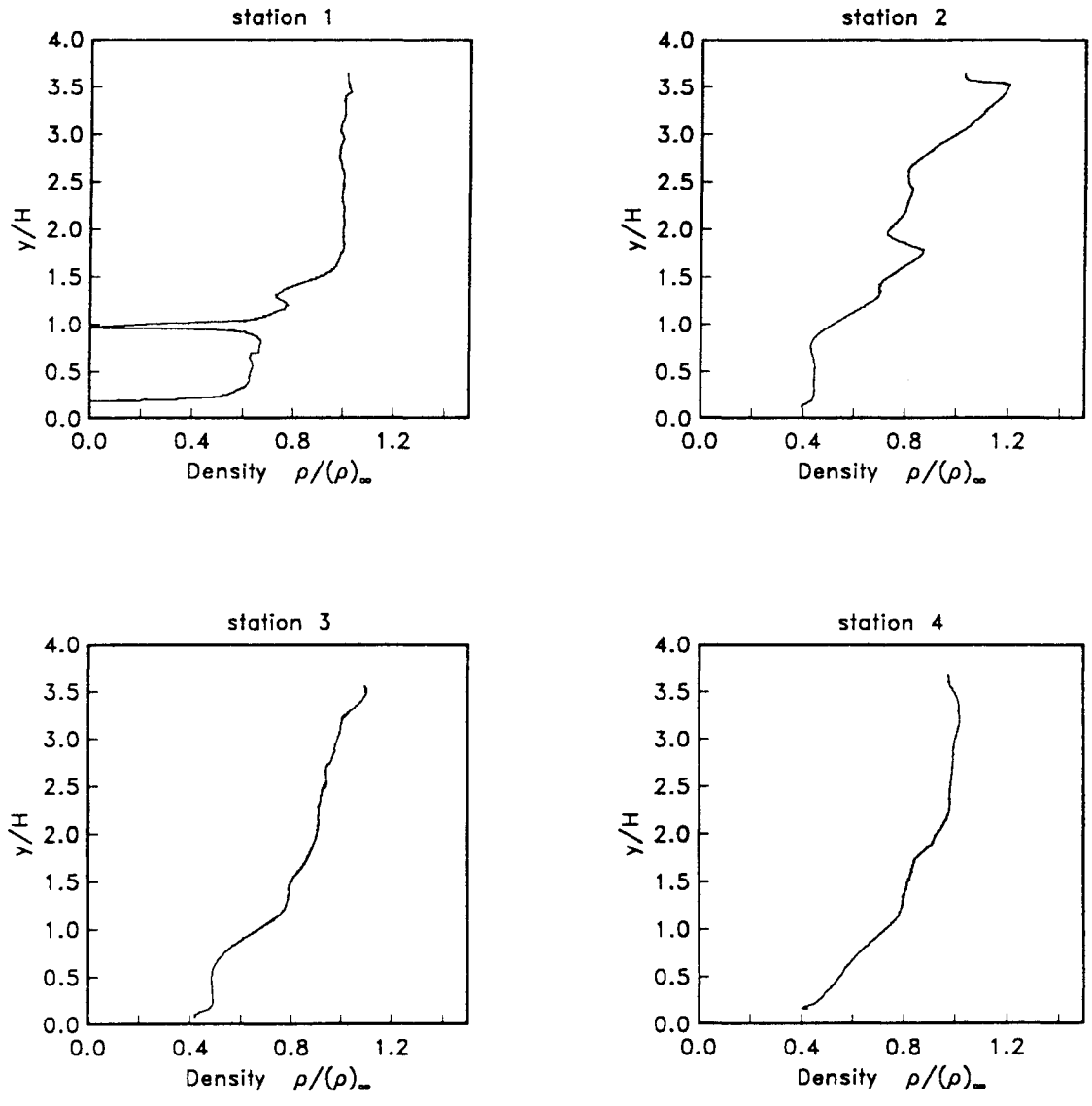

Figure 32. Density profiles, right side, Case (C)

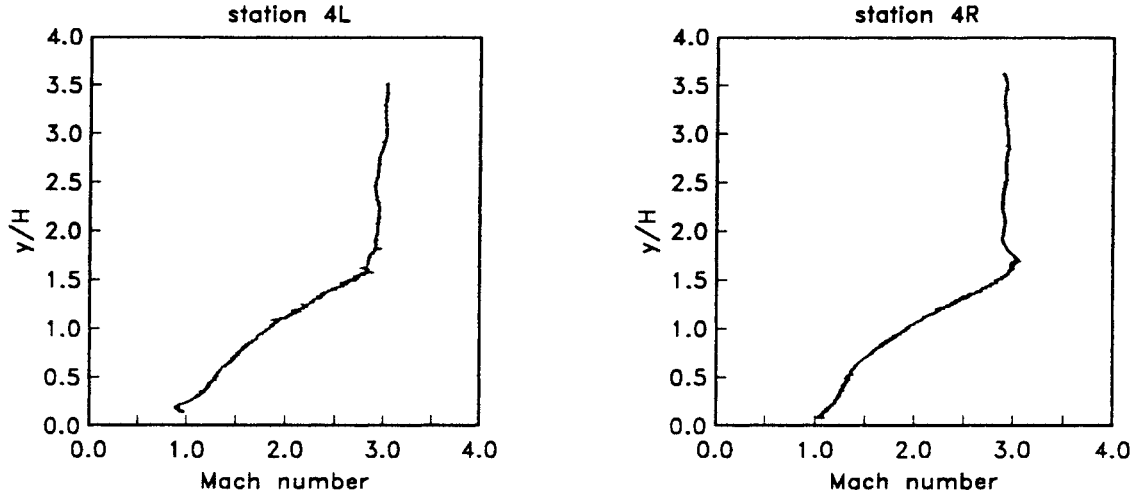

Figure 33. Mach number profiles, Stations 4L,4R, Case (D)

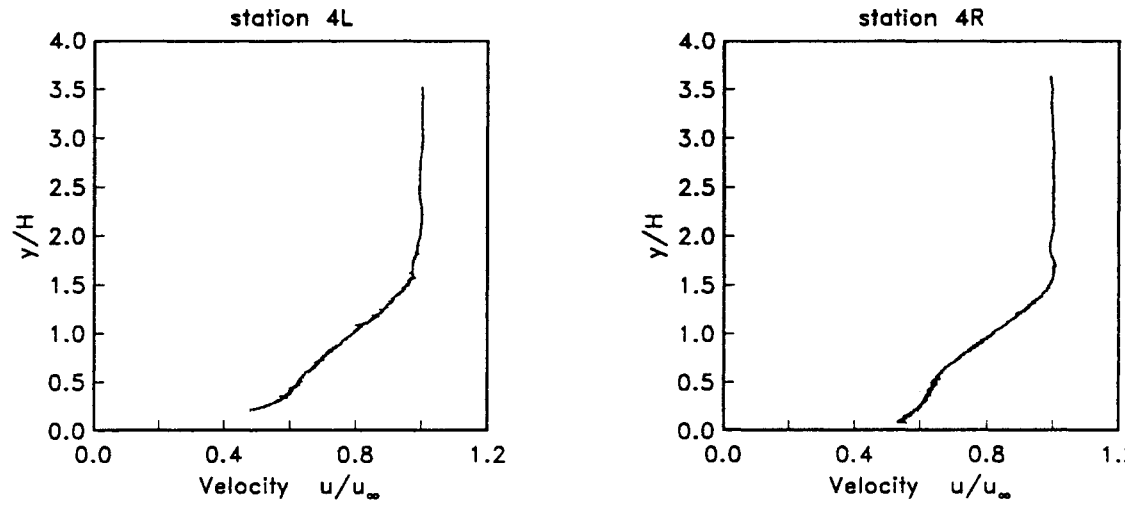

Figure 34. Velocity profiles, Stations 4L,4R, Case (D)

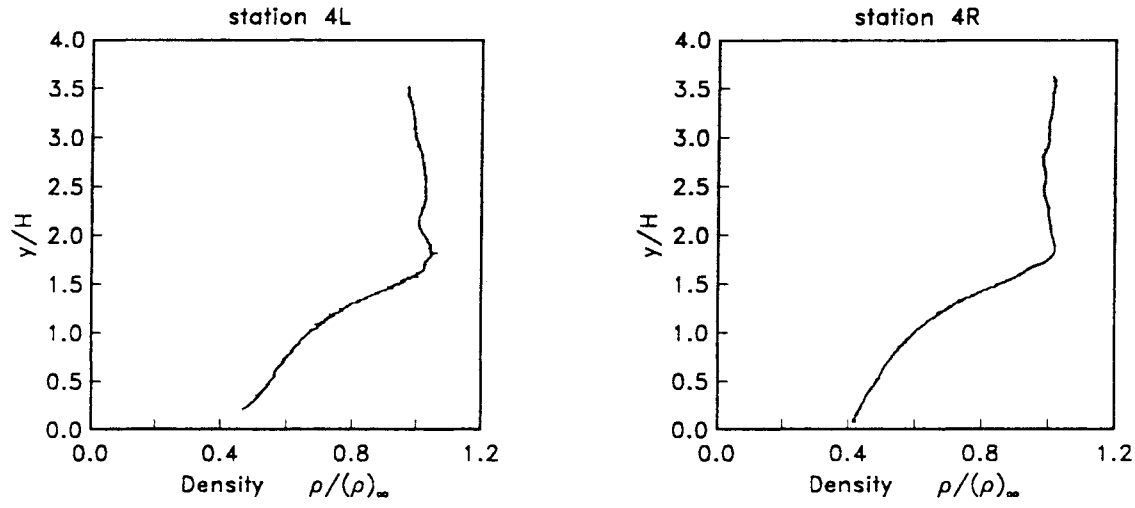

Figure 35. Density profiles, Stations 4L,4R, Case (D)

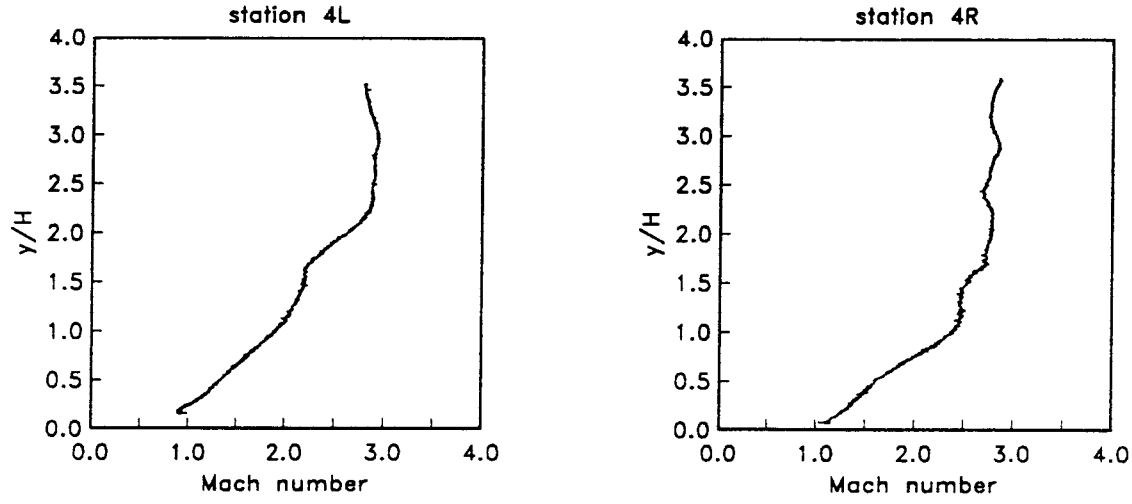

Figure 36. Mach number profiles, Stations 4L,4R, Case (E)

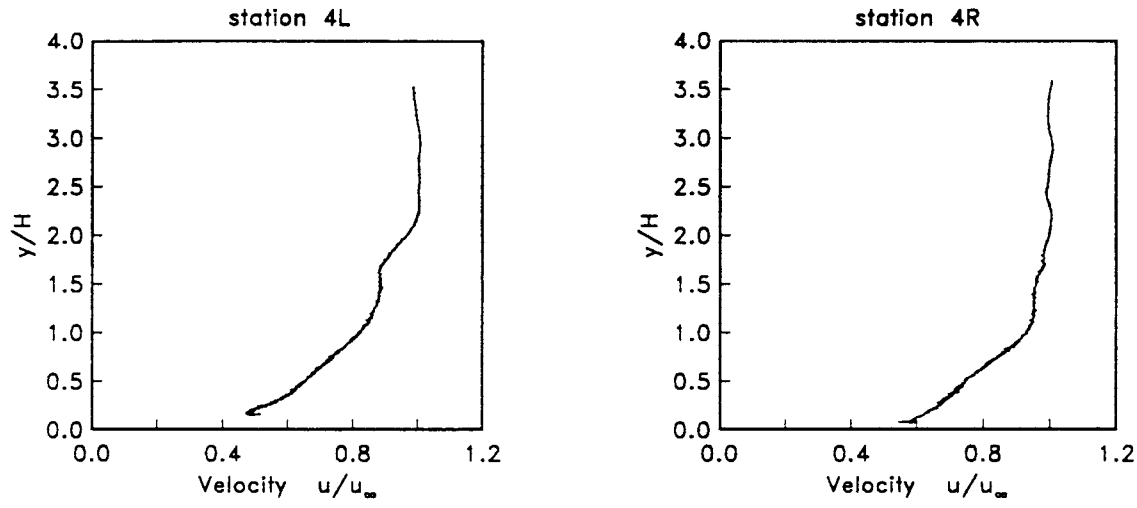

Figure 37. Velocity profiles, Stations 4L,4R, Case (E)

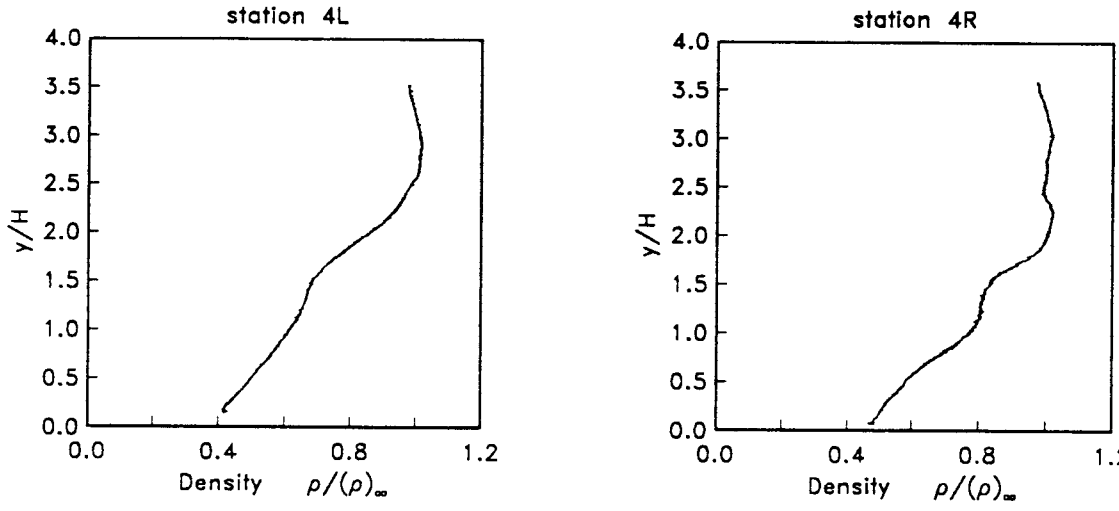

Figure 38. Density profiles, Stations 4L,4R, Case (E)

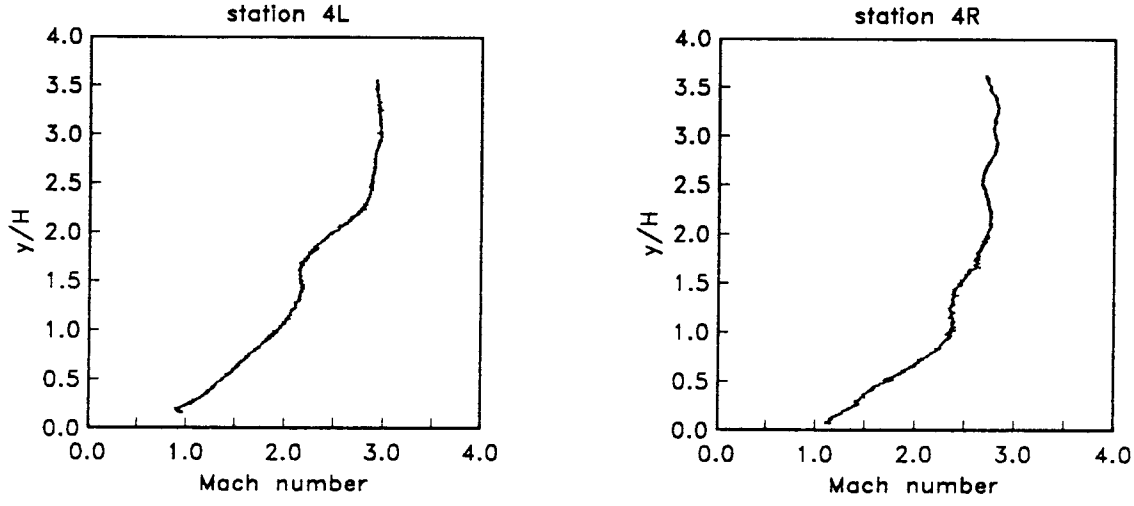

Figure 39. Mach number profiles, Stations 4L,4R, Case (F)

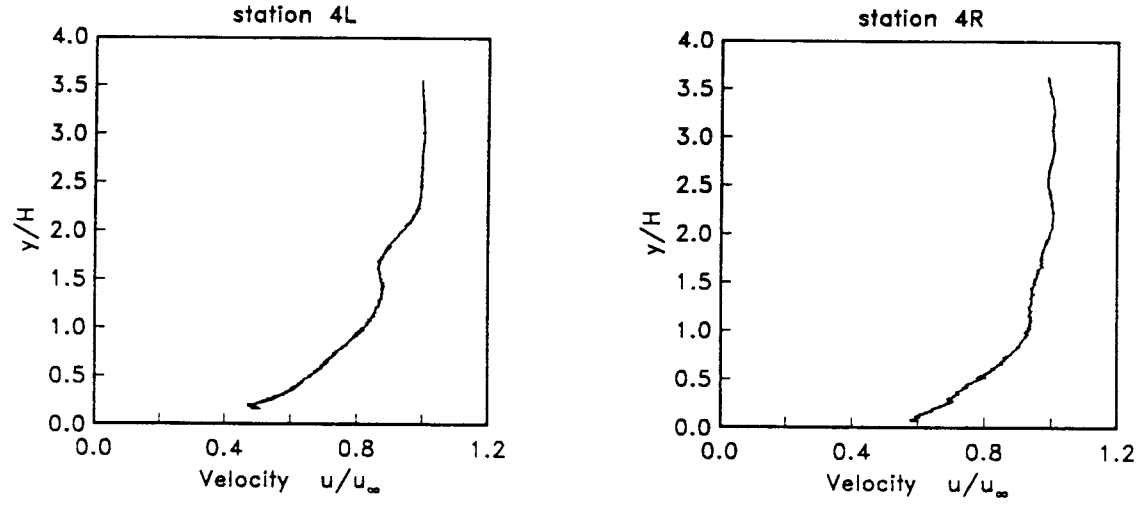

Figure 40. Velocity profiles, Stations 4L,4R, Case (F)

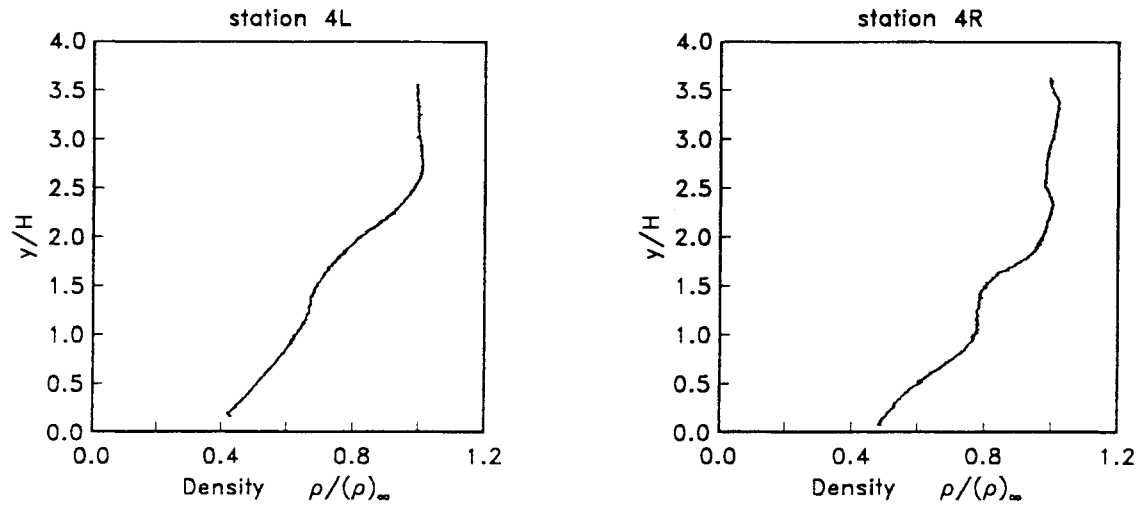

Figure 41. Density profiles, Stations 4L,4R, Case (F)

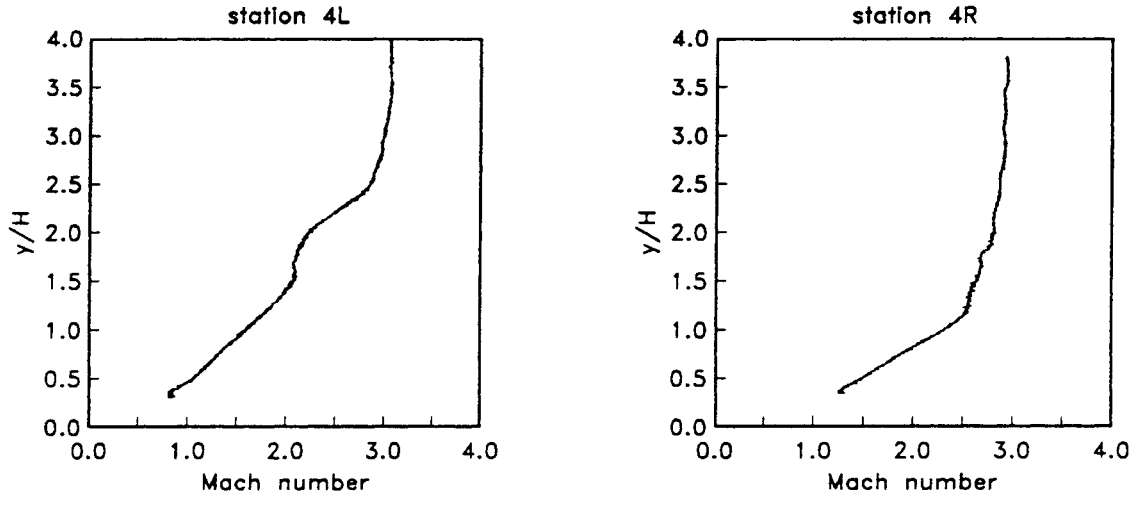

Figure 42. Mach number profiles, Stations 4L,4R, Case (G)

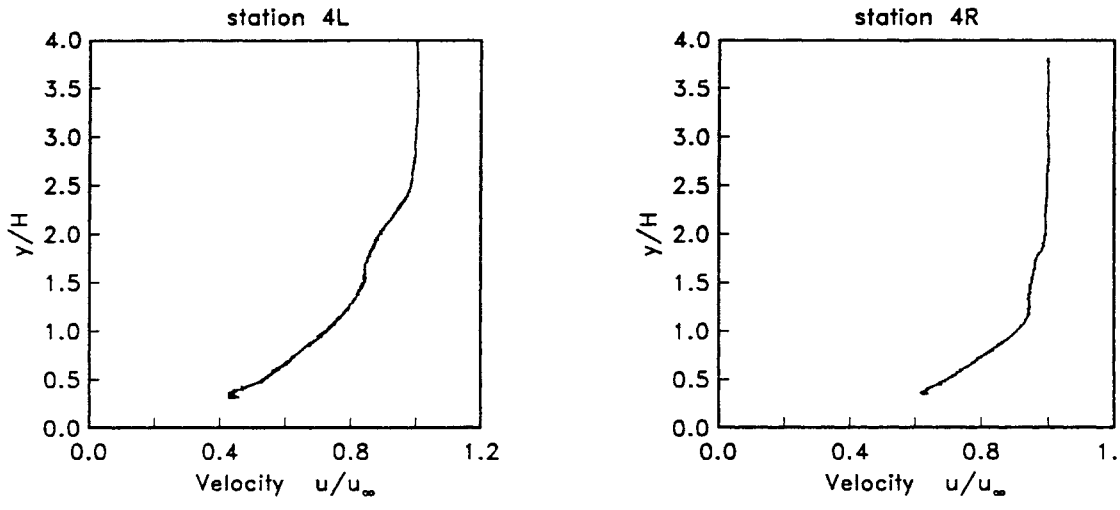

Figure 43. Velocity profiles, Stations 4L,4R, Case (G)

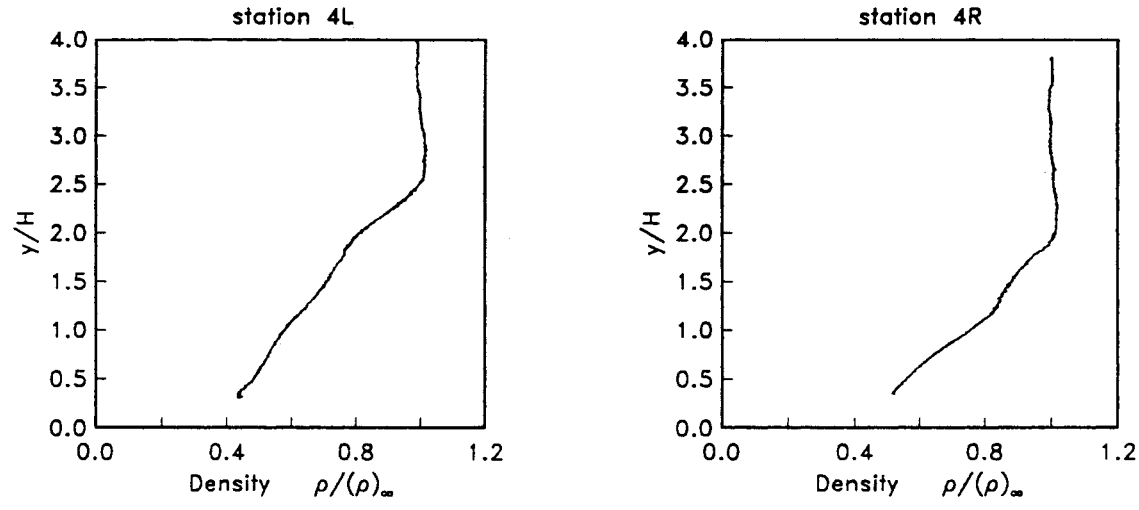

Figure 44. Density profiles, Stations 4L,4R, Case (G)

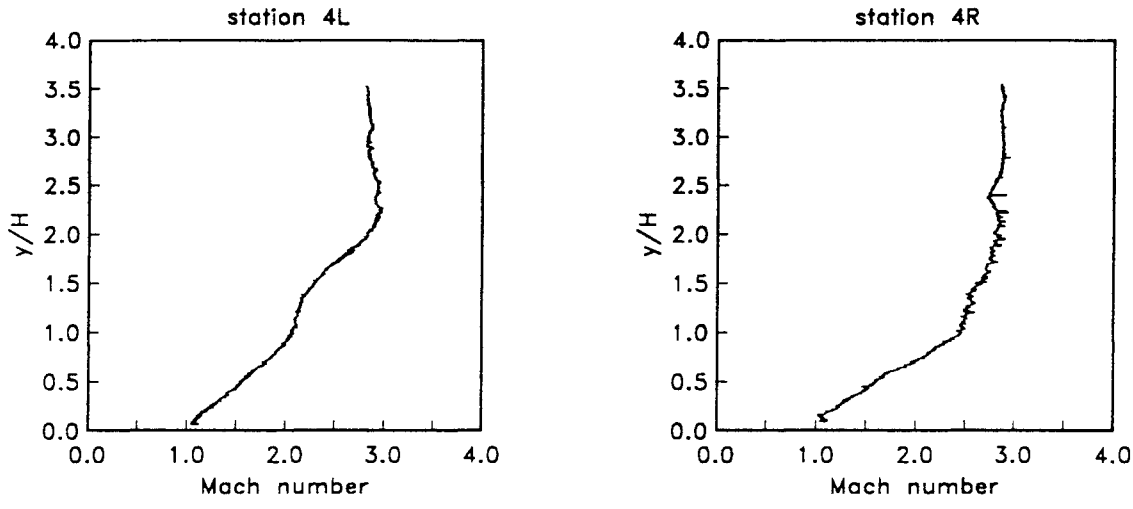

Figure 45. Mach number profiles, Stations 4L,4R, Case (H)

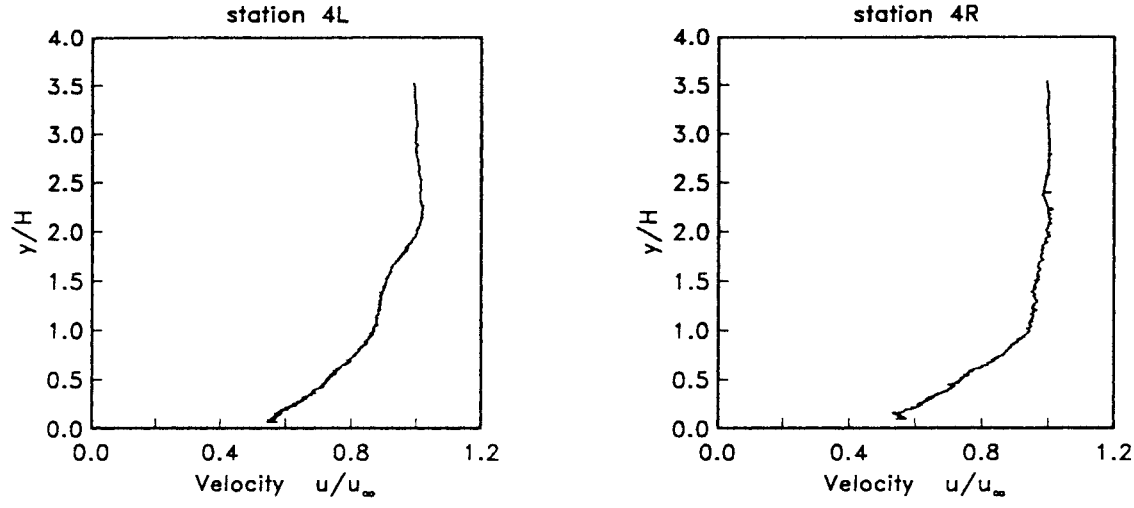

Figure 46. Velocity profiles, Stations 4L,4R, Case (H)

Attention Patron:

Page 93 omitted from numbering

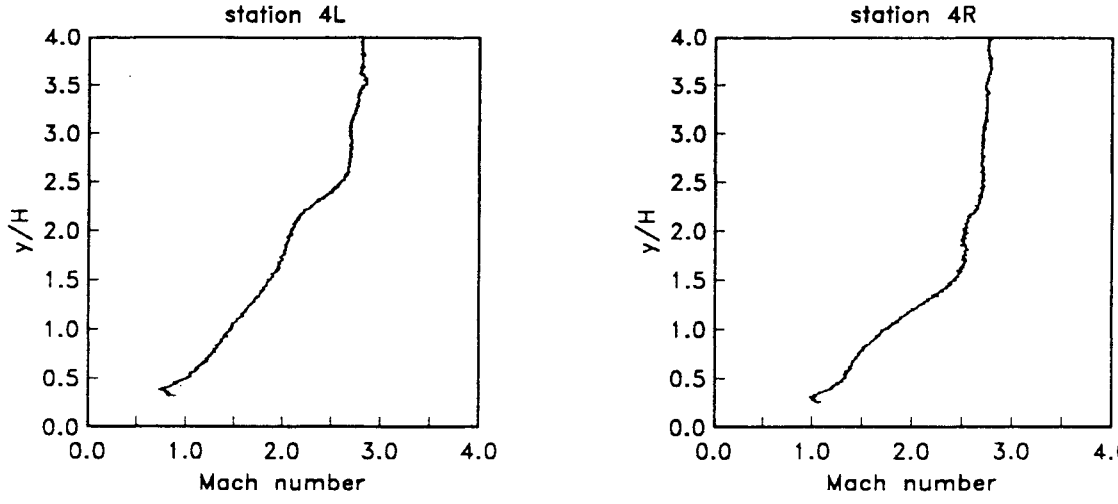

Figure 48. Mach number profiles, Stations 4L,4R, Case (I)

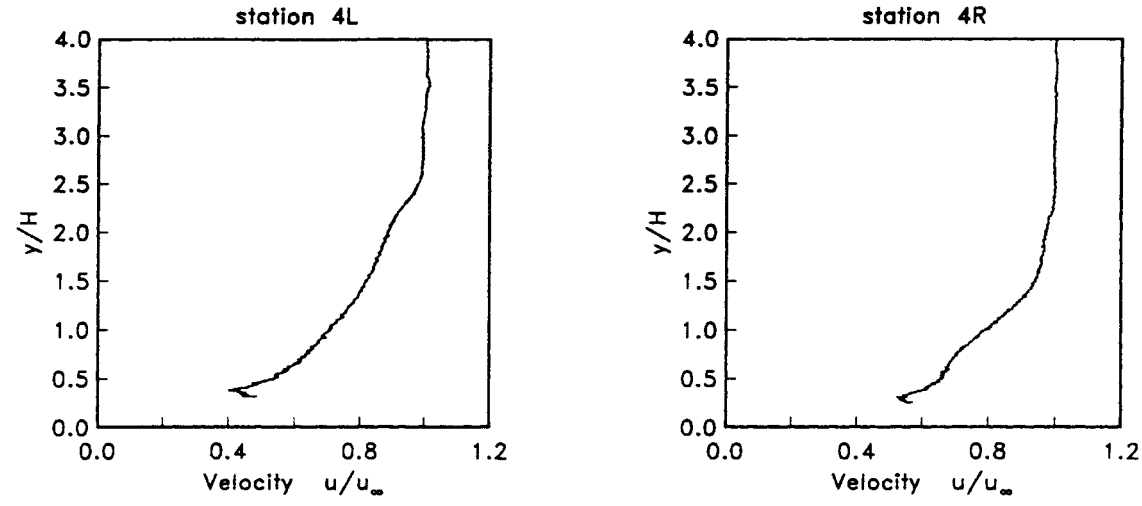

Figure 49. Velocity profiles, Stations 4L,4R, Case (I)

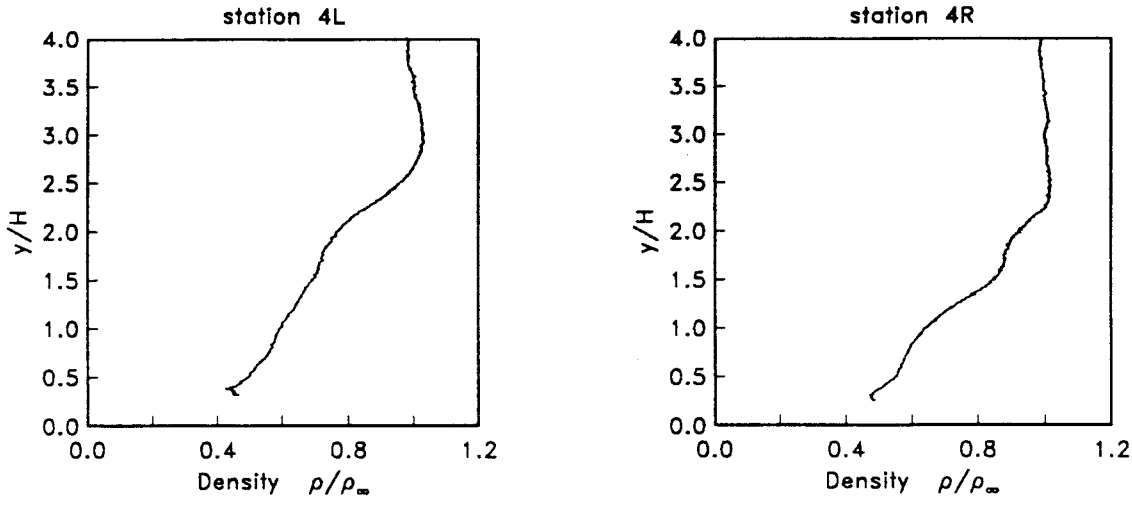

Figure 50. Density profiles, Stations 4L,4R, Case (I)

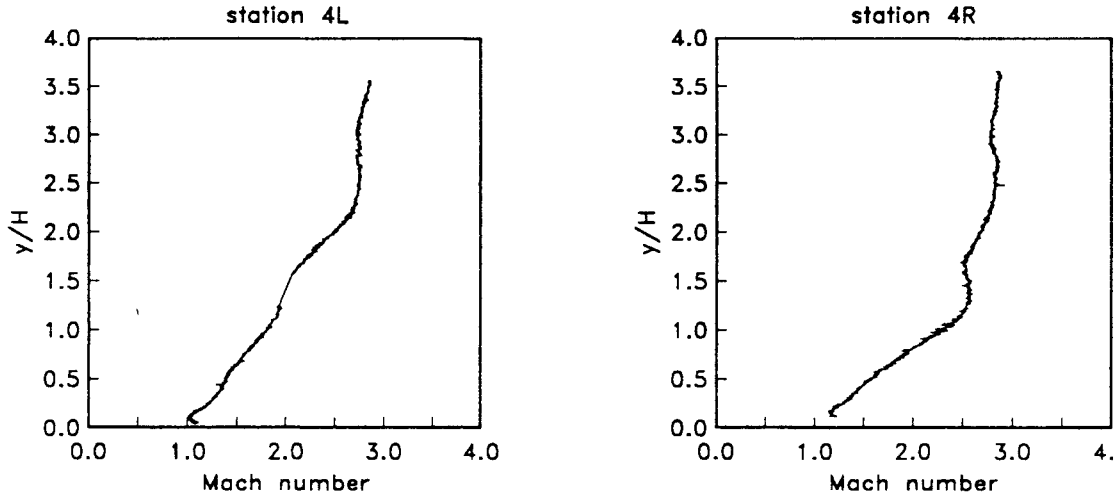

Figure 51. Mach number profiles, Stations 4L,4R, Case (J)

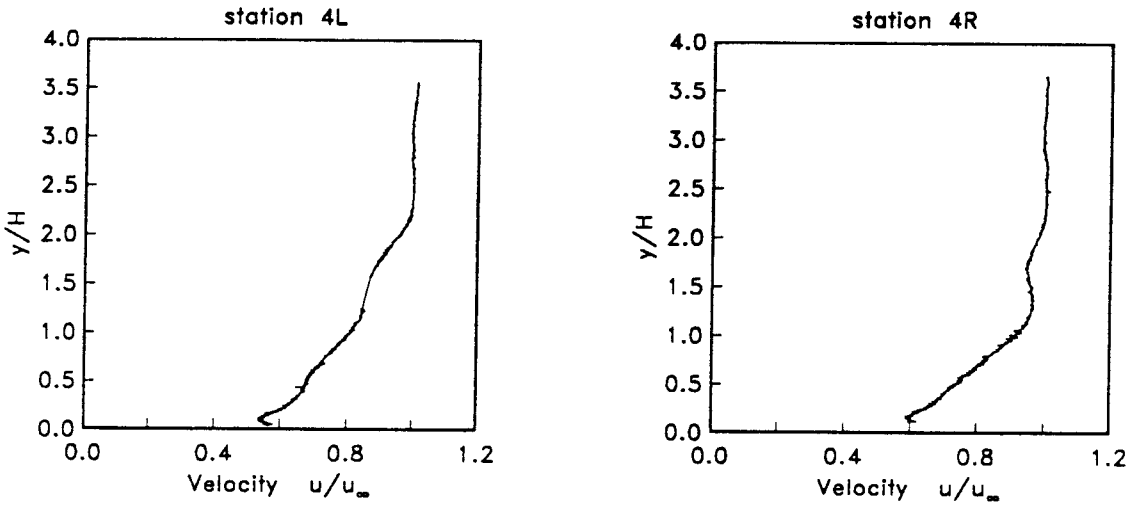

Figure 52. Velocity profiles, Stations 4L,4R, Case (J)

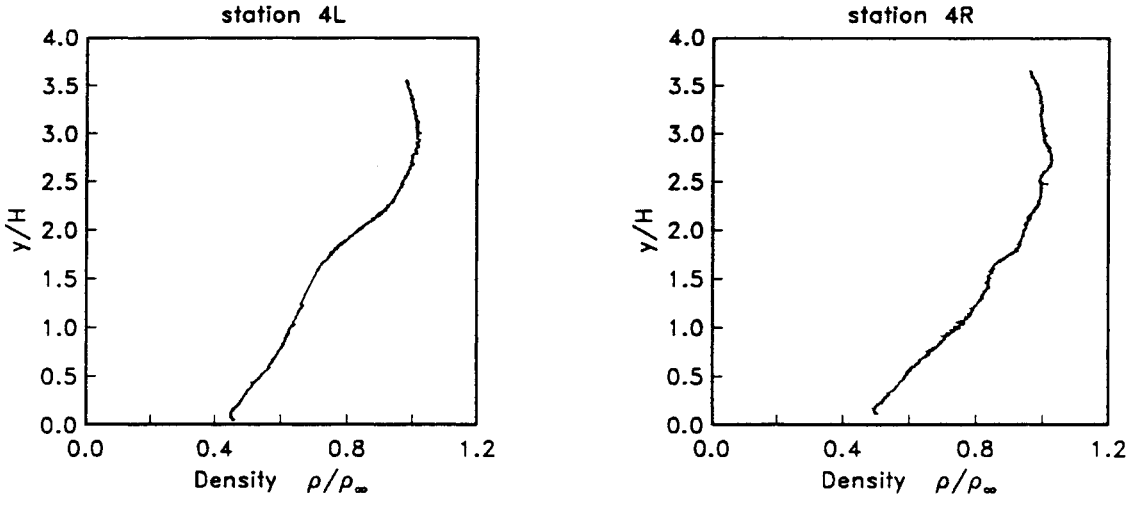

Figure 53. Density profiles, Stations 4L,4R, Case (J)

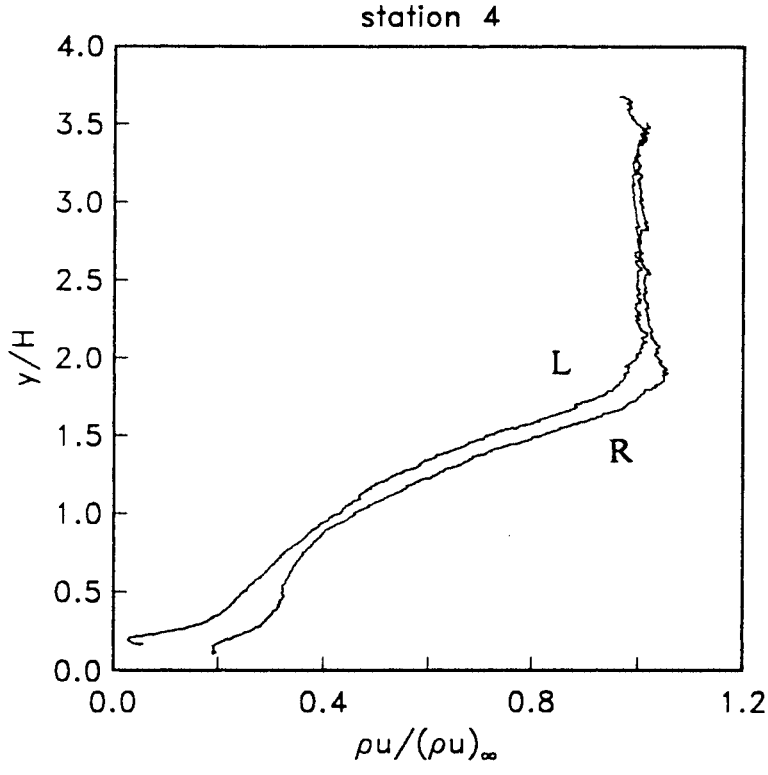

Figure 54. Mass flux profiles, Stations 4L,4R, Case (A)

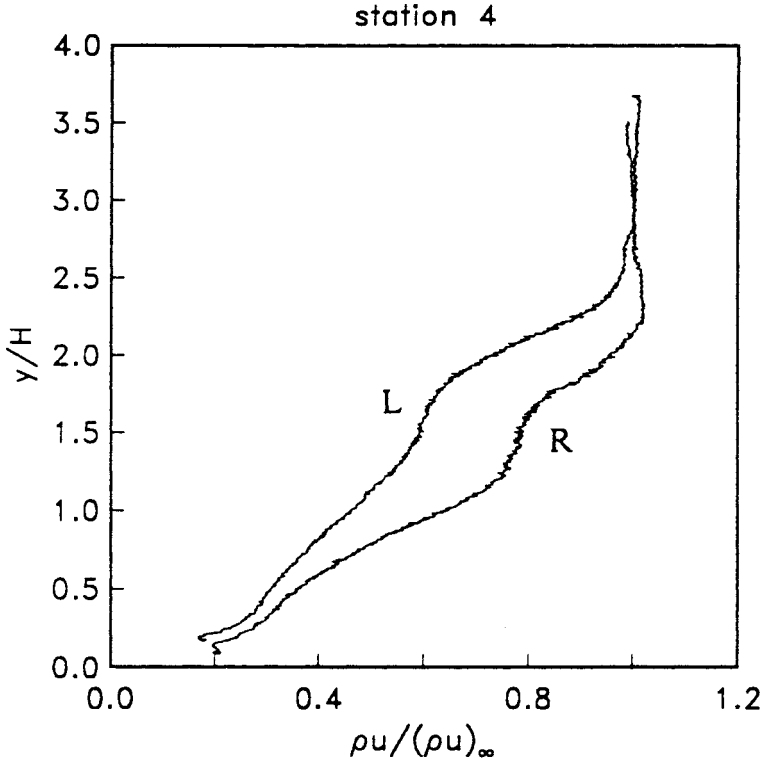

Figure 55. Mass flux profiles, Stations 4L,4R, Case (B)

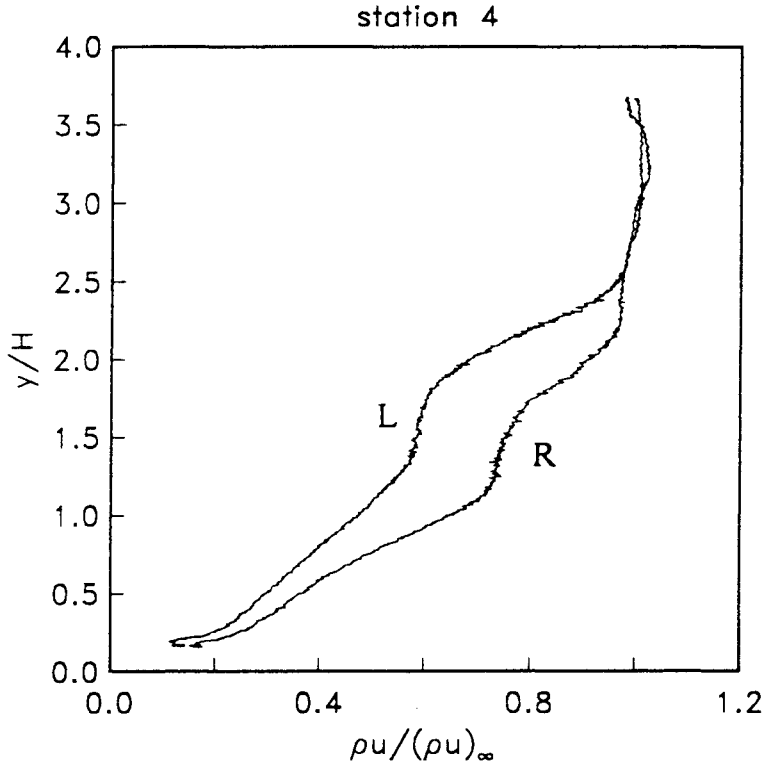

Figure 56. Mass flux profiles, Stations 4L,4R, Case (C)

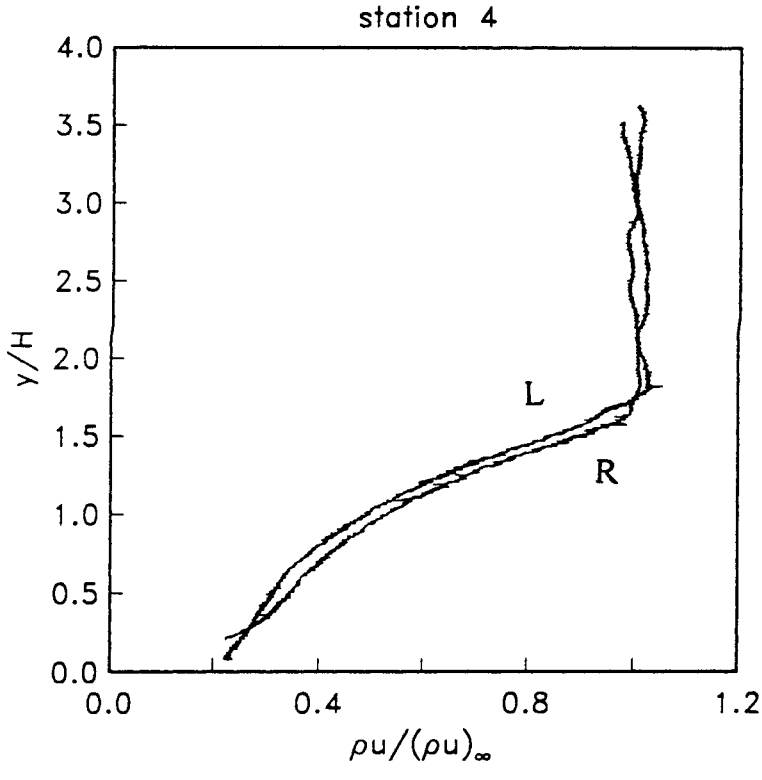

Figure 57. Mass flux profiles, Stations 4L,4R, Case (D)

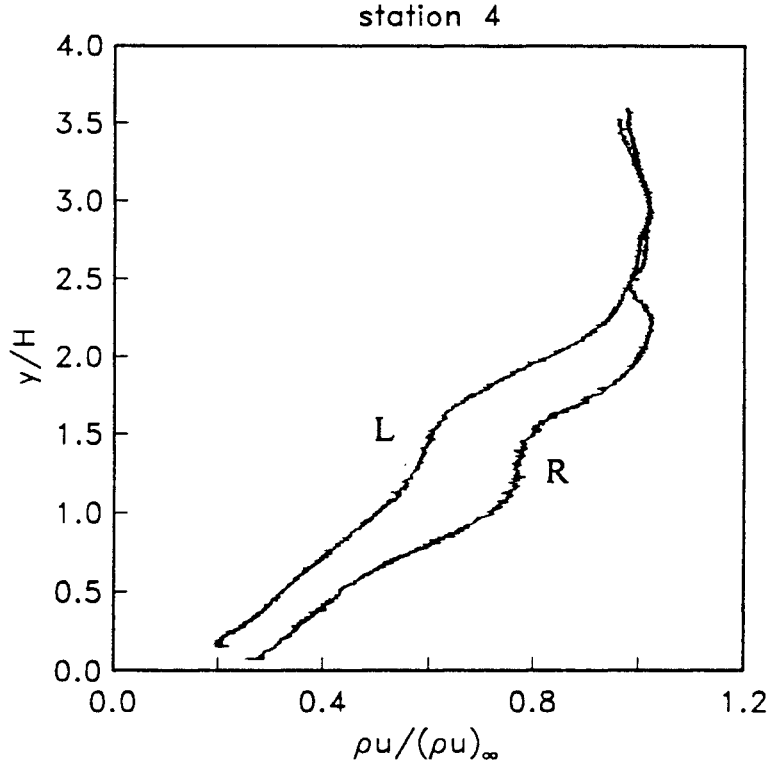

Figure 58. Mass flux profiles, Stations 4L,4R, Case (E)

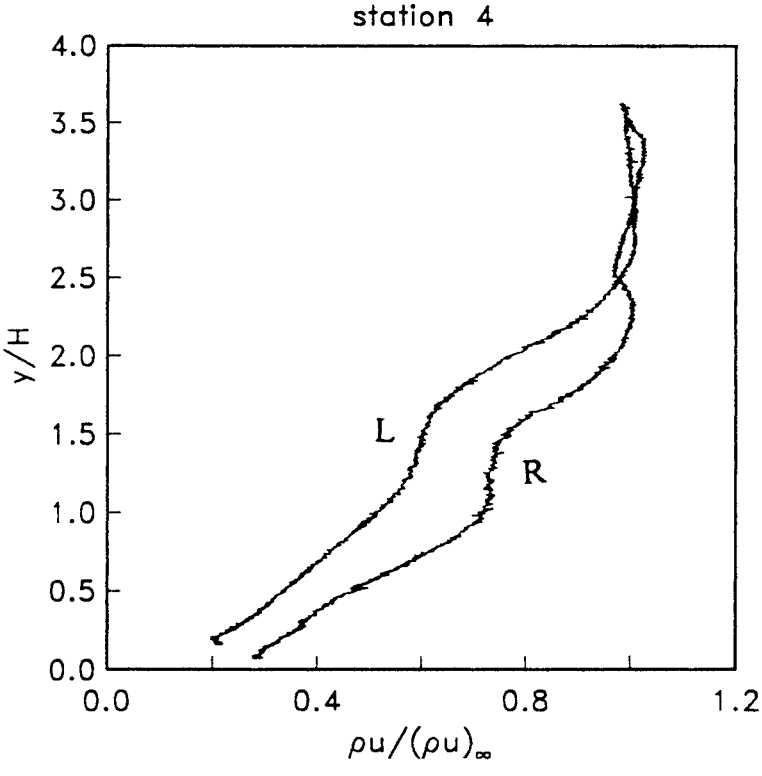

Figure 59. Mass flux profiles, Stations 4L,4R, Case (F)

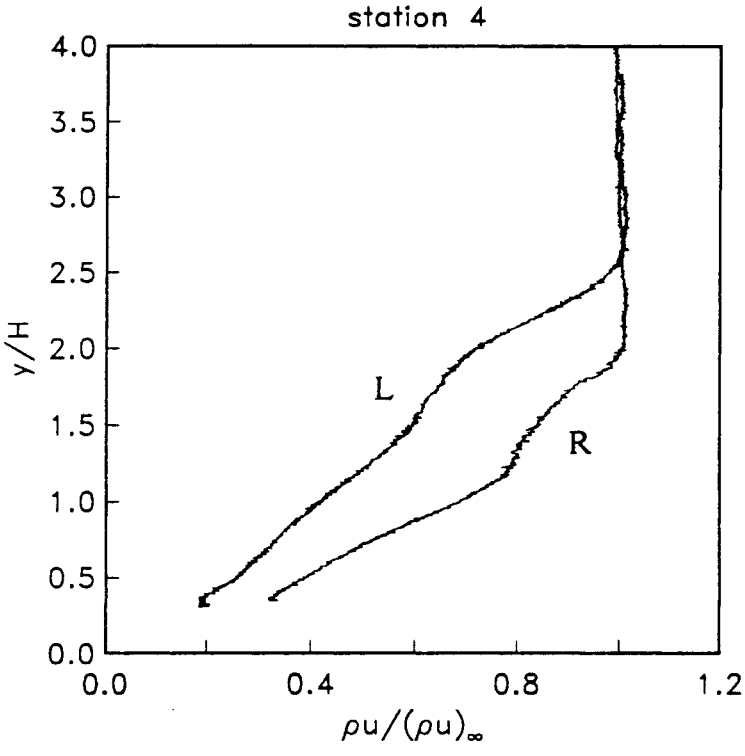

Figure 60. Mass flux profiles, Stations 4L,4R, Case (G)

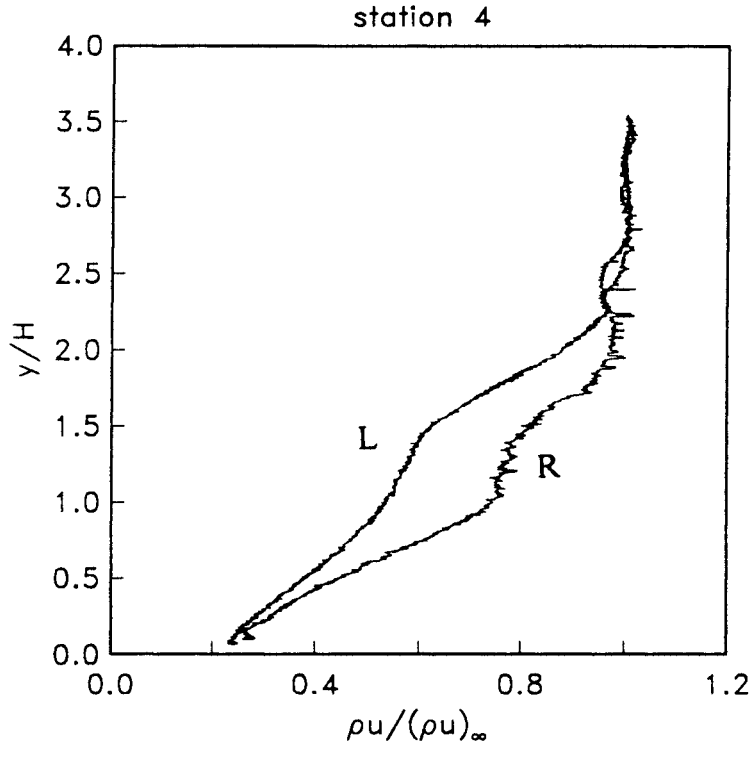

Figure 61. Mass flux profiles, Stations 4L,4R, Case (H)

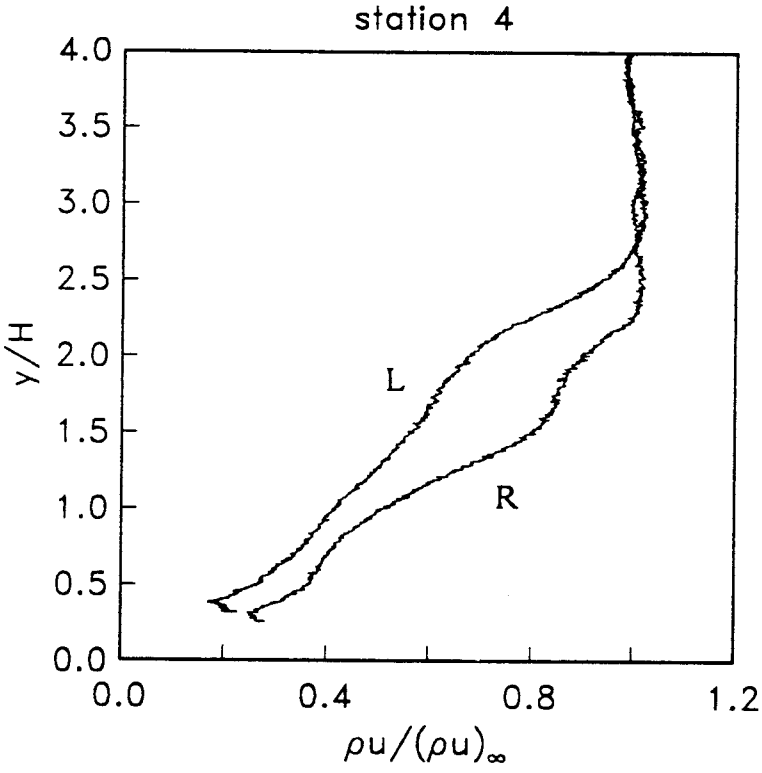

Figure 62. Mass flux profiles, Stations 4L,4R, Case (I)

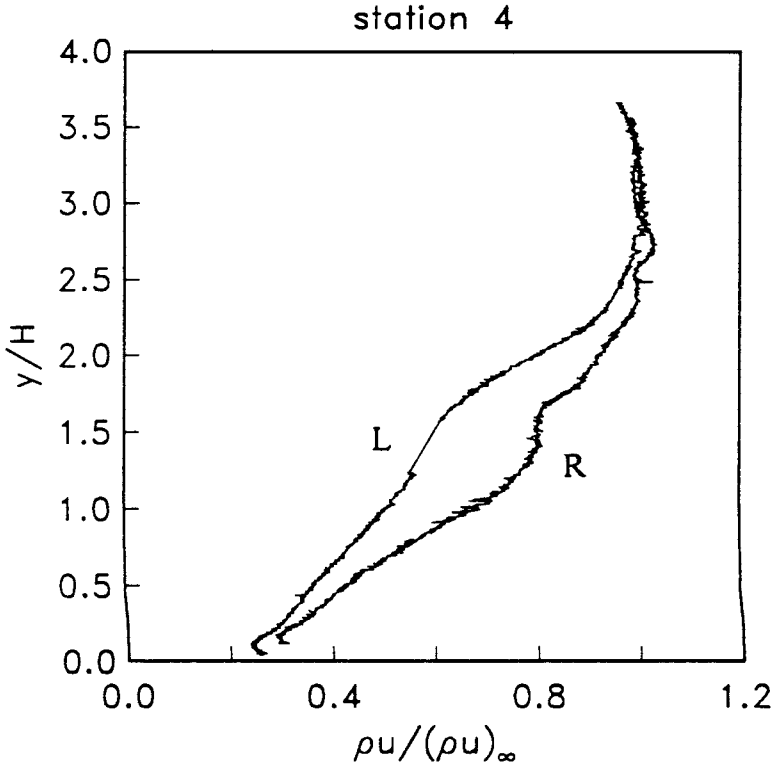

Figure 63. Mass flux profiles, Stations 4L,4R, Case (J)

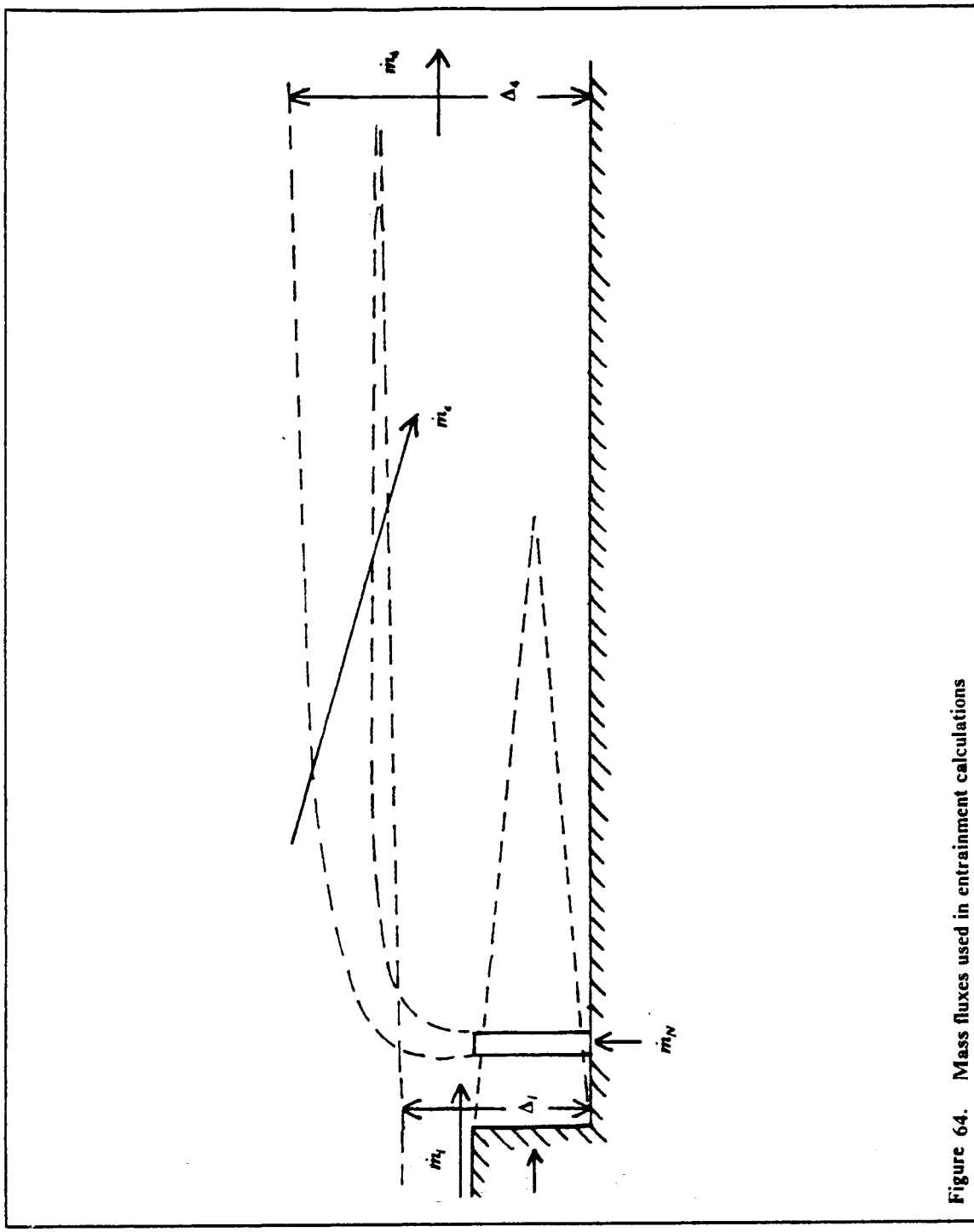

Figure 64. Mass fluxes used in entrainment calculations

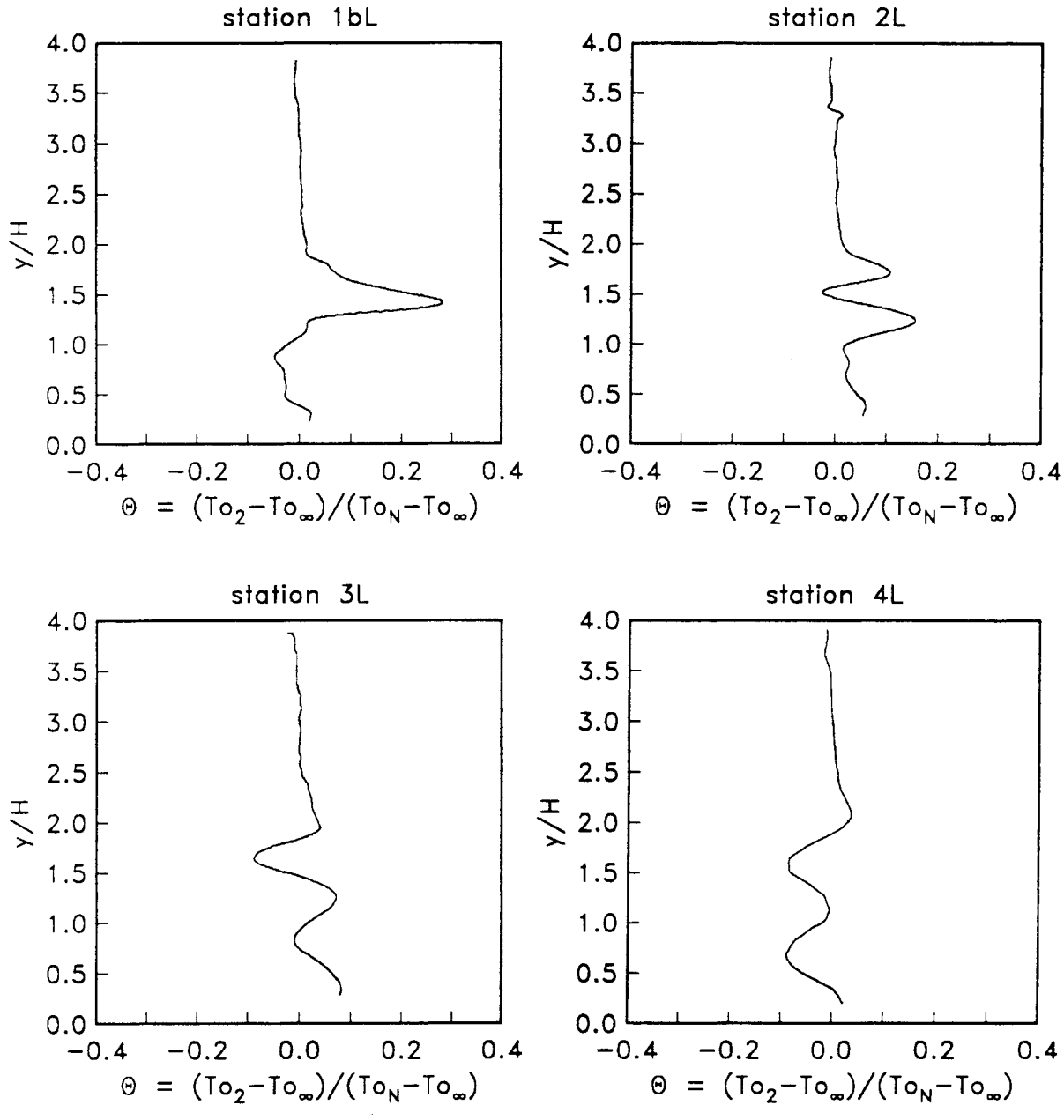

Figure 65. Nondimensional temperature, case (B)

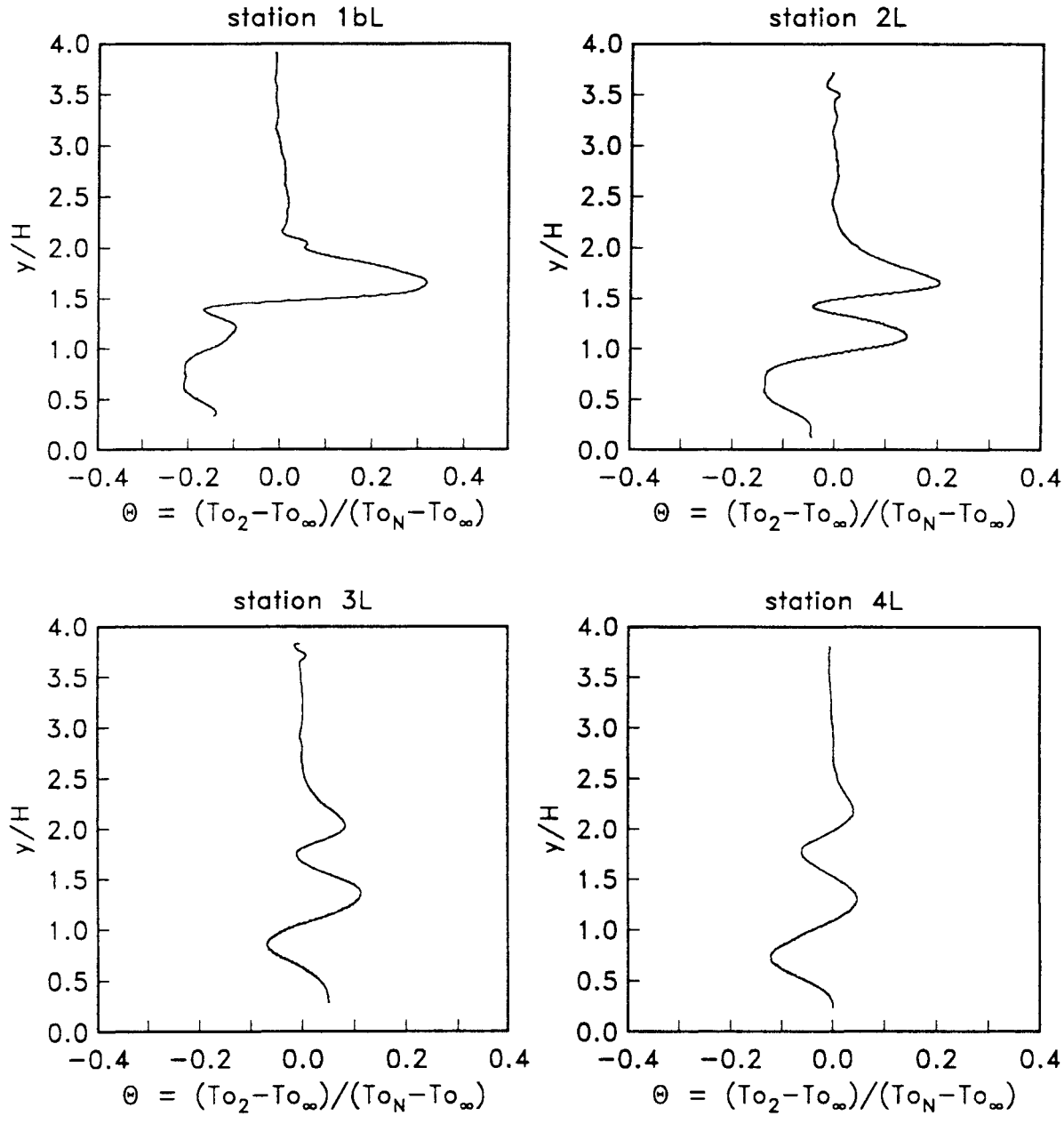

Figure 66. Nondimensional temperature, case (E)

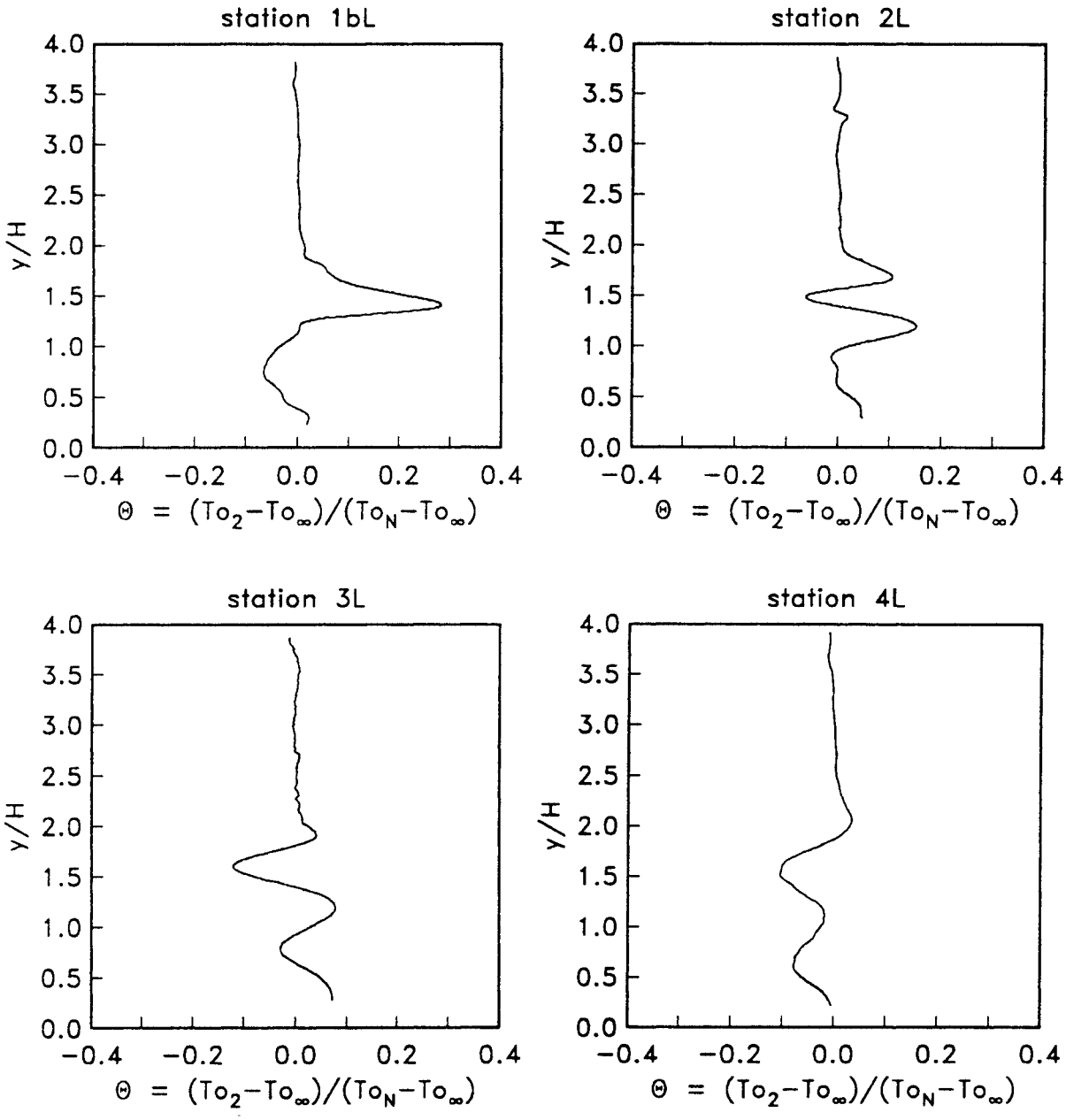

Figure 67. Nondimensional temperature, case (G)

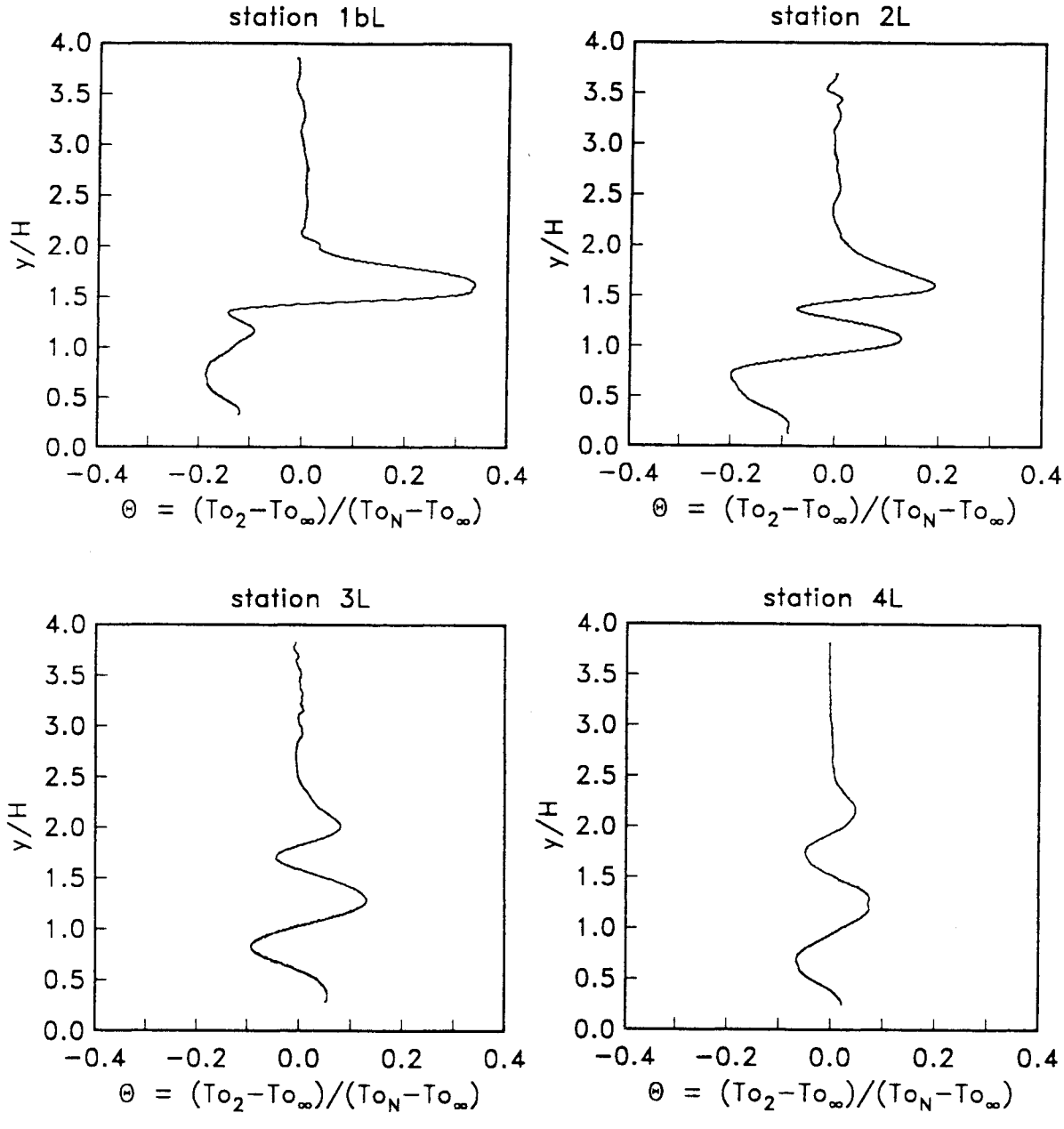

Figure 68. Nondimensional temperature, case (H)

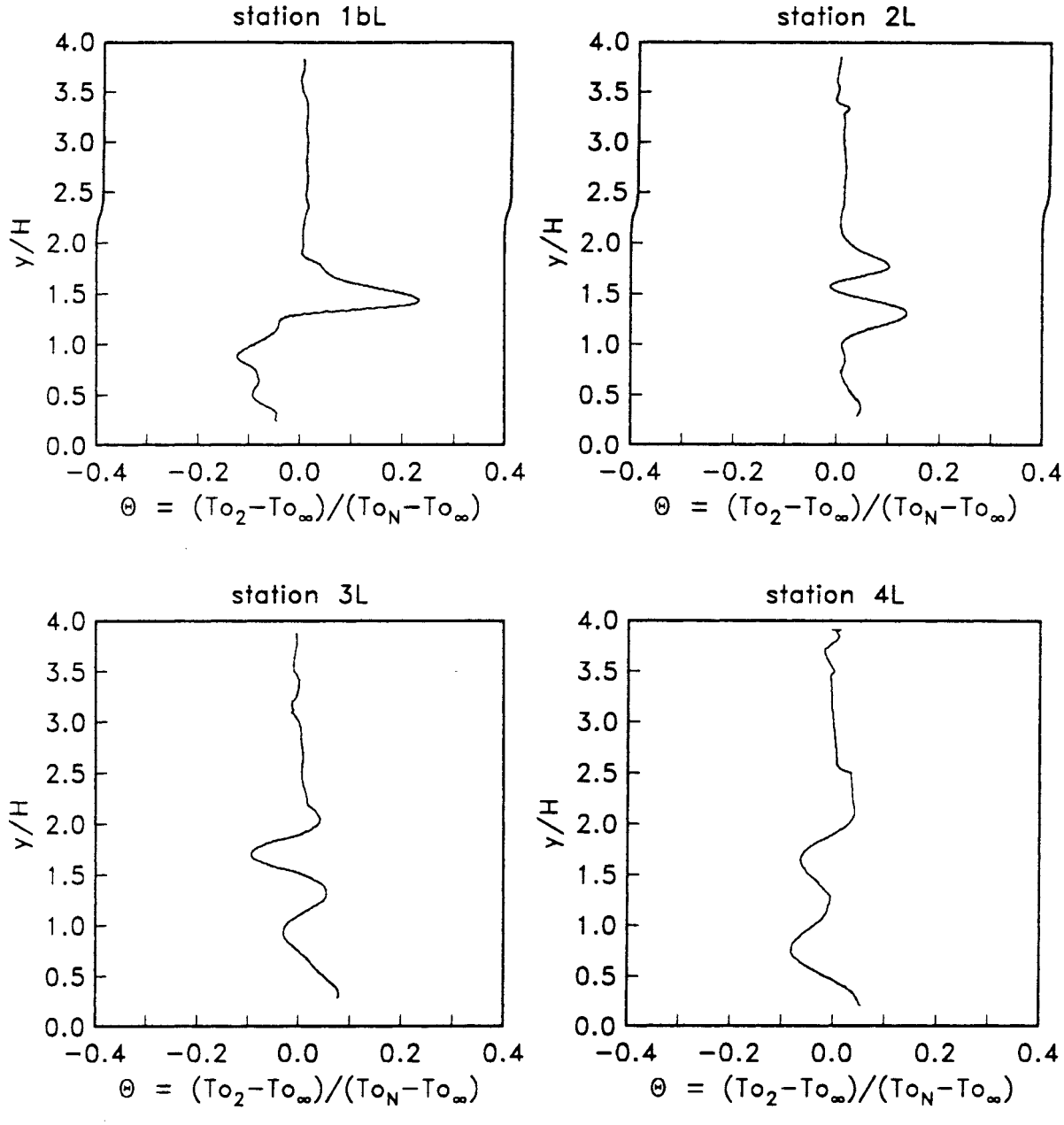

Figure 69. Nondimensional temperature, case (I)

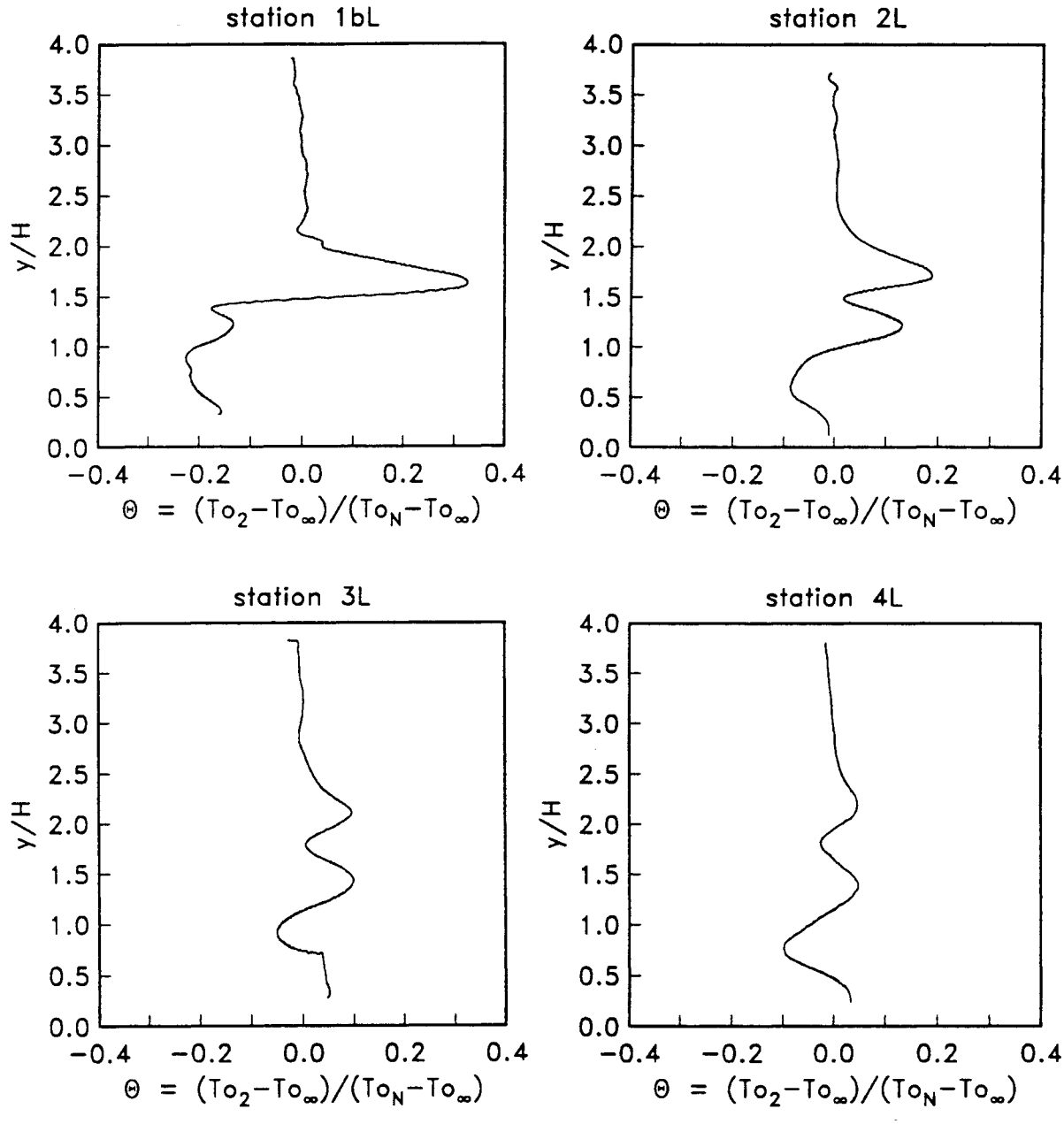

Figure 70. Nondimensional temperature, case (J)

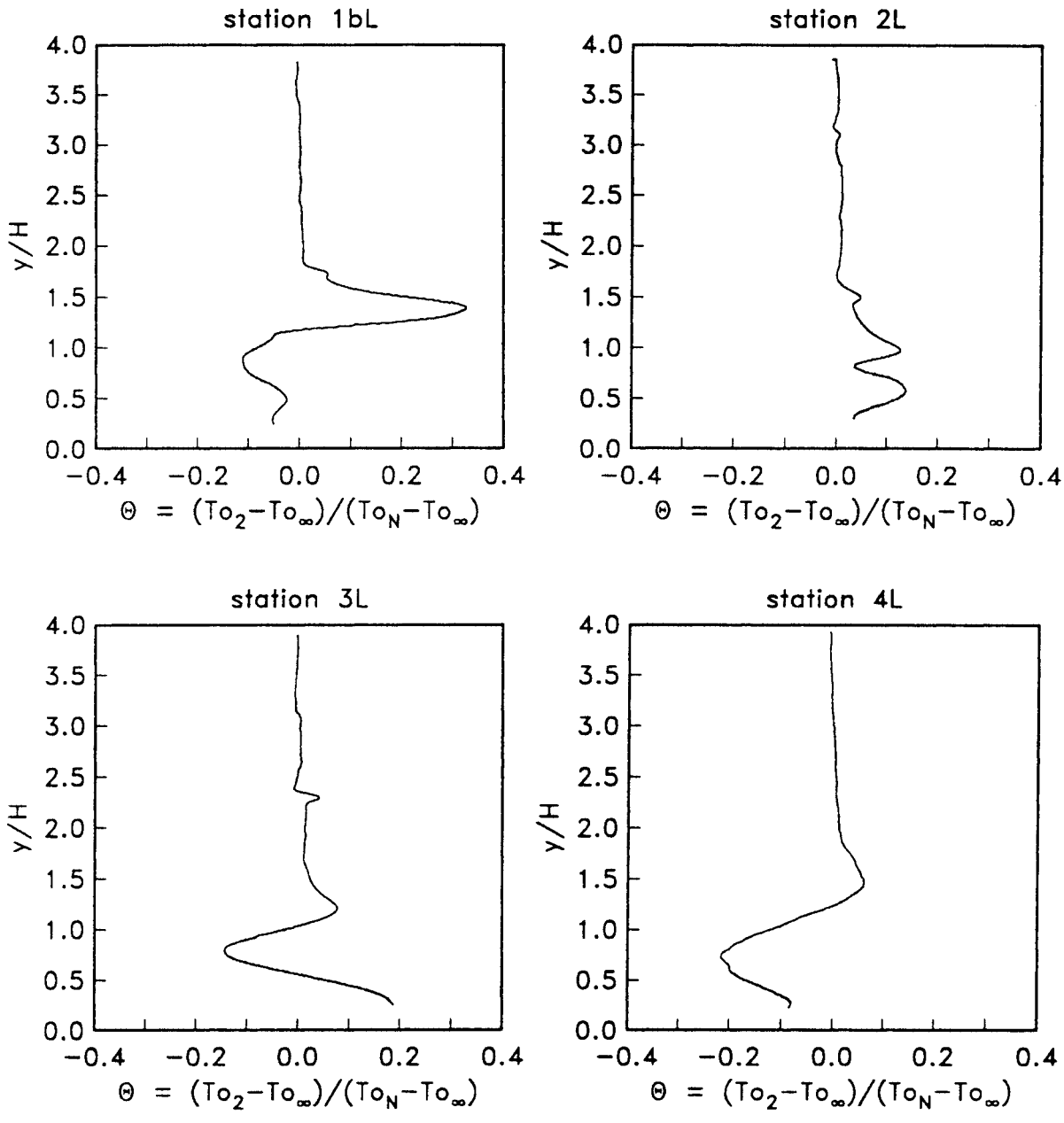

Figure 71. Nondimensional temperature, sonic jets, slot closed

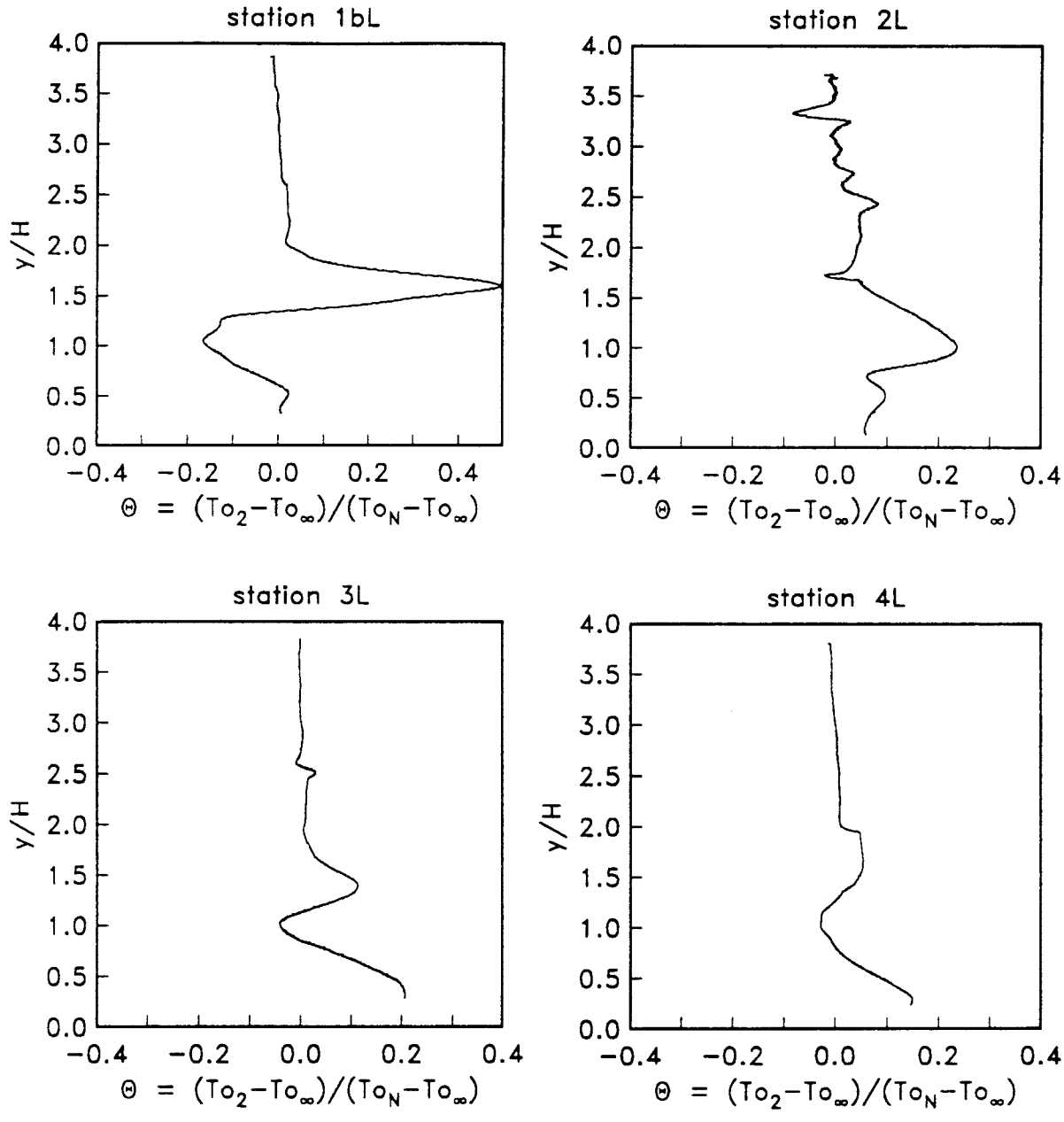

Figure 72. Nondimensional temperature, supersonic jets, slot closed

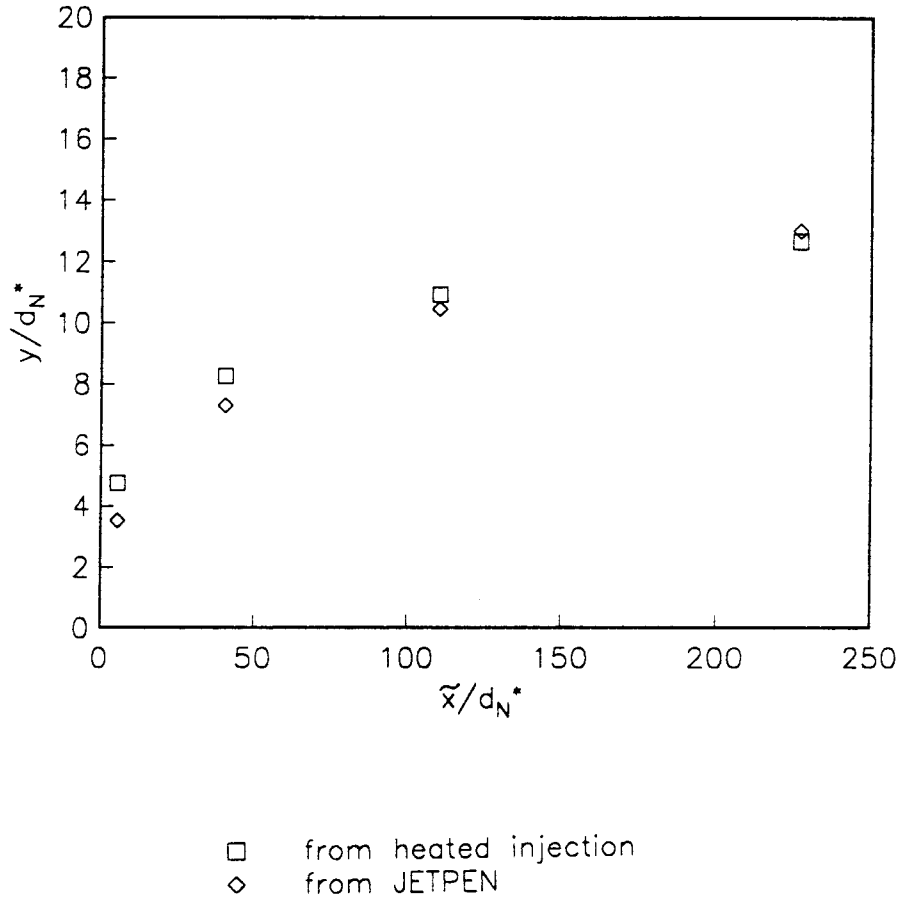

Figure 73. Normal jet trajectories, Case (B)

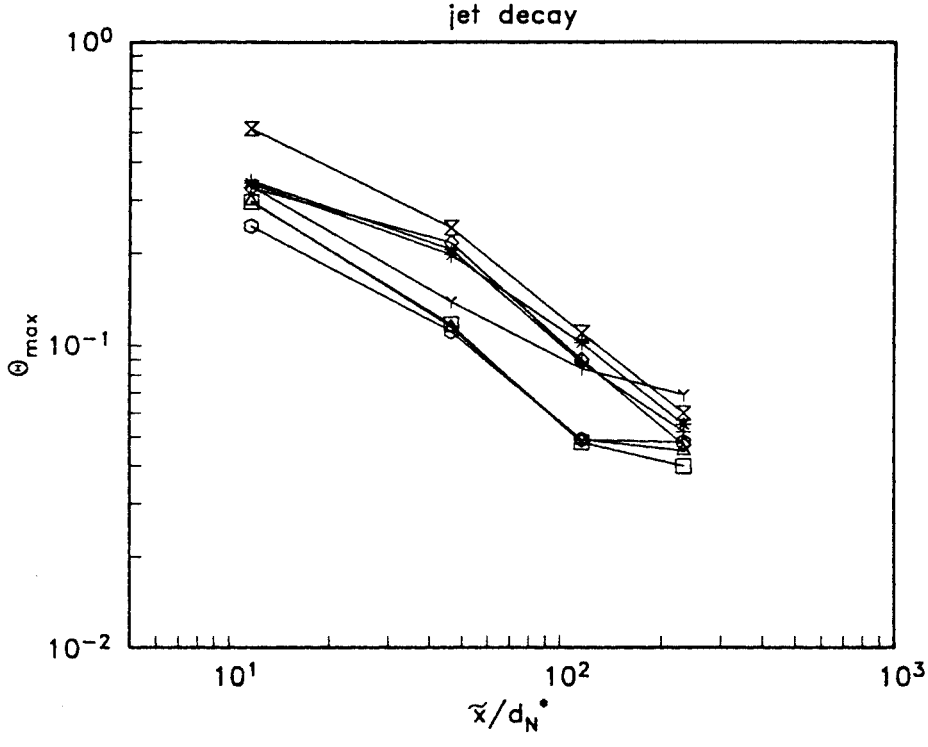

Figure 74. Jet temperature decay

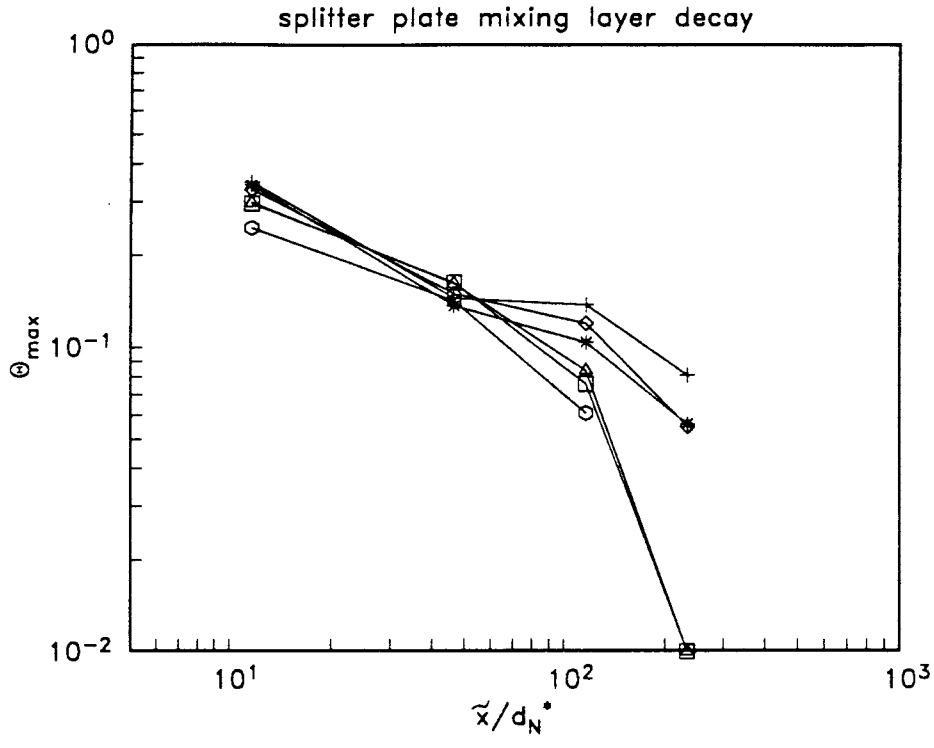

Figure 75. Splitter plate mixing layer temperature decay

Appendix A

Dimensional Mean Flow Profiles

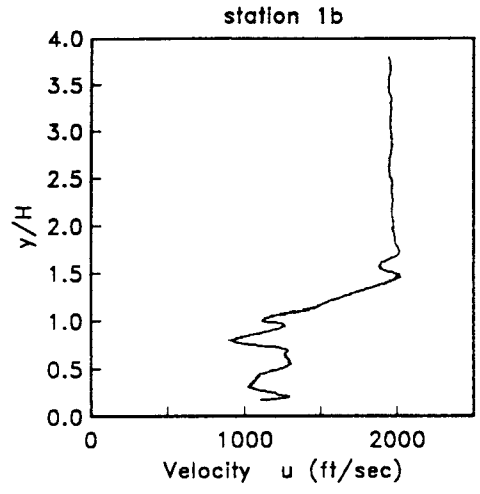

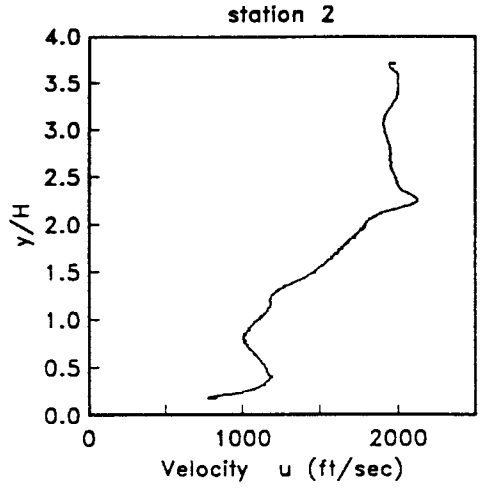

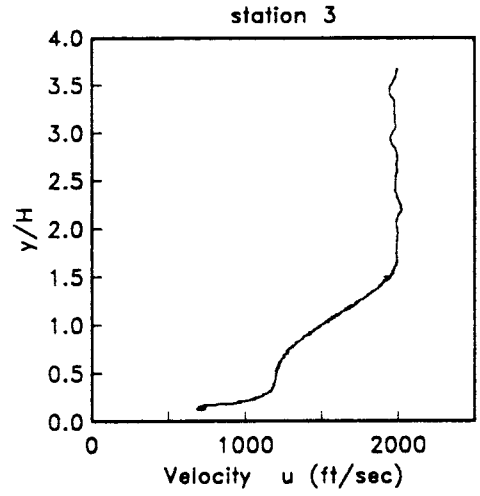

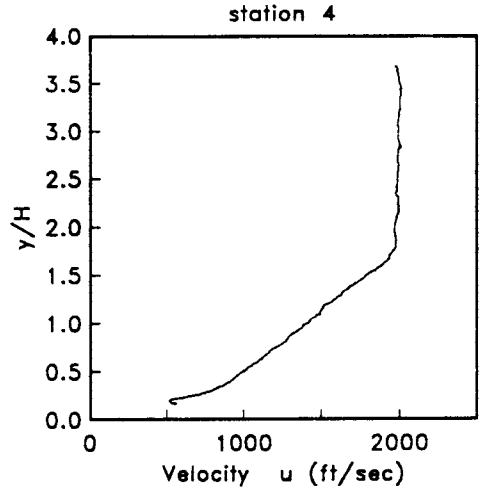

Velocity profiles, left side, Case (A)

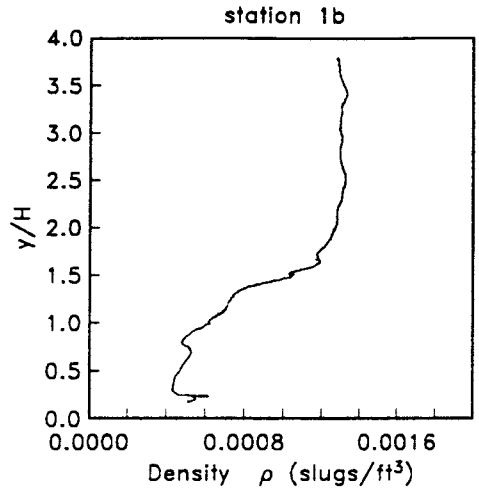

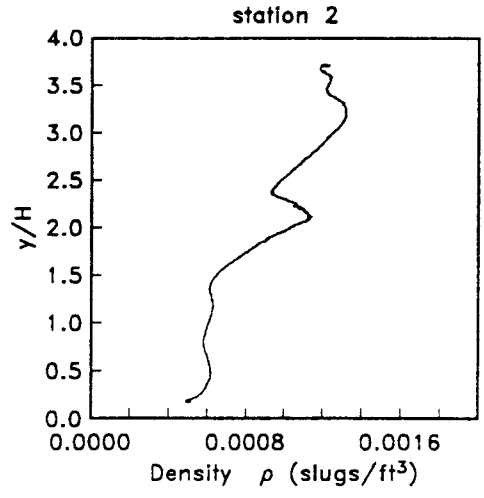

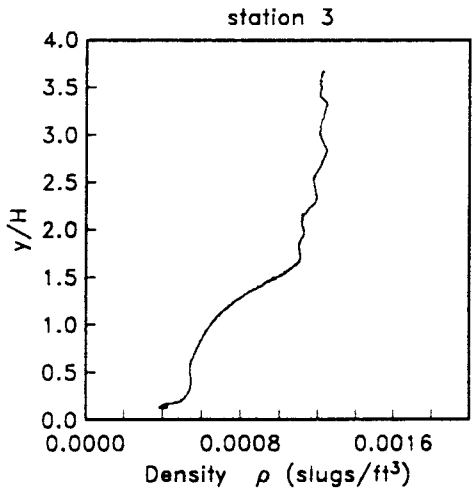

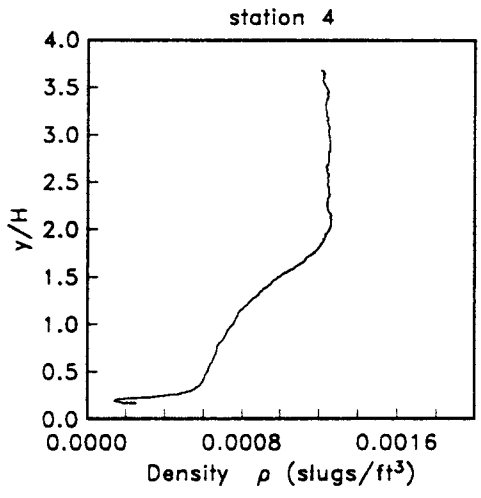

Density profiles, left side, Case (A)

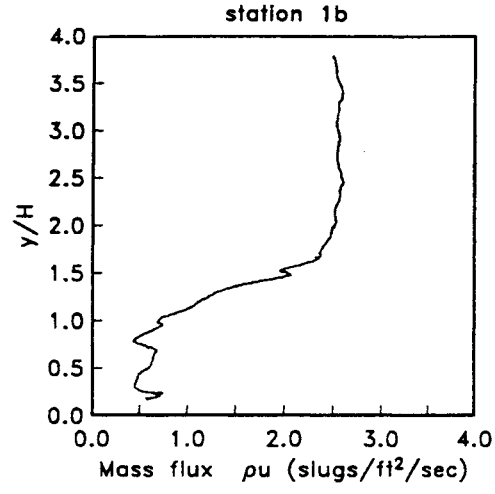

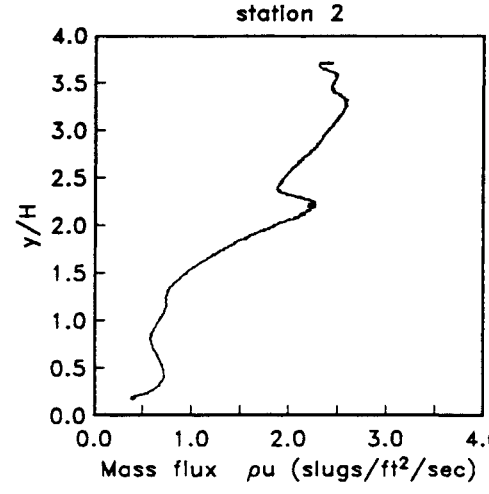

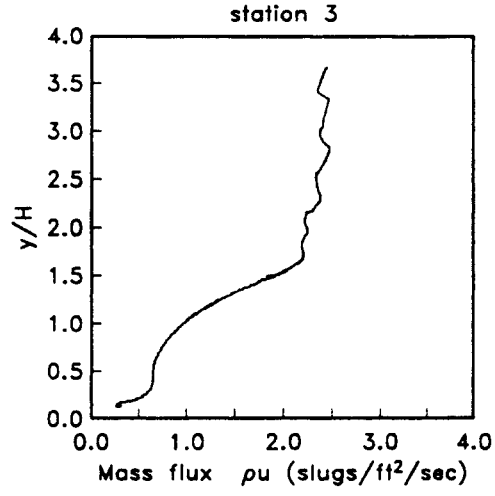

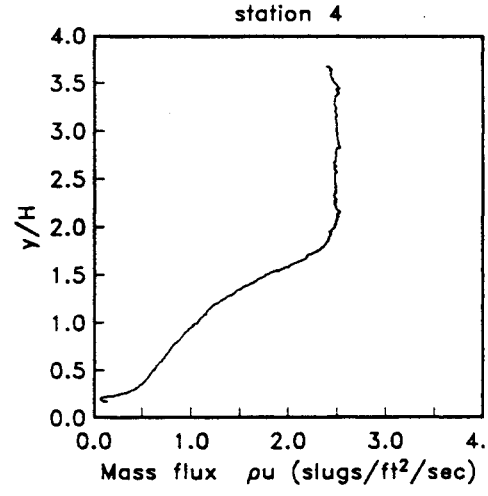

Mass flux profiles, left side, Case (A)

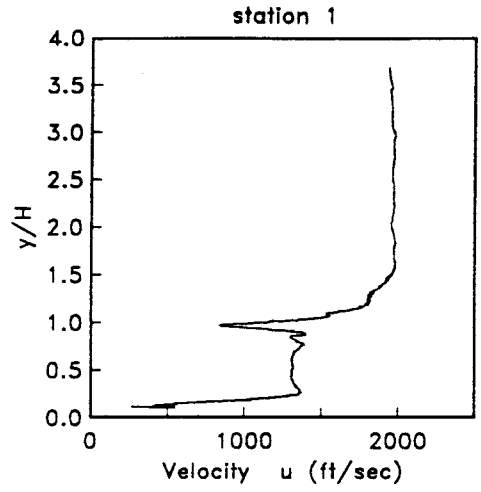

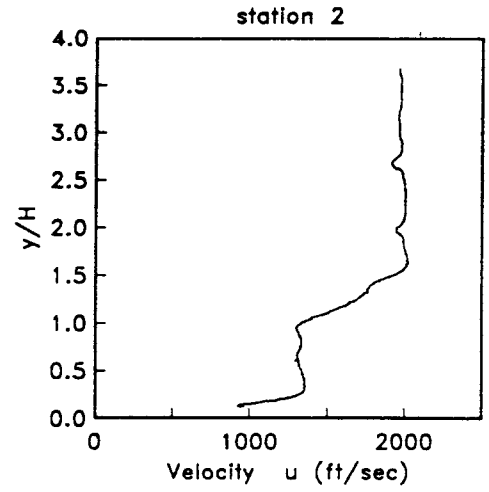

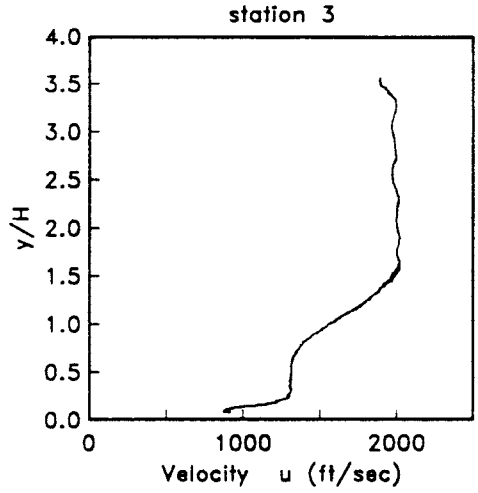

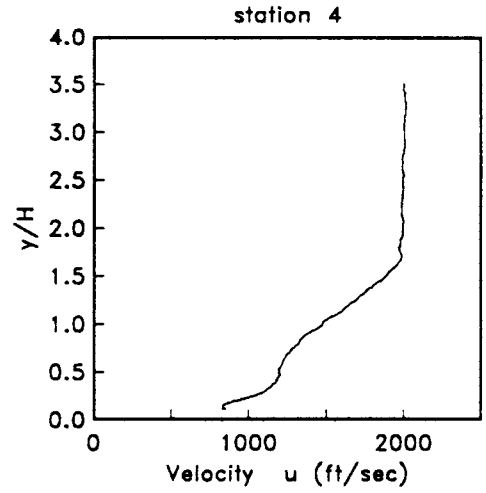

Velocity profiles, right side, Case (A)

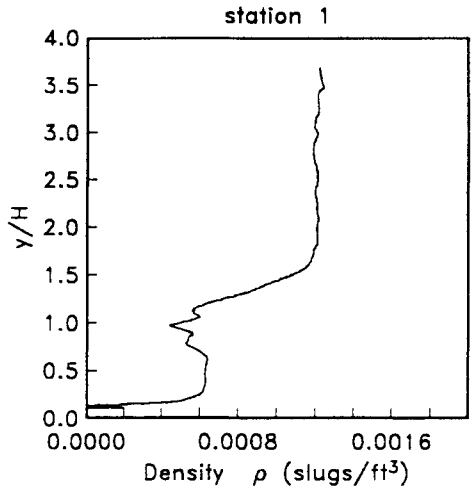

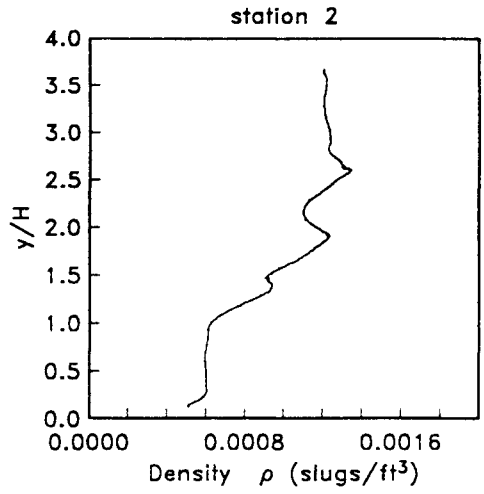

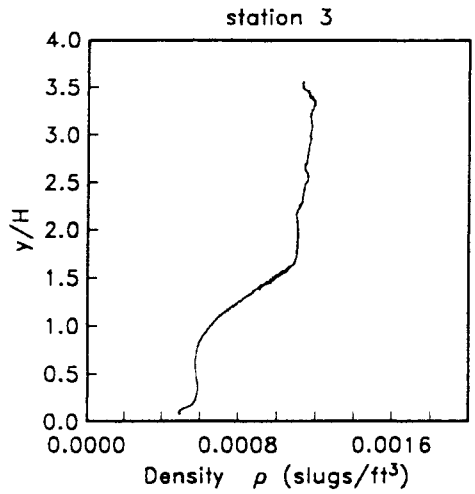

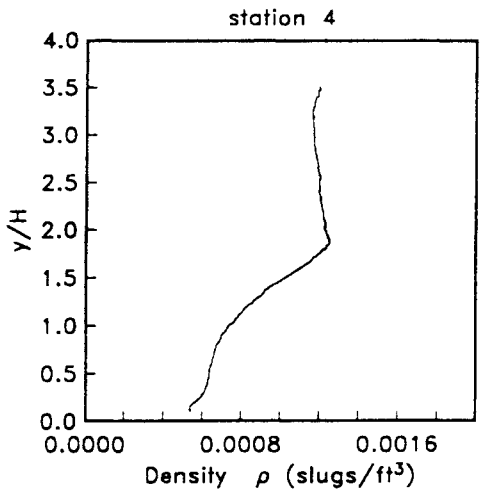

Density profiles, right side, Case (A)

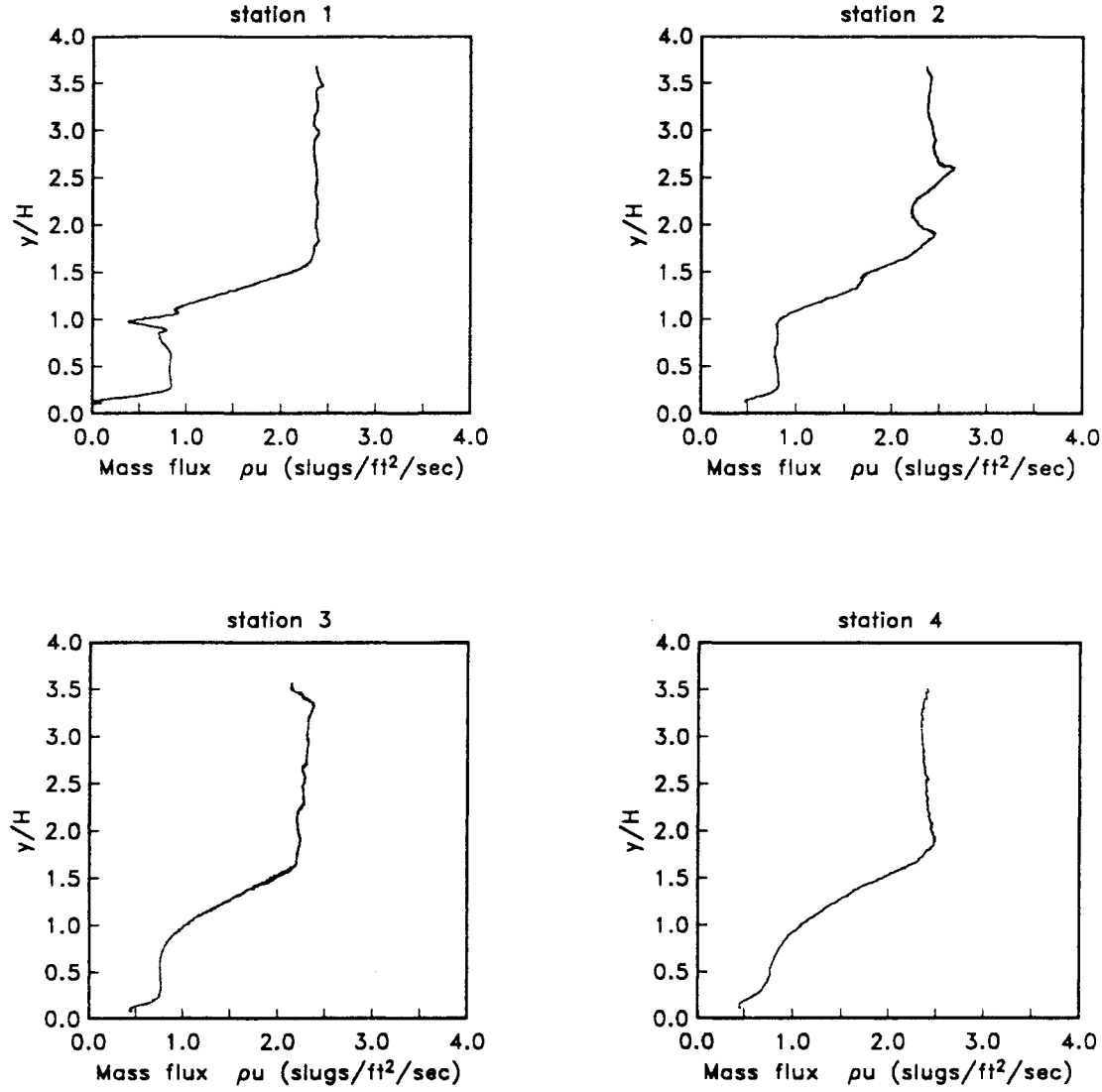

Mass flux profiles, right side, Case (A)

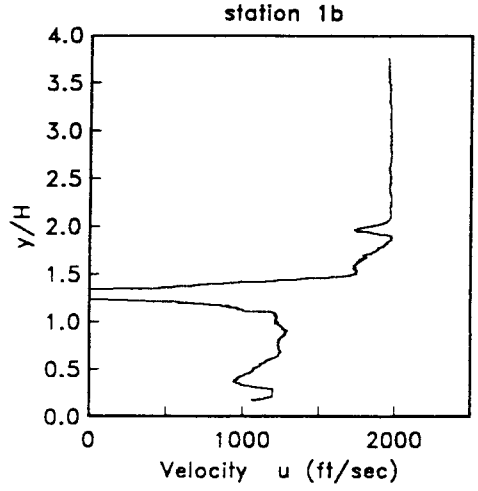

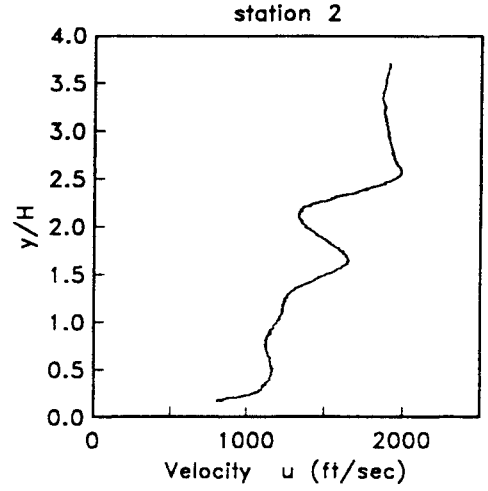

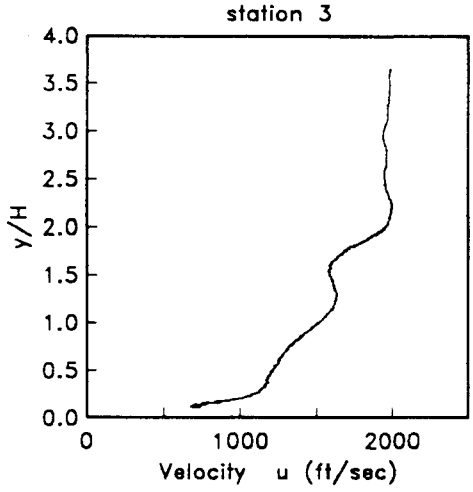

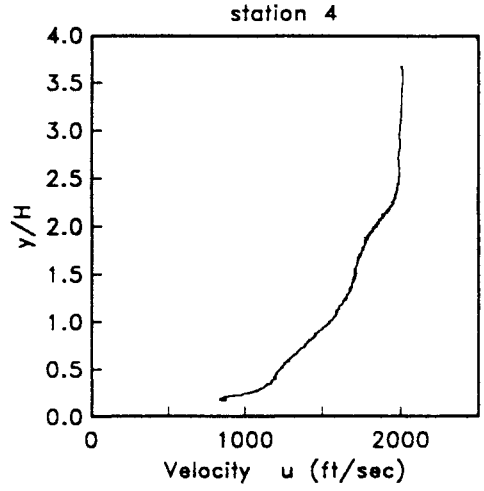

Velocity profiles, left side, Case (B)

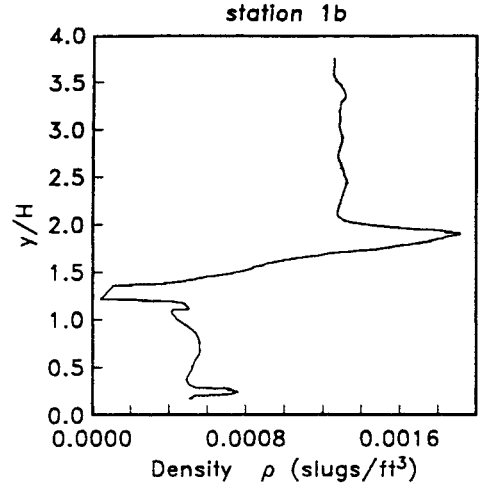

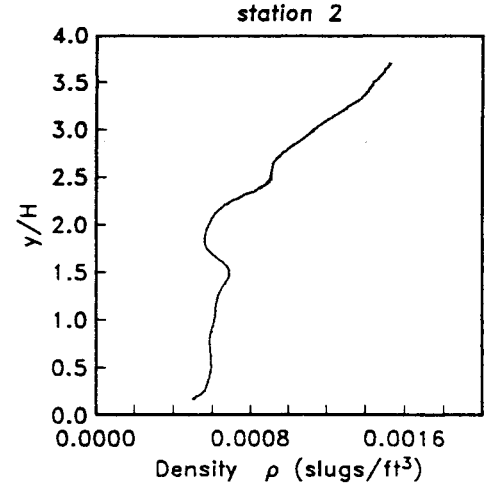

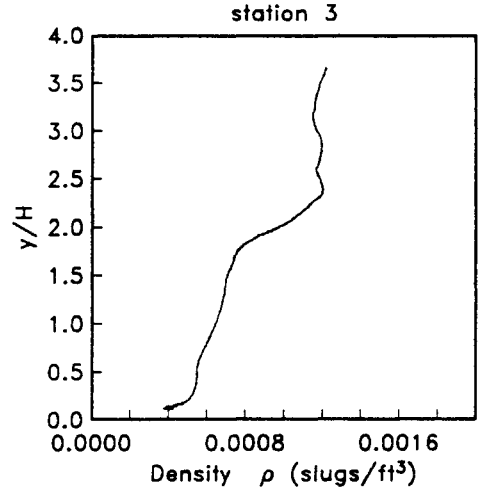

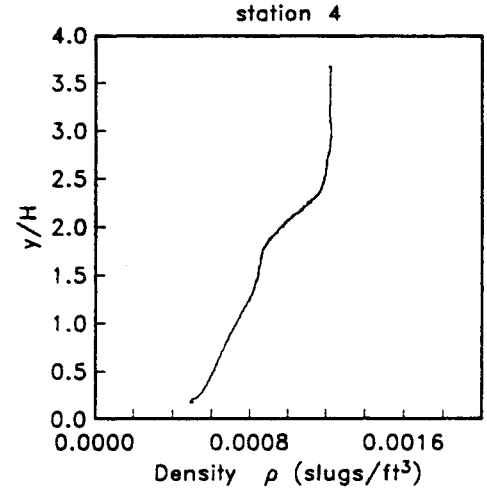

Density profiles, left side, Case (B)

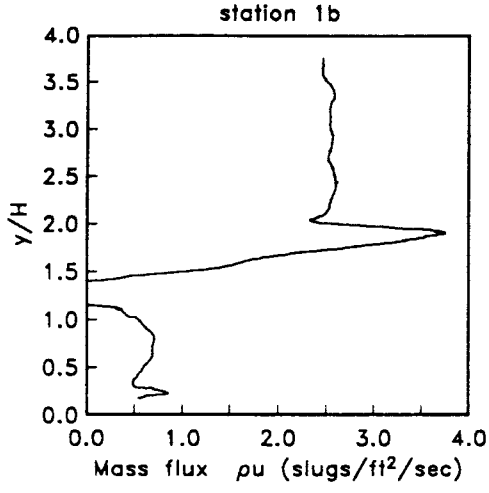

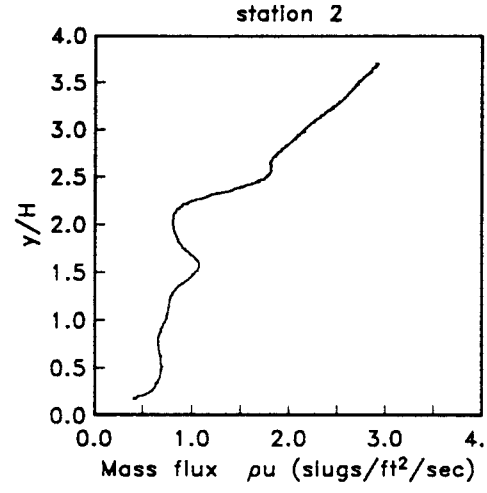

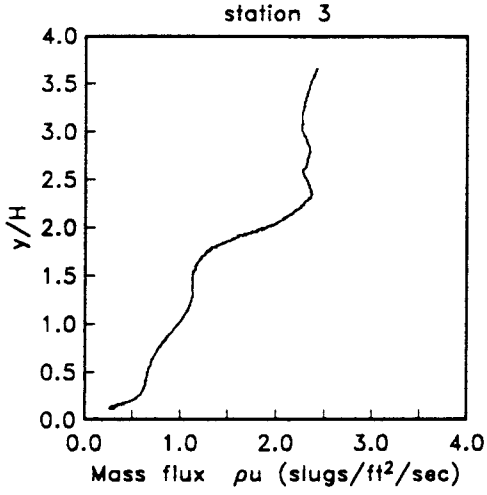

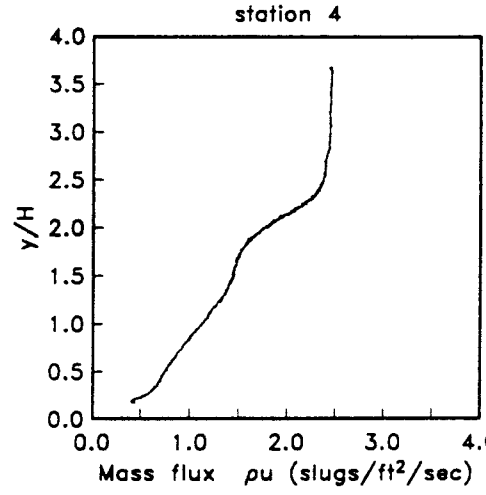

Mass flux profiles, left side, Case (B)

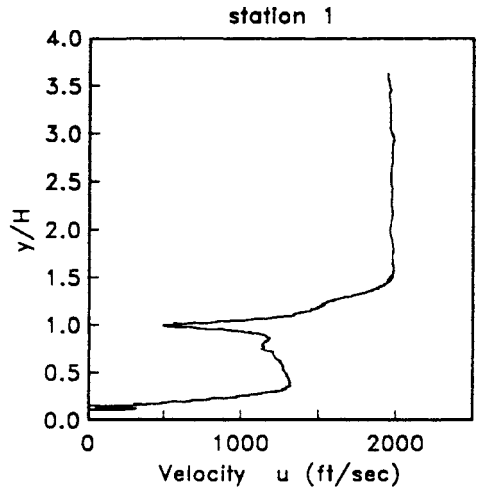

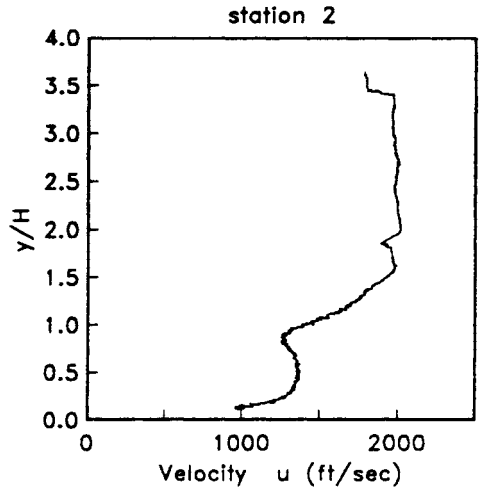

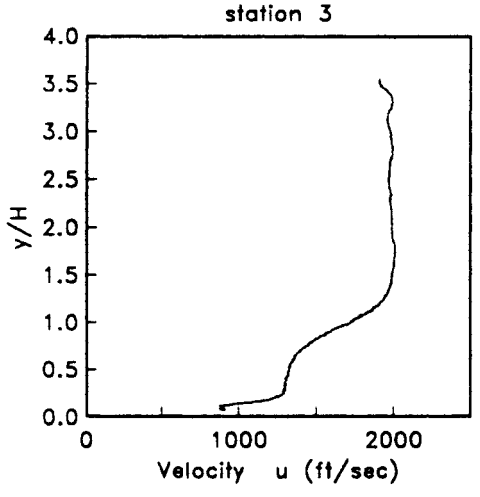

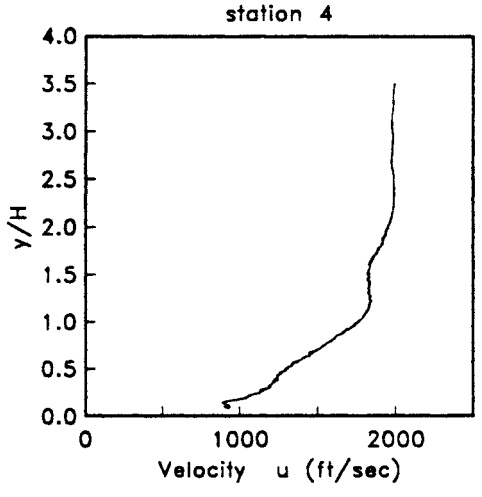

Velocity profiles, right side, Case (B)

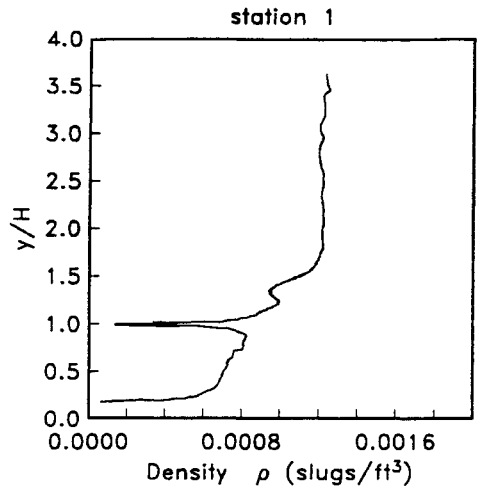

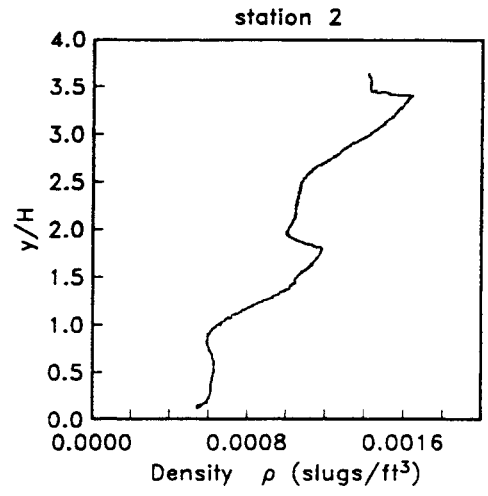

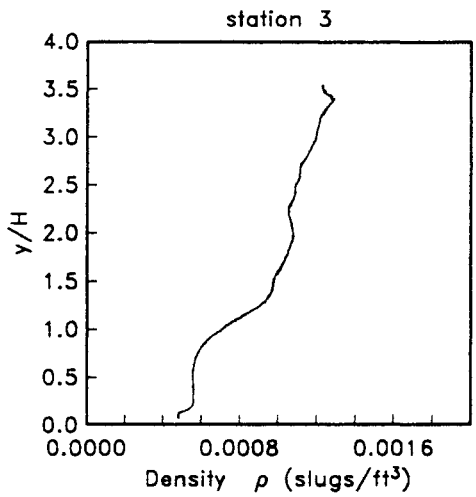

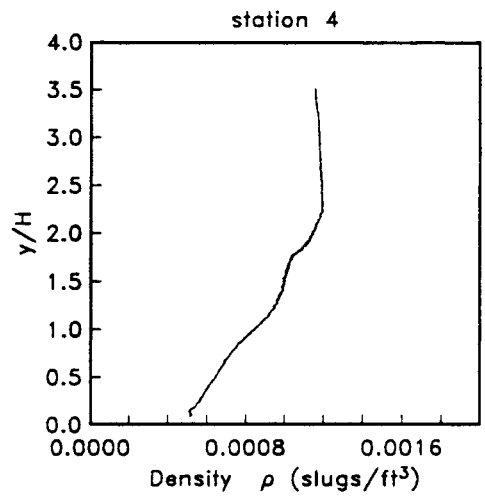

Density profiles, right side, Case (B)

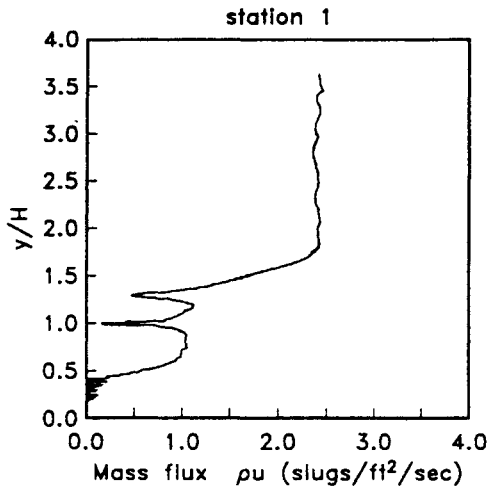

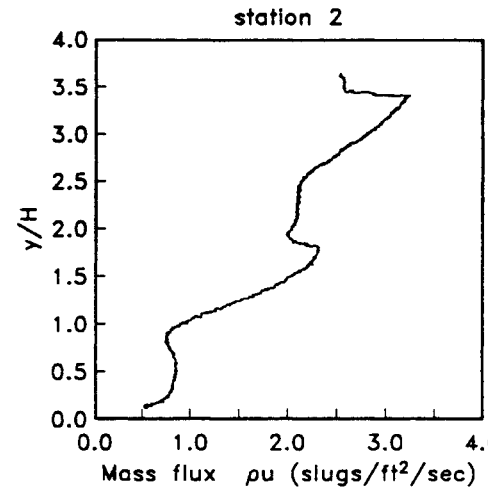

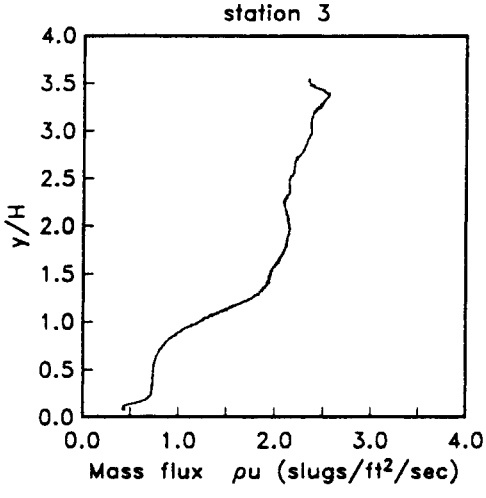

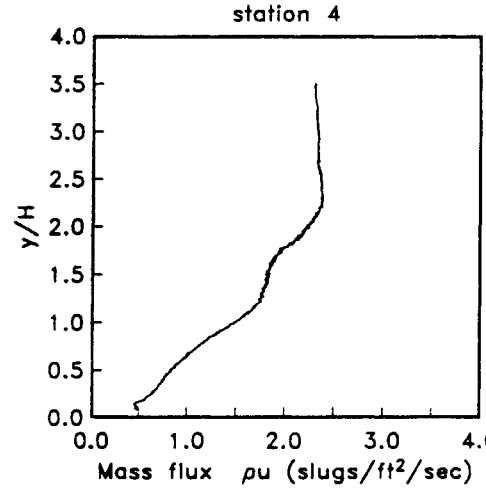

Mass flux profiles, right side, Case (B)

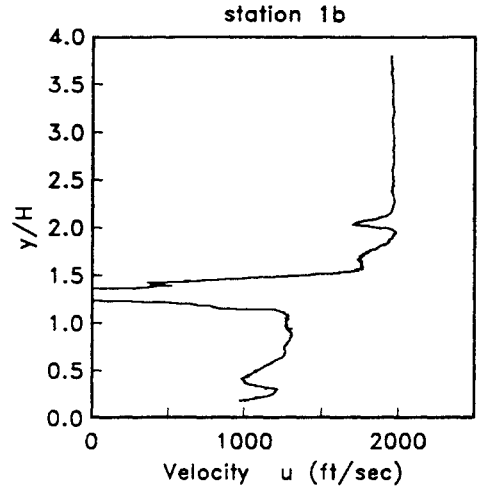

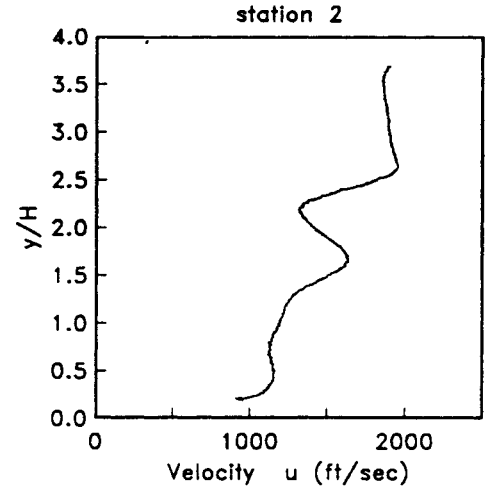

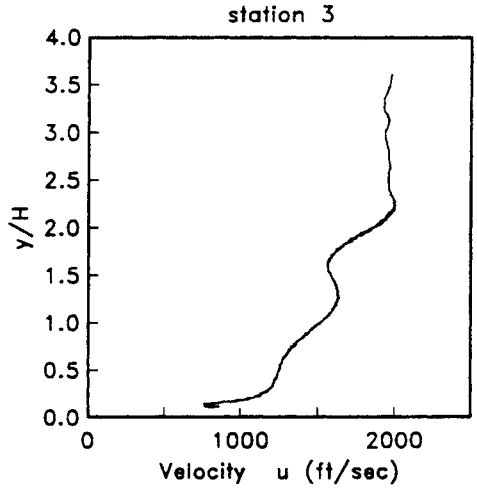

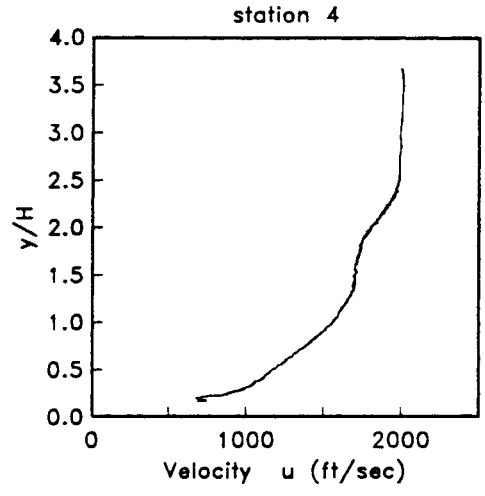

Velocity profiles, left side, Case (C)

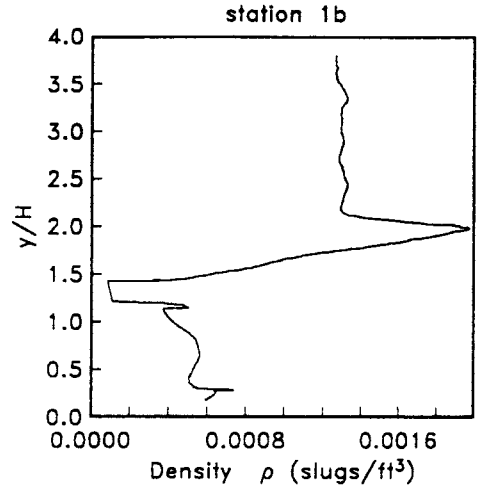

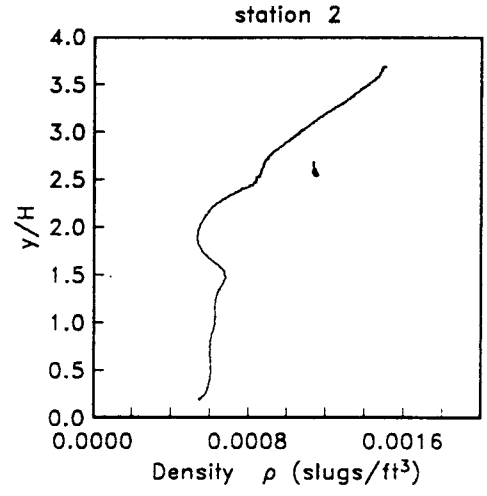

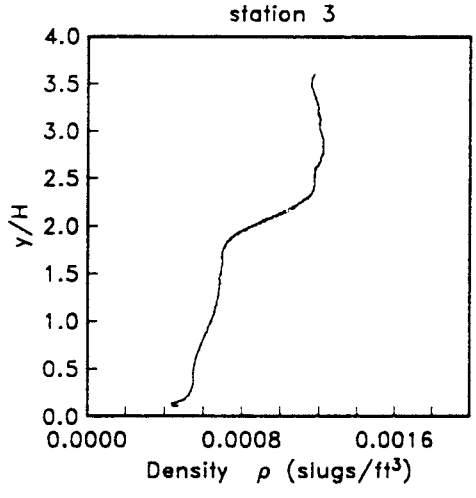

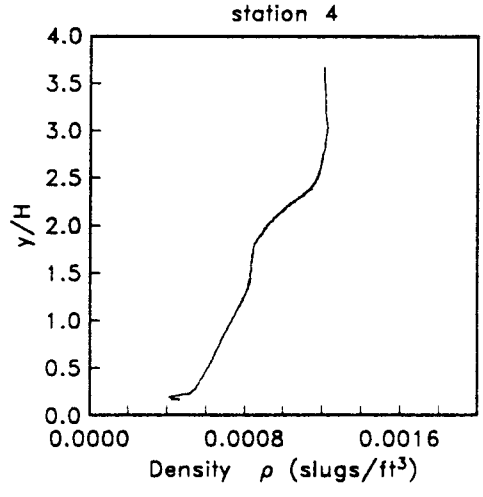

Density profiles, left side, Case (C)

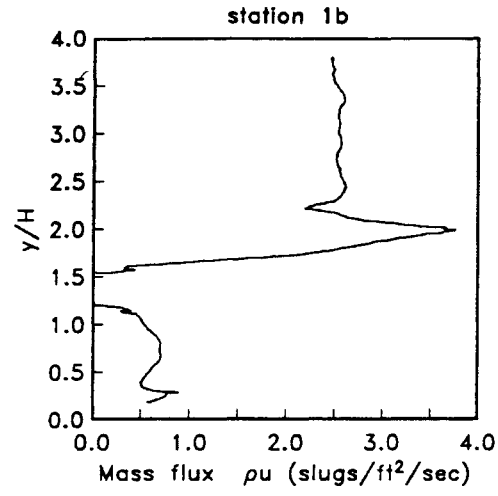

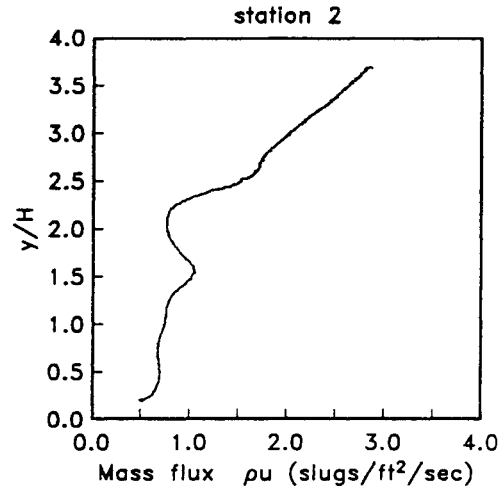

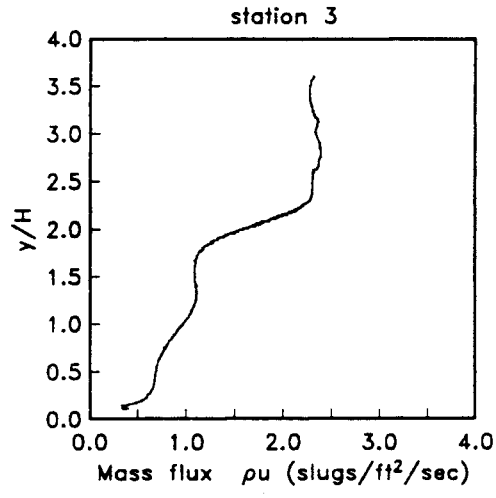

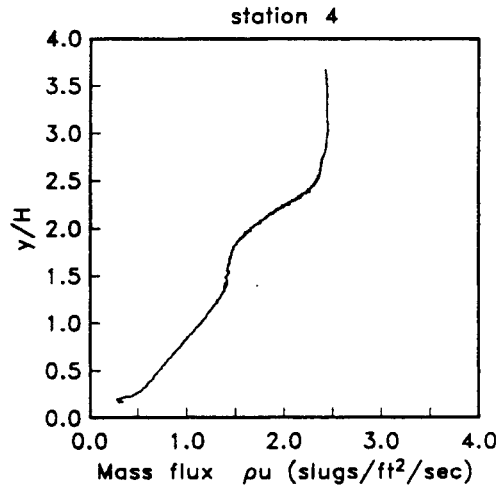

Mass flux profiles, left side, Case (C)

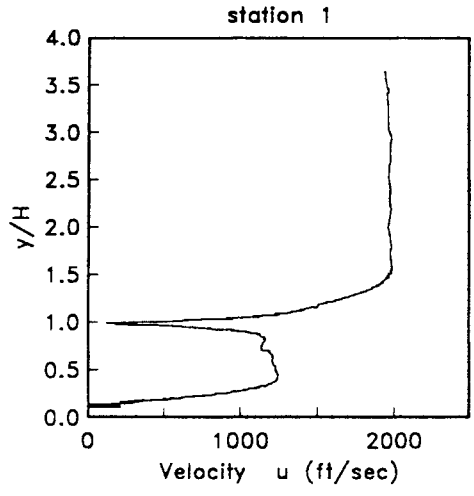

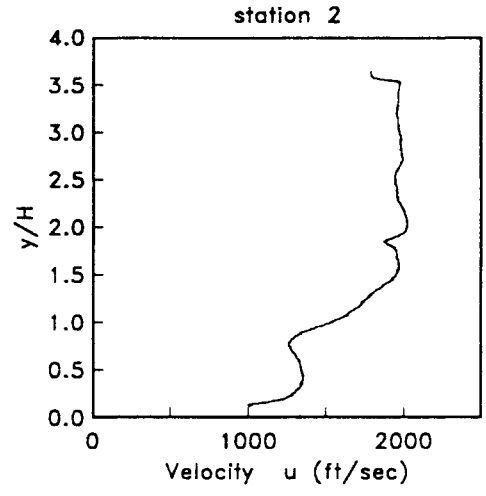

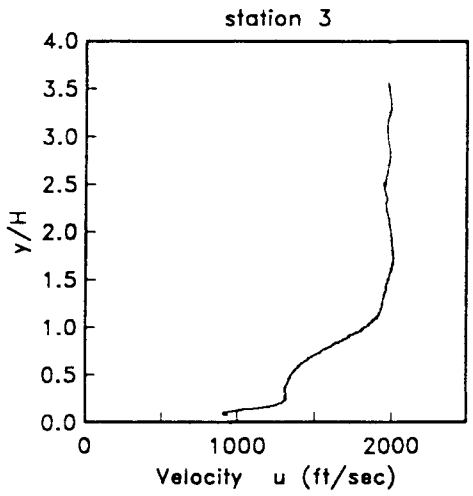

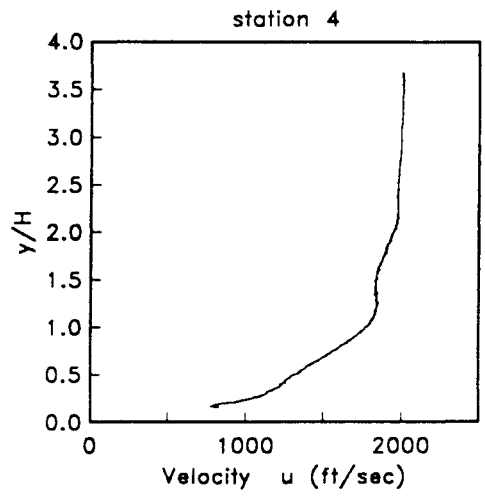

Velocity profiles, right side, Case (C)

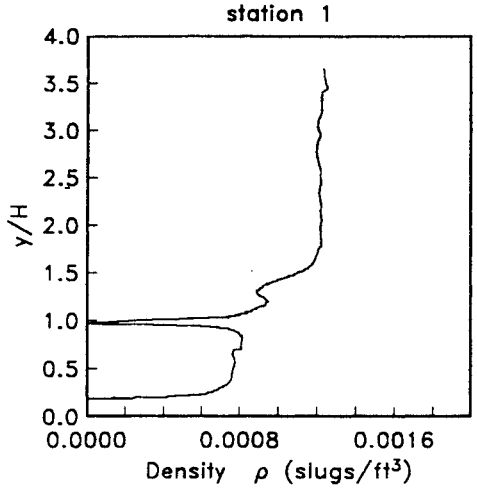

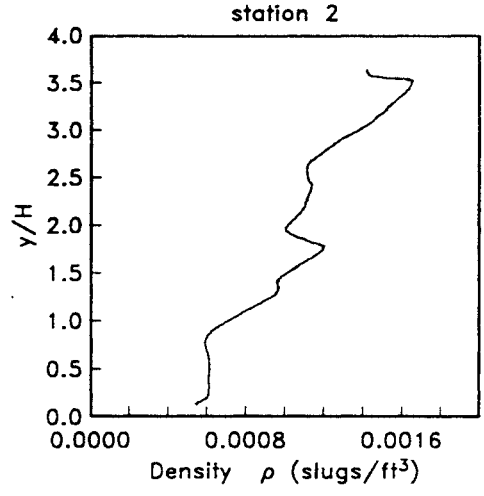

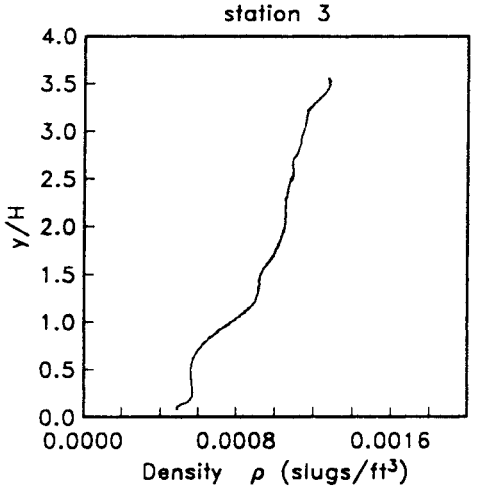

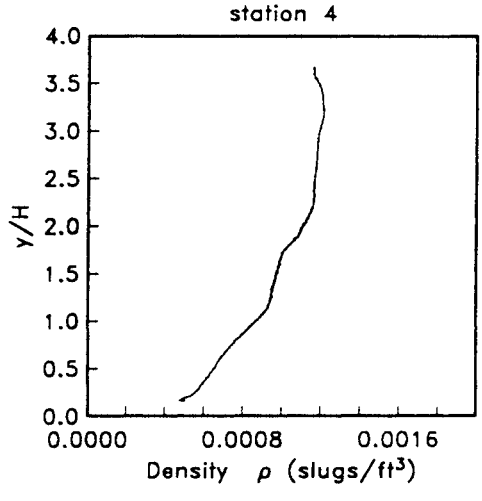

Density profiles, right side, Case (C)

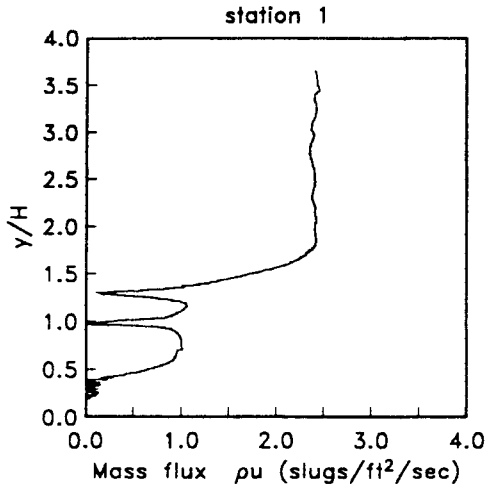

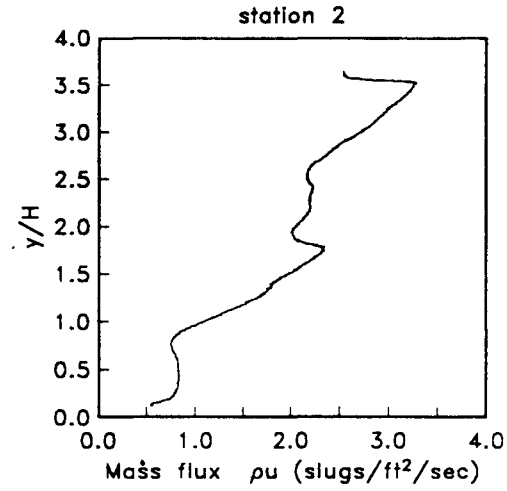

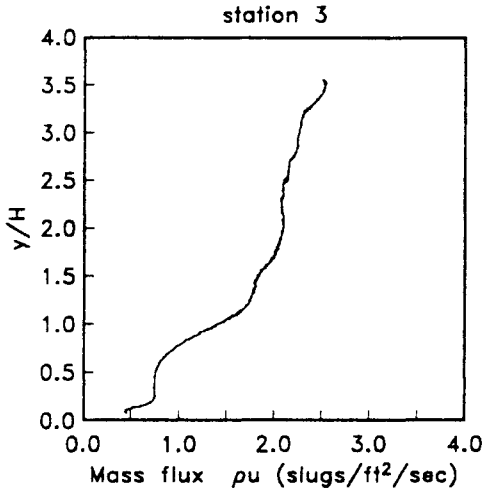

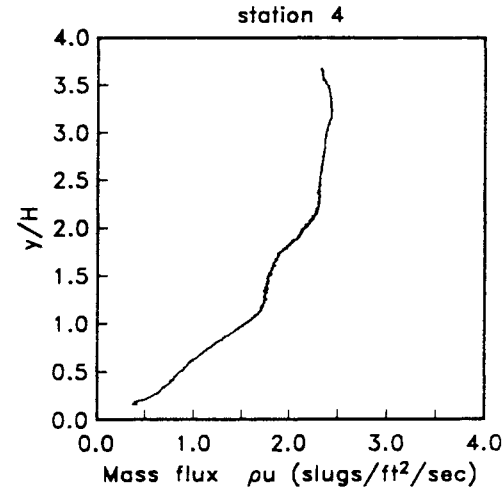

Mass flux profiles, right side, Case (C)

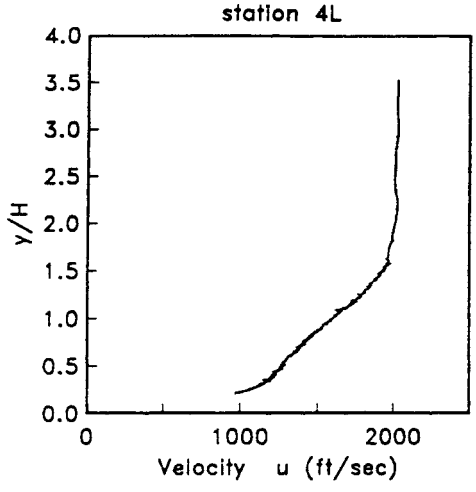

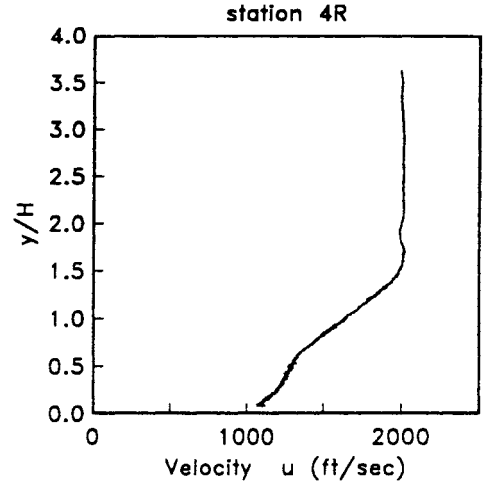

Velocity profiles, Stations 4L,4R, Case (D)

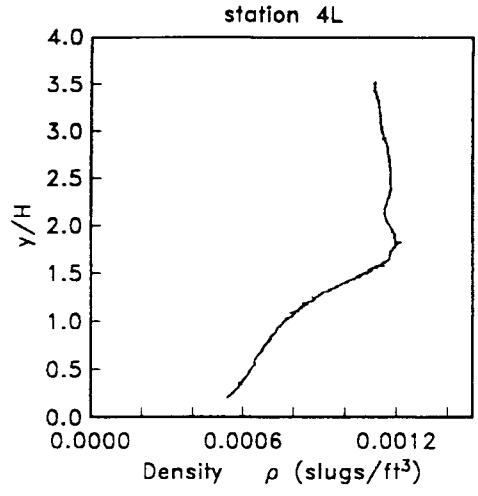

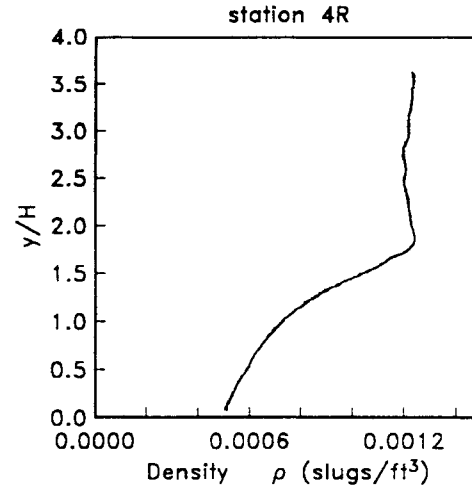

Density profiles, Stations 4L,4R, Case (D)

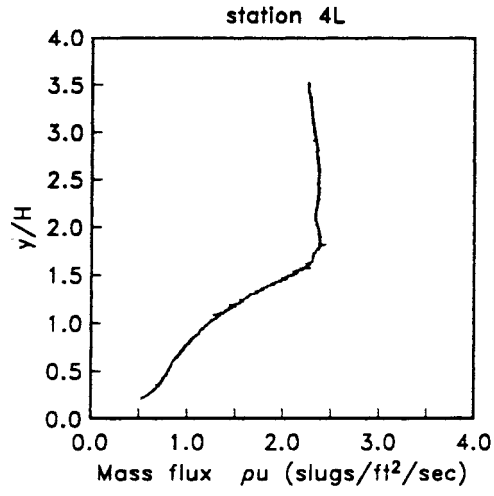

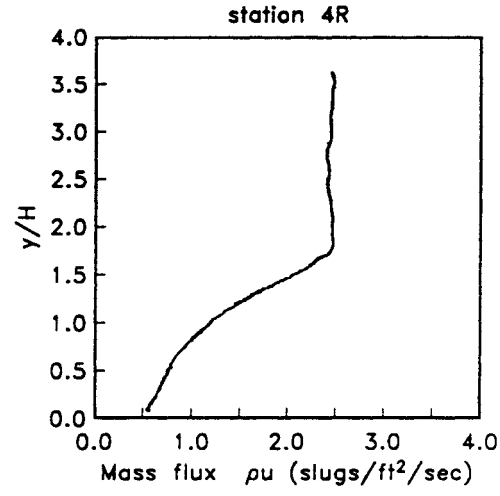

Mass flux profiles, Stations 4L,4R, Case (D)

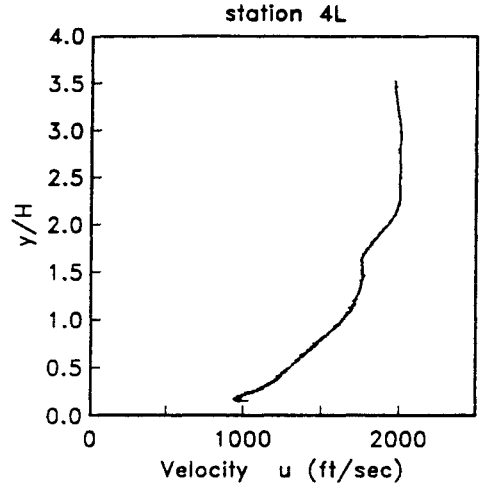

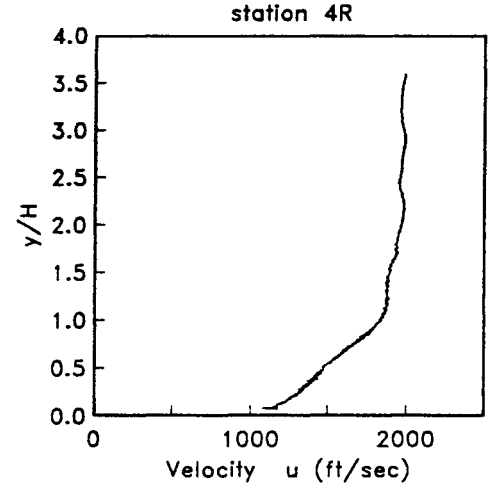

Velocity profiles, Stations 4L,4R, Case (E)

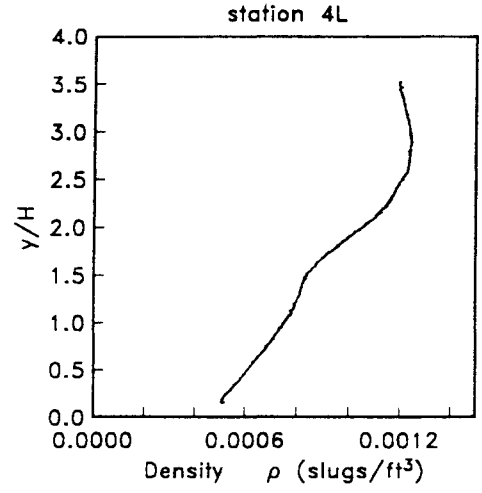

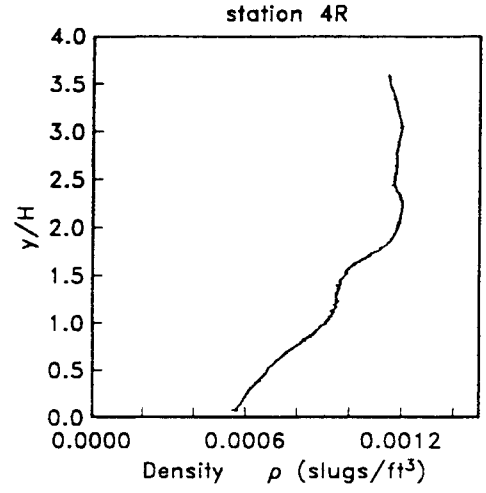

Density profiles, Stations 4L,4R, Case (E)

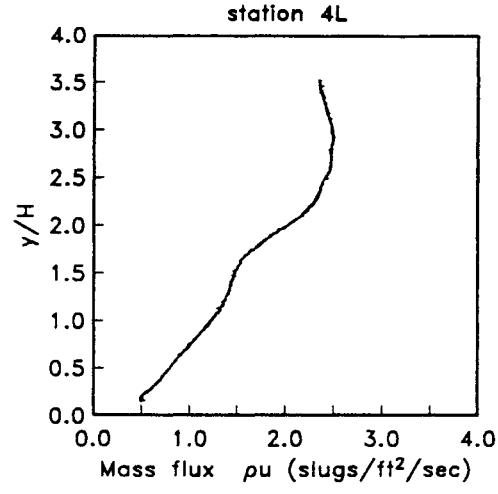

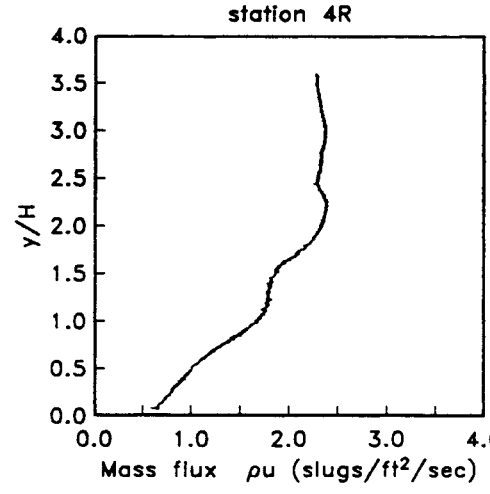

Mass flux profiles, Stations 4L,4R, Case (E)

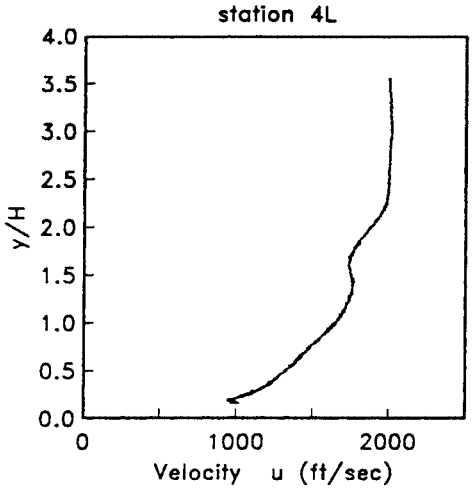

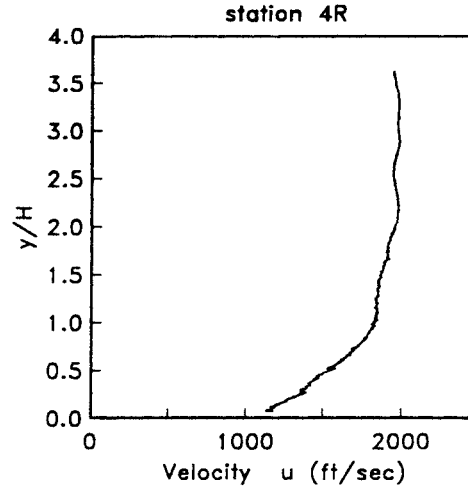

Velocity profiles, Stations 4L,4R, Case (F)

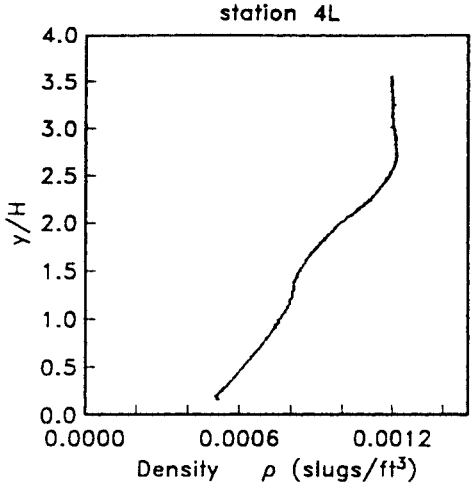

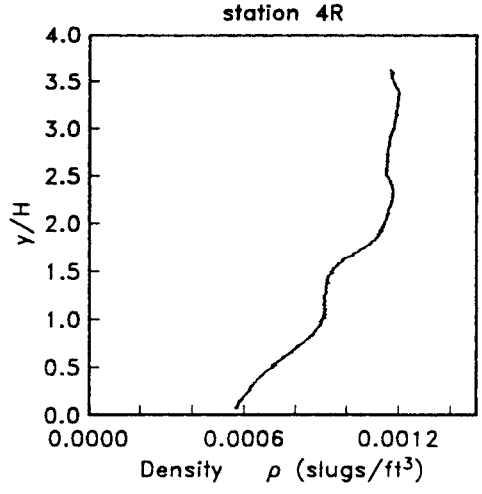

Density profiles, Stations 4L,4R, Case (F)

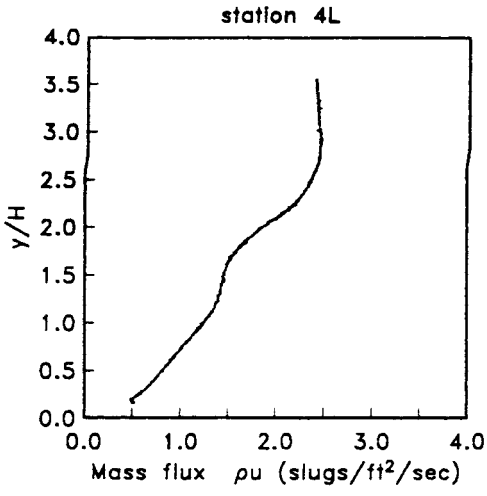

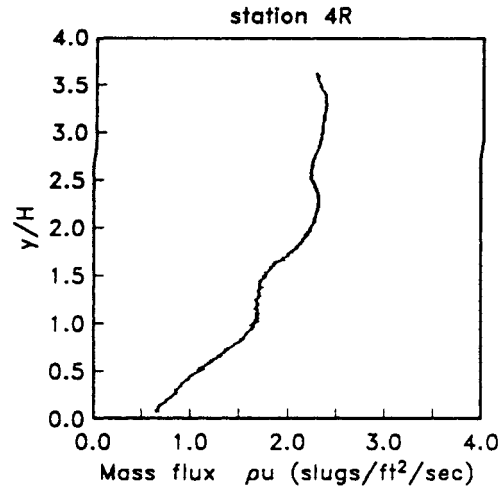

Mass flux profiles, Stations 4L,4R, Case (F)

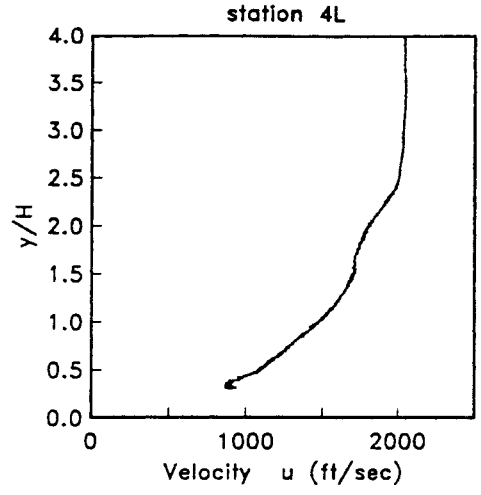

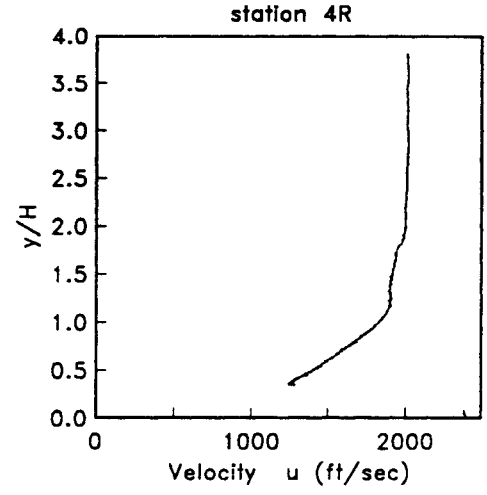

Velocity profiles, Stations 4L,4R, Case (G)

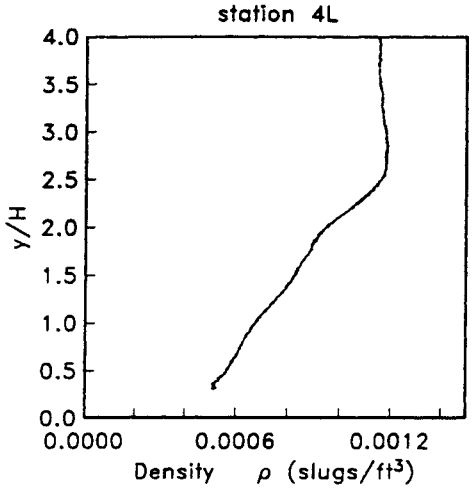

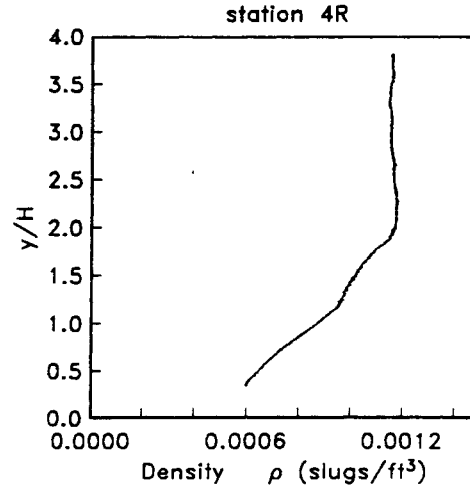

Density profiles, Stations 4L,4R, Case (G)

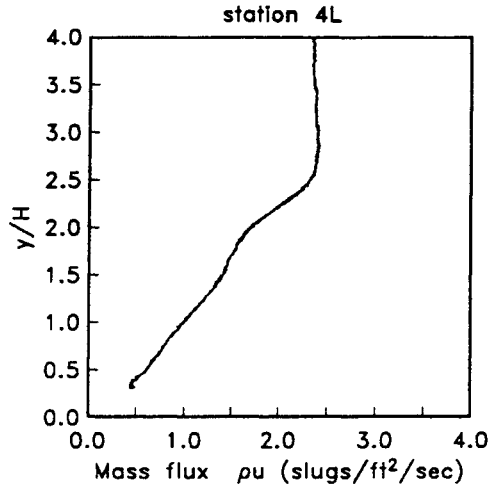

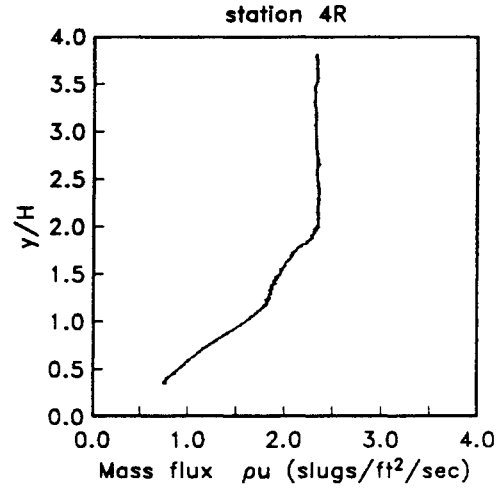

Mass flux profiles, Stations 4L,4R, Case (G)

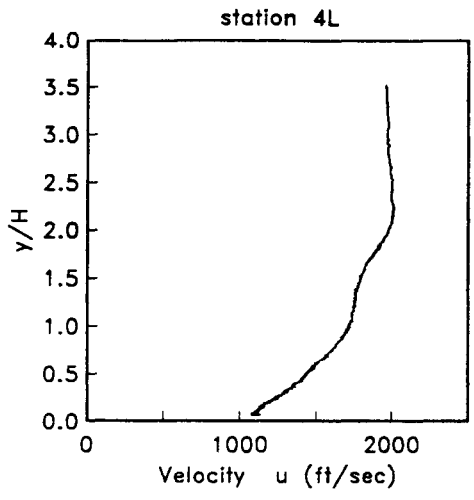

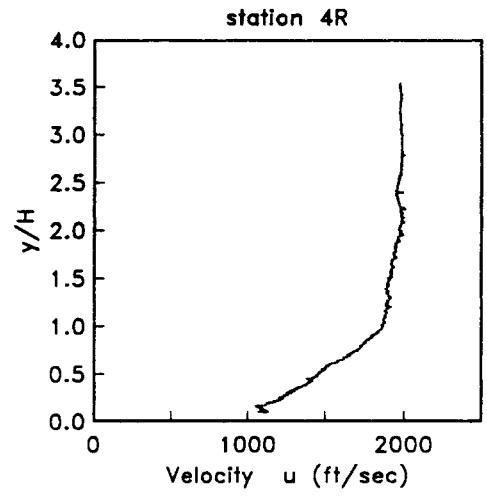

Velocity profiles, Stations 4L,4R, Case (H)

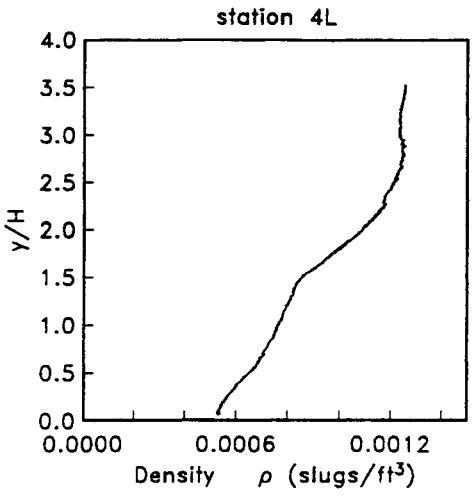

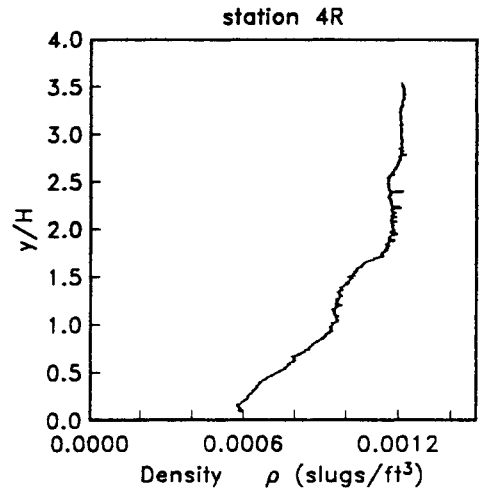

Density profiles, Stations 4L,4R, Case (H)

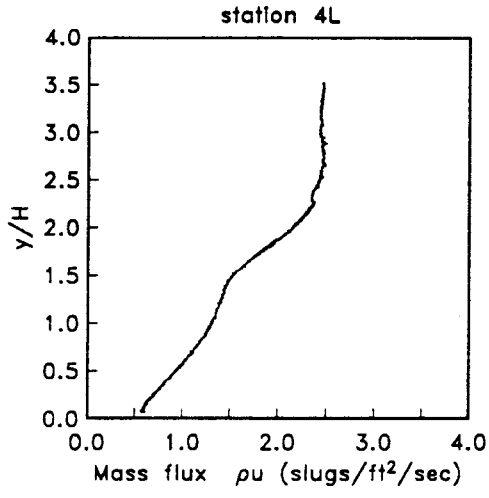

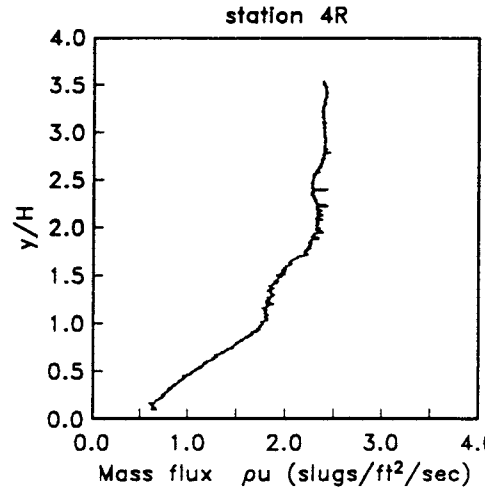

Mass flux profiles, Stations 4L,4R, Case (H)

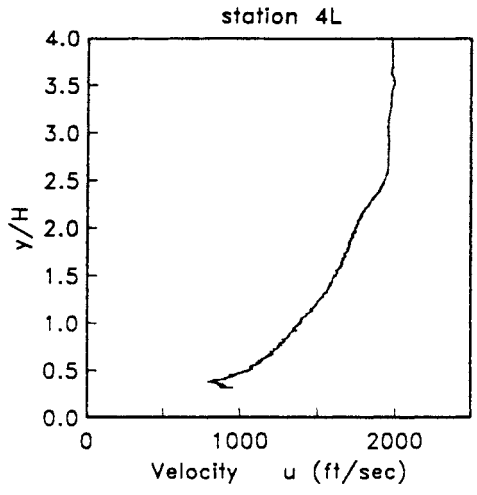

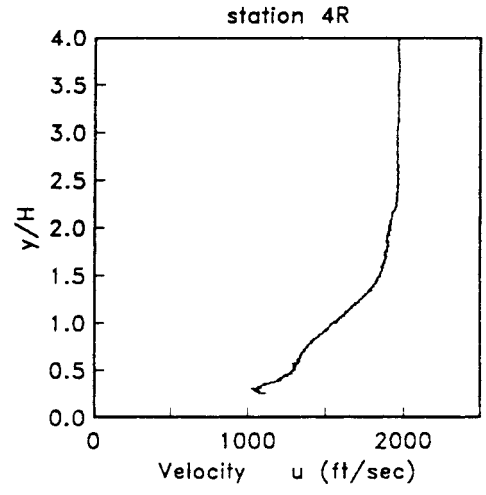

Velocity profiles, Stations 4L,4R, Case (I)

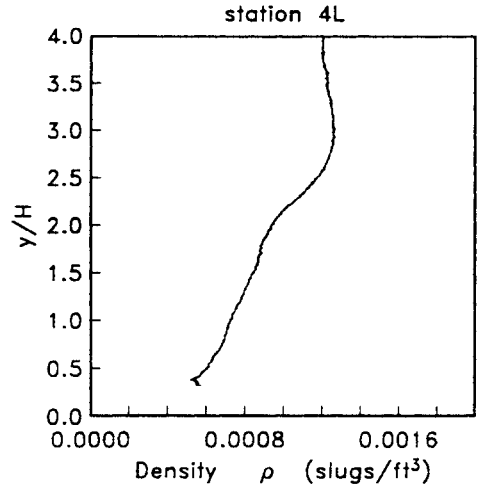

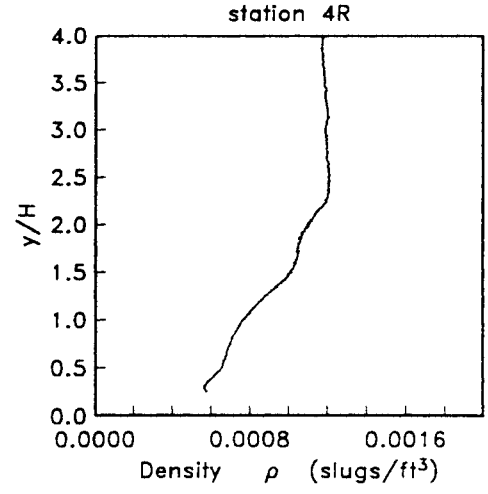

Density profiles, Stations 4L,4R, Case (I)

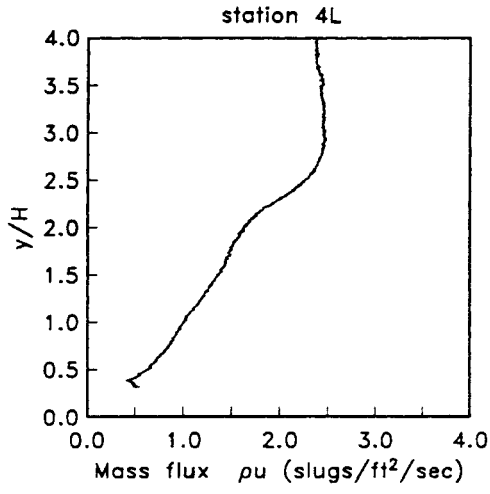

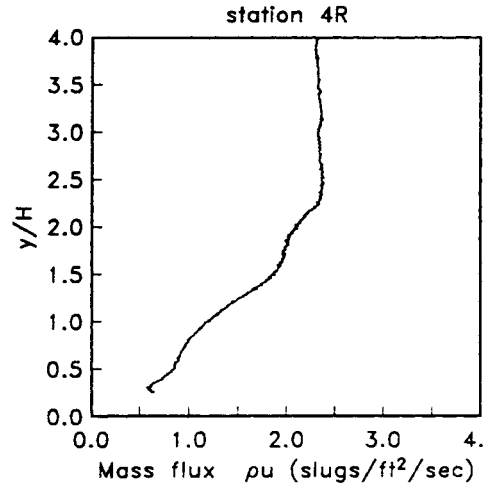

Mass flux profiles, Stations 4L,4R, Case (I)

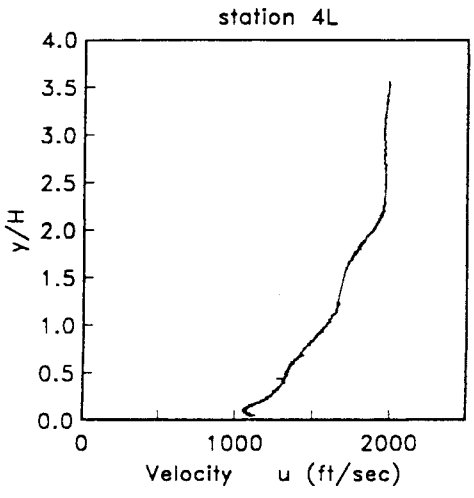

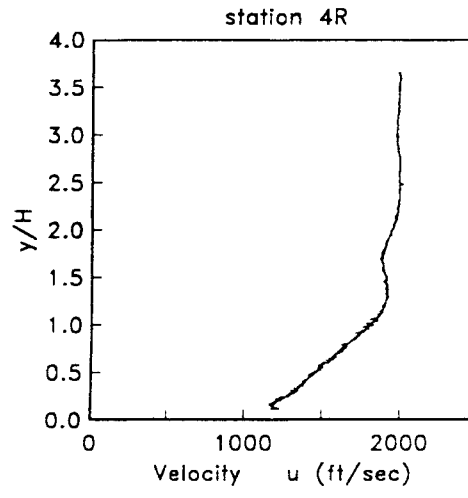

Velocity profiles, Stations 4L,4R, Case (J)

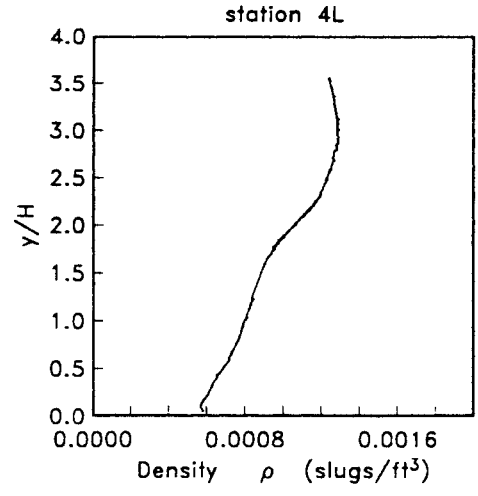

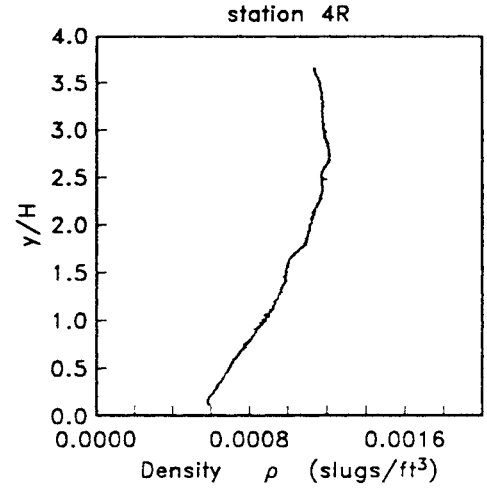

Density profiles, Stations 4L,4R, Case (J)

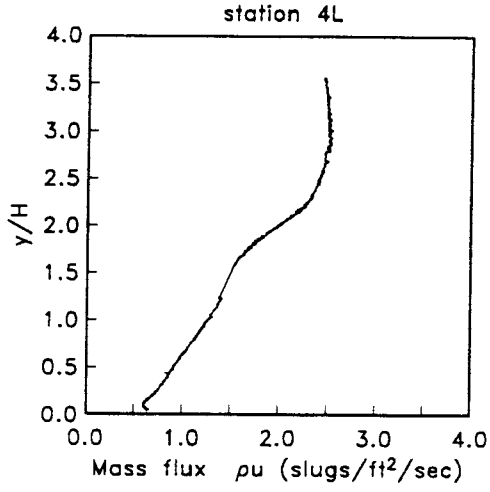

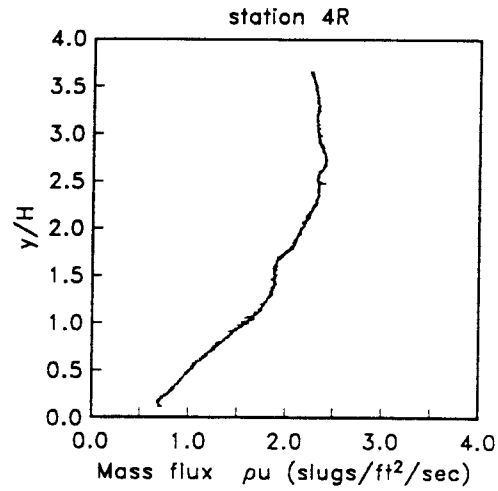

Mass flux profiles, Stations 4L,4R, Case (J)

The vita has been removed from the scanned document